# Implementing a photon physics model in Serpent 2

Toni Kaltiaisenaho

**Thesis supervisor:**

Prof. Filip Tuomisto

**Thesis advisor:**

Adj. Prof. Jaakko Leppänen

**Aalto University**
School of Science

Author: Toni Kaltiaisenaho

Title: Implementing a photon physics model in Serpent 2

Supervisor: Prof. Filip Tuomisto

Advisor: Adj. Prof. Jaakko Leppänen

Photon transport problems are encountered in many areas of science and engineering, such as gamma-heating and radiation shielding calculations in reactor physics, particle physics simulations, and radiation therapy dose calculations. The most accurate approach for solving these problems is the Monte Carlo particle transport method. In order to be applicable, the interactions that photons undergo with matter must be modelled accurately.

In this work, a photon physics model is developed for Serpent 2 Monte Carlo transport code which is primarily used for reactor physics calculations. The four dominant photon interactions with matter are discussed and implemented: the photoelectric effect, Rayleigh scattering, Compton scattering, and pair production. Also, the important atomic relaxation, electron-positron annihilation, and thick-target bremsstrahlung processes are included. Detailed interaction models are used which are not limited only to reactor physics problems. New and modified sampling methods are presented for the photoelectric effect, Doppler broadening of Compton-scattered photons, Compton electrons, and pair production.

The implemented photon physics model is compared with MCNP6 code for a variety of materials and photon energies. A good agreement is obtained in general. At photon energies below 1 MeV or so, differences caused by the Doppler broadening of Compton-scattered photons are encountered. However, these discrepancies should be negligible in reactor physics calculations. At higher energies, differences in the thick-target bremsstrahlung methods cause the photon spectrum given by Serpent to be lower. The angular distribution of pair production seems to be broader in Serpent than in MCNP6. In a simple test geometry Serpent performs faster than MCNP6, up to a factor of 3.

Tekijä: Toni Kaltiaisenaho

Työn nimi: Fotonifysiikkamallin kehittäminen Serpent 2-koodiin

Päivämäärä: 26.5.2016       Kieli: Englanti       Sivumäärä: 7+125

Teknillisen fysiikan laitos

Professuuri: Teknillinen fysiikka

Työn valvoja: Prof. Filip Tuomisto

Työn ohjaaja: Dos. Jaakko Leppänen

Fotonikuljetusongelmia esiintyy monilla tieteen aloilla, kuten esimerkiksi reaktorifysiikkaan liittyvissä gammakuumennus- ja säteilysuojauslaskuissa, hiukkasfysiikan simulaatioissa ja sädehoitojen annoslaskennassa. Tarkin tapa ratkaista näitä ongelmia on Monte Carlo -kuljetusmenetelmä. Jotta tämä menetelmä olisi hyödynnettävissä, on fotonien vuorovaikutukset väliaineen kanssa mallinnettava tarkasti.

Tämän työn aiheena on kehittää fotonifysiikkamalli Serpent 2 Monte Carlo -koodiin, jota käytetään lähinnä reaktorifysiikkaan liittyvässä laskennassa. Neljä tärkeintä fotonien vuorovaikutusta esitellään ja toteutetaan: valosähköinen ilmiö, Rayleigh-sironta, Compton-sironta ja parinmuodostus. Lisäksi atomien relaksaatio, elektroni-positroni-annihilaatio ja paksun kohtion jarrutussäteily otetaan huomioon. Nämä ilmiöt toteutetaan tarkoilla vuorovaikutusmalleilla, joiden käyttö ei rajoitu pelkästään reaktorifysiikkalaskuihin. Työssä esitellään uusia ja muokattuja laskentamenetelmiä valosähköiselle ilmiölle, Compton-sironneiden fotonien Doppler-leventämiselle, Compton-elektroneille ja parinmuodostukselle.

Kehitettyä fotonifysiikkamallia verrataan MCNP6-koodiin testaamalla useita materiaaleja ja fotonien energioita. Tulokset vastaavat yleisesti ottaen hyvin toisiaan. Alle 1 MeV:n energioilla havaitaan Doppler-leventämisen mallintamisen aiheuttamia eroja. Näiden erojen ei kuitenkaan pitäisi olla merkittäviä reaktorifysiikkalaskuissa. Suuremmilla energioilla Serpent tuottaa matalamman spektrin kuin MCNP6, mikä johtuu eroista jarrutussäteilymenetelmässä. Parinmuodostuksen kulmajakauma näyttäisi olevan Serpentissä leveämpi kuin MCNP6:ssa. Yksinkertaisessa testausgeometriassa Serpentin laskenta-aika on lyhyempi kuin MCNP6:n, ero on suurimmillaan kolminkertainen.

Avainsanat: Monte Carlo fotonikuljetus, Serpent, valosähköinen ilmiö, Rayleigh-sironta, Compton-sironta, parinmuodostus

# Preface

Espoo 26.5.2016

Toni Kaltiaisenaho

# Contents

# Abbreviations

| | |
|---|---|
| CDF | Cumulative distribution function |
| CSDA | Continuous slowing down approximation |
| DCS | Differential cross section |
| DDCS | Double differential cross section |
| DWBA | Distorted wave Born approximation |
| EADL | Evaluated Atomic Data Library |
| ENDF | Evaluated Nuclear Data File |
| EPDL97 | Evaluated Photon Data Library '97 Version |
| IA | Impulse approximation |
| ISF | Incoherent scattering function |
| NIST | National Institute of Standards and Technology |
| PDF | Probability density function |
| QED | Quantum electrodynamics |
| RIA | Relativistic impulse approximation |
| RNG | Random number generator |
| TTB | Thick-target bremsstrahlung |
| WH | Waller–Hartree theory |

# 1 Introduction

Radiation transport problems are encountered in many fields of science and engineering. Modelling of the core of a nuclear reactor, radiotherapy treatment planning, shielding of satellite electronics, particle physics simulations, and many other applications require advanced computational tools for radiation calculations. The state-of-the-art methodology for solving these problems is the Monte Carlo method which enables simulating particle transport process in complicated geometries without major approximations. The basic idea of the Monte Carlo method is to simulate the track of a particle as it travels in a medium by using accurate models of interactions between the particle and matter. A large number of simulated particles are required to obtain accurate estimates of desired quantities, which makes the Monte Carlo method computationally intensive and time-consuming. However, increasing computational capacity and parallel computing have made the Monte Carlo method a feasible alternative over faster but less accurate methods.

A variety of particle types can be simulated with the Monte Carlo method, such as neutrons, photons, electrons, protons, and heavy ions. In this thesis, the Monte Carlo method is applied to photons in the energy ranges of X-rays and gamma rays which are generated, for example, in nuclear reactions, radioactive decay, acceleration of charged particles, and transitions between atomic energy levels. These high-energy photons can travel long distances and undergo multiple interactions with the matter before finally being absorbed. As photons interact with the matter, part of their energy is deposited in the medium. The Monte Carlo method is often used for estimating the spatial distribution of the deposited energy or the energy spectrum of photons in complicated geometries. Such detailed calculations are needed for, e.g., taking into account gamma-heating in nuclear reactors, calculating radiation doses in radiotherapy treatments, and modelling gamma-ray detectors.

The topic of this thesis is to implement a photon physics model in Serpent 2. Serpent [1] is a three-dimensional, continuous-energy Monte Carlo neutron transport code developed at VTT Technical Research Centre of Finland Ltd. While originally developed as a lattice physics code for spatial homogenization [2], Serpent now includes many state-of-the-art features, such as group constant generation for reactor simulator codes [3], built-in depletion solver [4], and on-the-fly treatment of temperature dependence of microscopic cross sections [5]. A major on-going work is the development of multi-physics capabilities for coupling Serpent with fuel performance and thermal hydraulics codes [6]. In the core of a nuclear reactor, the temperature and density distributions of the core materials and the moderator are coupled with the neutronics of the system. Photon transport mode is needed to calculate the gamma-heating for obtaining a realistic temperature distribution in the core. However, the photon transport mode presented in this work is not limited only to reactor physics applications, but is intended to be a detailed model applicable for other purposes as well in the energy range of 1 keV and 100 MeV.

The logic behind the Monte Carlo transport method is practically the same for

neutrons and photons, and therefore the existing transport routines in Serpent can be used without major modifications. Thus, the main focus of this thesis is on presenting and implementing interaction models between photons and matter. Various Monte Carlo codes have been developed for photon transport calculations, such as PENELOPE [7], EGS5 [8], EGSnrc [9], MCNP6 [10], FLUKA [11, 12], and Geant4 [13]. However, there is no unified treatment of photon interactions in these codes. One reason for this is that accurate interaction models are often very complicated or difficult to apply as such for the Monte Carlo transport method, and therefore, various approximations with different ranges of validity have been developed. The needed accuracy, the speed of the computation, and often the complexity of the implementation determine which approximation is used. Choosing the suitable models for our purposes can become a tedious task because of the large variety of methods used in different Monte Carlo codes. Fortunately, many comparisons and evaluations can be found in the literature, significantly simplifying this task.

A major challenge in photon transport problems is that electrons and positrons are generated in photon–matter interactions. The transport of charged particles differs significantly from neutral particles due to the large number of interactions they undergo with matter. In order to perform an electron transport calculation in a reasonable amount of time, special simulation techniques are required. These methods are far too vast and complicated to be covered here, and hence, a full electron transport mode is not implemented in Serpent as a part of this work. Luckily, the error introduced by omitting electron transport is usually small because electrons lose their energy in much shorter distances than photons, especially at low energies. However, high-energy electrons lose some of their energy by emitting bremsstrahlung photons which can travel far away from the point of emission, and therefore must be taken into account. A so-called thick-target bremsstrahlung approximation is implemented for generating bremsstrahlung photons which can be used, e.g., in gamma-heating calculations, but is not suitable for high-detail applications, such as radiotherapy treatment simulations. It is possible that a full electron transport mode will be implemented in Serpent in the future. Therefore, the generation of electrons by photon interactions is also treated in a detailed manner in this work.

This thesis is organized as follows: In Sec. 2, the Monte Carlo transport method is presented and the important concepts of random sampling and cross section are discussed. Sec. 3 forms the main part of this thesis, presenting the four most important photon interactions with matter: photoelectric effect, Rayleigh scattering, Compton scattering, and electron-positron pair production. Atomic relaxation and electron-related interactions are discussed in Secs. 4 and 5, respectively. The implemented photon transport model is compared with MCNP6 Monte Carlo code in Sec. 6 using two test simulation cases. Finally, we conclude in Sec. 7.

# 2   Monte Carlo particle transport

The basic idea of the Monte Carlo particle transport method is to simulate tracks of particles in some geometry as they would occur in a real-life physical process. A particle track consists of straight lines of free-flights which are joined together by interaction locations in which the particle interacts with targets, such as atoms. The medium where the particles travel is usually approximated to consist of uniformly distributed targets. The general procedure for simulating particle tracks is straightforward. The desired number of particles are created from a known source, determining the initial locations, directions, and energies of the particles. Because each particle can be regarded as independent of all the other particles, their transport can be simulated one by one. First, the free path length between the initial location of the particle and the first interaction location is selected, and the particle is moved along its direction vector to the interaction site. The target type and the interaction type are then selected and the interaction process is modelled. In a scattering interaction, the particle direction and energy are changed and updated. The particle track is terminated in an absorption interaction or if some stopping condition is met. Any secondary particles generated in the interaction are modelled accordingly. This procedure is then repeated using the updated location, direction and energy until the particle track is terminated.

What makes this simulation procedure a Monte Carlo method is the way the free path length, target type, interaction type, outcome of an interaction, and often the initial parameters of particles are selected. These are all random variables which are associated with probability density functions. The value of each variable is randomly picked from the corresponding distribution. This is essentially what occurs in the actual physical process of particle transport, in which the indeterminacy is caused by the quantum nature of particle interactions.

The desired outcome of a Monte Carlo particle transport simulation is usually an estimate of some variable, such as a deposited energy in some volume element. Estimates are obtained by recording the desired events for each simulated particle, and then averaging over the number of recorded events. Appropriate normalization is also needed to obtain an estimate of an actual physical parameter. Due to the stochastic nature of the transport process, the estimate is a random variable which must be accompanied by an error estimate. A large number of particles are often needed for obtaining reliable estimates, which makes the Monte Carlo transport method computationally costly.

This section presents the mathematical basis of the transport process discussed in the first paragraph, and introduces important concepts needed in the following sections. The emphasis is on how the probability distributions needed for transport calculation are formed, and how random numbers can be drawn from them. We therefore start our discussion on the basics of probability theory which leads us to different random sampling methods. The important concept of cross section is then presented and its usage in the transport process is discussed. Finally, the general algorithm for the

Monte Carlo particle transport is presented.

## 2.1 Basics of probability theory

Probability theory provides the mathematical basis for studying phenomena associated with random behaviour which can be due to unknown or uncontrollable factors, or the physical nature of the phenomenon. The basic concept of probability theory is the random variable, here denoted by $X$, which can obtain a set of values, each of which is associated with a probability. The outcome of a random variable is called a random variate. Depending on the values $X$ can obtain, $X$ can be a discrete or continuous random variable. Here, the necessary definitions of probability theory needed for understanding this work are given.

The probability of finding a continuous random variable $X$ between differential interval $x$ and $x + dx$ is given by

$$P(x < X \leq x + dx) = f_X(x)dx, \tag{2.1}$$

where $f_X(x)$ is a probability density function (PDF). The PDF of a continuous random variable satisfies the conditions

$$f_X(x) \geq 0 \quad \forall x \quad \text{and} \quad \int_{-\infty}^{\infty} f_X(x)dx = 1. \tag{2.2}$$

In the case of a discrete random variable $X$, each possible outcome $x_i$ is associated with a probability $P(X = x_i)$ which satisfies

$$P(X = x_i) \in [0, 1] \quad \forall x_i \quad \text{and} \quad \sum_i P(X = x_i) = 1. \tag{2.3}$$

The PDF for a discrete random variable $X$ can be formed using the Dirac delta function as

$$f_X(x) = \sum_i P(X = x_i)\delta(x - x_i), \tag{2.4}$$

which unifies the treatment of discrete and continuous random variables.

Cumulative distribution function (CDF) of a continuous random variable is defined as

$$F_X(x) = \int_{-\infty}^{x} f_X(x')dx' = P(X \leq x). \tag{2.5}$$

Therefore, the probability of finding $X$ between $a$ and $b$ is given by

$$P(a < X \leq b) = \int_a^b f_X(x)dx = F_X(b) - F_X(a). \tag{2.6}$$

For a discrete distribution the CDF is simply given by

$$F_X(x) = \sum_{x_i \leq x} P(X = x_i). \tag{2.7}$$

As it's clear from the definitions above, a CDF is a non-decreasing, right-continuous function which satisfies

$$\lim_{x \to -\infty} F_X(x) = 0 \quad \text{and} \quad \lim_{x \to \infty} F_X(x) = 1. \tag{2.8}$$

For a short notation, we write $X \sim F_X$ when $X$ follows a distribution $F_X$.

The mean of a random variable $X$ is defined as

$$\langle x \rangle = \int_{-\infty}^{\infty} x f_X(x) dx. \tag{2.9}$$

In general, the expected value of a function $g(x)$ is given by

$$\langle g(x) \rangle = \int_{-\infty}^{\infty} g(x) f_X(x) dx. \tag{2.10}$$

The joint PDF of two random variables $X$ and $Y$ is a function which satisfies the conditions

$$f_{X,Y}(x, y) \geq 0 \quad \forall x, y \quad \text{and} \quad \iint f_{X,Y}(x, y) dx dy = 1. \tag{2.11}$$

The one-variable PDFs of $x$ and $y$ are called marginal PDFs and are obtained as

$$f_X(x) = \int f_{X,Y}(x, y) dy \quad \text{and} \quad f_Y(y) = \int f_{X,Y}(x, y) dx. \tag{2.12}$$

The conditional PDFs of $X$ given that $Y = y$, and $Y$ given that $X = x$ are given by

$$f_{X|Y}(x|y) = \frac{f_{X,Y}(x, y)}{f_Y(y)} \quad \text{and} \quad f_{Y|X}(y|x) = \frac{f_{X,Y}(x, y)}{f_X(x)}. \tag{2.13}$$

## 2.2 Random sampling from probability distributions

The key idea of the Monte Carlo method is to generate a large number of random variates obeying the distributions related to the studied phenomenon, and then use them in a simulation to obtain statistical estimates of desired variables. Generating random variates from a probability distribution is called random sampling, or simply sampling. We discuss here some of the basic sampling methods used in the later sections of this work.

One problem in random sampling is that true randomness cannot be generated by pure arithmetic operations performed by computers. Instead, computers use algorithms called random number generators (RNG) to generate pseudorandom numbers which are not truly random. Many RNGs have been developed for different purposes, and the choice of the RNG strongly depends on the application. Statistical tests can be used for investigating the randomness of random number sequences produced by RNGs [14]. The algorithms and properties of different RNGs are not

discussed here, and we assume that pseudorandom numbers can be regarded as truly random.

The random numbers produced by RNGs are most often uniformly distributed between 0 and 1. Many methods based on probability theory exist for transforming uniformly distributed random numbers into random variates following the wanted distribution. The chosen random sampling method is applied for constructing an algorithm which produces a correctly distributed random variate using the known input parameters of the distribution. The most important property of a sampling algorithm is usually the speed, assuming that the algorithm is accurate. However, the speed naturally depends on the used RNG, programming language, compiler options, hardware related properties, and the distribution itself, complicating the comparison of different methods. Therefore, no general way exists for choosing the best method for generating random variates.

### 2.2.1 Inverse transform method

The inverse transform method is probably the most basic method for generating random numbers. The idea is to transform a uniformly distributed random variable $U \sim unif(0,1)$ into a random variable $X \sim F_X$ using the inverse function of the CDF, $F_X^{-1}$. It can be shown [15] that the CDF of a random variable given by

$$X = F_X^{-1}(U) \tag{2.14}$$

is in fact $F_X$. Therefore, to generate a random variate of $X$, one generates a random variate $\xi$ of $U$ and then calculates $F_X^{-1}(\xi)$. The inverse transform method is applicable when the inverse function has a simple form and can be quickly computed. However, in many cases the use of the inverse transform method is limited because the CDF or its inverse may not be expressed analytically, or the computation of the inverse function is too expensive.

Two examples of using the inverse transform method are given here. The first example is the exponential distribution which has a PDF

$$f_X(x) = \kappa e^{-\kappa x}, \quad x \geq 0, \tag{2.15}$$

where $\kappa > 0$. The CDF is given by

$$F_X(x) = \int_0^x \kappa e^{-\kappa x'} dx' = 1 - e^{-\kappa x}. \tag{2.16}$$

A random variable $X$ following the exponential distribution is therefore given by

$$X = F_X^{-1}(U) = -\frac{1}{\kappa} \ln(1 - U). \tag{2.17}$$

Because $1 - U \sim unif(0,1)$, it is equivalent to replace $1 - U$ by $U$.

The second example is a discrete distribution of random variable $X$ which can obtain values $X = x_i, \; i = 1, 2, \ldots$ . The CDF of a discrete random variable is given by Eq. (2.7). The inverse transform method yields that the random variable can be sampled by

$$F_X(x_{i-1}) < \xi \le F_X(x_i), \tag{2.18}$$

where $F_X(x_0) = 0$ is assumed. It is straightforward to verify this formula by noting that the probability for finding $\xi$ between $x_{i-1}$ and $x_i$ is equal to $F_X(x_i) - F_X(x_{i-1}) = \mathrm{P}(X = x_i)$. The index $i$ satisfying Eq. (2.18) can be found using a binary search algorithm which performs in $\mathcal{O}(\log n)$ time. As a side note, this method is not the fastest way to sample a discrete random variable. An example of a faster algorithm is the Walker's alias method [16] which performs in a constant $\mathcal{O}(1)$ time.

### 2.2.2 Rejection sampling method

Another common technique to generate random variates is the rejection sampling method, which is also known as the acceptance-rejection method. Consider two random variables $X \sim F_X$ and $Y \sim G_Y$ with PDFs $f_X$ and $g_Y$, respectively. We want to generate random variates of $X$ which is difficult or impossible to do using other methods, whereas $Y$ is straightforward to sample using, for example, the inverse transform method. The rejection sampling method is based on the result [15] that the CDF of $X$ can be written as the conditional distribution

$$\mathrm{P}\left(Y \le y \mid U \le \frac{f_X(Y)}{Cg_Y(Y)}\right) = F_X(y), \tag{2.19}$$

where $U \sim unif(0,1)$ and the constant $C$ satisfies

$$0 < \frac{f_X(x)}{Cg_Y(x)} \le 1 \quad \forall x \quad \text{and} \quad C \ge 1. \tag{2.20}$$

Therefore, the random variable $X$ can be sampled by first sampling a random variate of $Y$, say $y$, and then accept this value as a random variate of $X$ if

$$\xi \le \frac{f_X(y)}{Cg_Y(y)}, \tag{2.21}$$

where $\xi$ is a random variate of $U$.

The rejection sampling method can be generalized by introducing the so-called rejection function

$$\psi(x) = \frac{f(x)}{Cg(x)}, \tag{2.22}$$

so that a PDF $f(x)$ can be written as

$$f(x) = C\psi(x)g(x). \tag{2.23}$$

The constant $C$ can now be interpreted as a normalization constant. Because $C$ satisfies Eq. (2.20) it is obvious that $0 \leq \psi(x) \leq 1$. An algorithm for the rejection sampling method can now be given as follows:

(i) Generate a random variate $x$ from $g(x)$ and $\xi \sim unif(0, 1)$.

(ii) If $\xi \leq \psi(x)$, accept $x$. Else, go to step (i).

Note that the random variable $X$ is not explicitly stated in this notation, and $x$ is used as a random variate in the algorithm. Also, by stating $\xi \sim unif(0, 1)$ we mean that $\xi$ is a random variate of a uniformly distributed random variable $U \sim unif(0, 1)$. This notation is used hereafter whenever applicable.

The efficiency of the sampling algorithm is defined as the probability of accepting the sampled value, which is given by

$$\int_{-\infty}^{\infty} \psi(x)g(x)dx = \frac{1}{C} \int_{-\infty}^{\infty} g(x)dx = \frac{1}{C}. \tag{2.24}$$

Therefore, the constant $C$ should be minimized in order to obtain good efficiency. However, a high efficiency doesn't necessarily make the algorithm fast if generating $x$ from $g(x)$ is slow. Naturally, the speed of the algorithm depends also on the computation of $\psi(x)$, and the used random number generator, too. Therefore, there is no general way to determine the functions $g(x)$ and $\psi(x)$ to obtain the fastest possible algorithm.

### 2.2.3 Sampling from a tabulated distribution

Often, a PDF of a continuous random variable is given in a tabulated numerical form if it is a result of an experiment or simulation, or if the PDF is difficult or impossible to express in an analytical form. In order to draw random values from such a tabulated distribution, proper interpolation method must be used between the data points, and in some cases the data must also be extrapolated. The inverse transform method is the preferred technique when the interpolation method is simple enough so that the CDF can be easily inverted. Naturally, it is also possible to use the rejection sampling method if a proper rejection function can be found. Here, we discuss only the use of the inverse transform method on sampling a continuous random variable from a tabulated single-variate distribution.

Consider a piecewise PDF $f(x)$ so that $(x_i, f(x_i)), i = 1, 2, \ldots, N$ are the tabulated points of the PDF. The CDF can be expressed as

$$F(x) = \int_{-\infty}^{x} f(x')dx' = F(x_i) + \int_{x_i}^{x} f(x')dx', \quad x_i \leq x \leq x_{i+1}. \tag{2.25}$$

To use the inverse transform method, the CDF must be evaluated at the tabulated $x_i$ values. The first value of the CDF, $F(x_1)$, is either known or integrated from an

extrapolation function. The rest of the CDF values are calculated with Eq. (2.25), and extrapolation function is again used if $F(x_N) < 1$. The first step in the sampling procedure is to create $\xi \sim unif(0, 1)$, after which the index $i$ satisfying $F(x_i) \leq \xi \leq F(x_{i+1})$ is sought. The value of $x$ is then solved using the inverse of the CDF. Three examples of using the inverse transform method with different interpolation techniques are given here. In all cases, it is assumed that

$$x_i \leq x \leq x_{i+1} \quad \text{and} \quad F(x_i) \leq \xi \leq F(x_{i+1}), \tag{2.26}$$

and that $F(x_1) = 0$ and $F(x_N) = 1$.

The simplest case is to assume that the PDF can be expressed as a step function

$$f(x) = f(x_i), \tag{2.27}$$

which yields a piecewise linear CDF

$$F(x) = F(x_i) + f(x_i)(x - x_i) = F(x_i) + \frac{F(x_{i+1}) - F(x_i)}{x_{i+1} - x_i}(x - x_i). \tag{2.28}$$

Solving the inverse function gives the random value

$$x = x_i + \frac{\xi - F(x_i)}{F(x_{i+1}) - F(x_i)}(x_{i+1} - x_i). \tag{2.29}$$

This approximation is often too rough to be used, especially when the interpolation grid is sparse.

If linear interpolation on a linear scale is adequate, the PDF can be expressed as

$$f(x) = f(x_i) + a_i(x - x_i), \tag{2.30}$$

where the interpolation coefficient $a_i$ is given by

$$a_i = \frac{f(x_{i+1}) - f(x_i)}{x_{i+1} - x_i}. \tag{2.31}$$

The CDF is simply given by

$$F(x) = F(x_i) + (f(x_i) - a_i x_i)(x - x_i) + \frac{1}{2}a_i(x^2 - x_i^2). \tag{2.32}$$

For $a_i \neq 0$, the inverse function is a quadratic equation, which has two roots. The root which satisfies Eq. (2.26) is given by

$$x = x_i + \frac{1}{a_i}\left(\sqrt{[f(x_i)]^2 - 2a_i[F(x_i) - \xi]} - f(x_i)\right). \tag{2.33}$$

For $a_i = 0$, the random value is simply given by

$$x = x_i + \frac{\xi - F(x_i)}{f(x_i)}. \tag{2.34}$$

It's clear that if an $n$th order polynomial is used for interpolation, the random value is a root of a polynomial with an order of $n + 1$.

When linear interpolation on a log-log scale is used, the PDF is given by

$$f(x) = \exp\left[\ln f(x_i) + c_i(\ln x - \ln x_i)\right] = f(x_i)\left(\frac{x}{x_i}\right)^{c_i}, \qquad (2.35)$$

where the interpolation coefficient $c_i$ is given by

$$c_i = \frac{\ln f(x_{i+1}) - \ln f(x_i)}{\ln x_{i+1} - \ln x_i}. \qquad (2.36)$$

For $c_i \neq -1$, the CDF can be expressed as

$$F(x) = F(x_i) + \frac{x_i f(x_i)}{c_i + 1}\left[\left(\frac{x}{x_i}\right)^{c_i+1} - 1\right]. \qquad (2.37)$$

The random value $x$ obtained from the inverse function is now given by

$$x = x_i\left[(1 + c_i)\frac{\xi - F(x_i)}{x_i f(x_i)} + 1\right]^{\frac{1}{1+c_i}}. \qquad (2.38)$$

In the case of $c_i = -1$, the CDF becomes

$$F(x) = F(x_i) + x_i f(x_i)\ln\left(\frac{x}{x_i}\right), \qquad (2.39)$$

and the random value is given by

$$x = x_i \exp\left(\frac{\xi - F(x_i)}{x_i f(x_i)}\right). \qquad (2.40)$$

### 2.2.4 Multivariate random sampling and composition method

In the case of a joint distribution of two random variables $X$ and $Y$, the PDF can be expressed using Eq.(2.13) as

$$f_{X,Y}(x, y) = f_Y(y)f_{X|Y}(x|y). \qquad (2.41)$$

To create a random variate pair $x$ and $y$, $y$ is first drawn from $f_Y(y)$ and $x$ is then sampled using $f_{X|Y}(x|y)$. This can easily be generalized to any number of random variables.

Another useful sampling technique is the composition method which can be applied to discrete mixture of PDFs, i.e. the PDF of random variable $X$ can be expressed as

$$f_X(x) = \sum_i P(Z = z_i)f_i(x). \qquad (2.42)$$

To sample the random variable $X$, the index $i$ is first selected according to the discrete probability $P(Z = z_i)$ and the value $x$ is then drawn from the corresponding $f_i(x)$.

## 2.3   Cross section

As stated in the beginning of this section, the free path length which a particle travels between interactions, target type, interaction type, and the outcome of an interaction are all random variables. Here, we define the probability density functions for these random variables. We start from the important concept of differential cross section (DCS) which defines a PDF for the outcome of a scattering interaction. This leads us to the concepts of microscopic and macroscopic cross sections which define the probabilities of interaction and target types in a macroscopic medium. Finally, the probability density function for the path length is given.

### 2.3.1   Differential and microscopic cross section

Consider an idealized scattering experiment illustrated in Fig. 2.1 where a mono-directional, mono-energetic beam of particles is directed at a target (e.g., an atom). Assume that only one interaction type is possible with the target. The number of incident particles per unit area per second is given by the beam intensity $I$. Some of the particles are scattered by the target while others pass the target without interacting. In spherical coordinates, the direction of each scattered particle is determined by the polar scattering angle $\theta \in [0, \pi]$ and the azimuthal scattering angle $\phi \in [0, 2\pi]$. Let the number of particles scattering into a solid angle $d\Omega$ around $(\theta, \phi)$ with an energy in the interval $(E', E' + dE')$ per unit time be $dN(\theta, \phi, E')/dt$, assuming that only the scattered particles are counted. The double differential cross section (DDCS) is defined as

$$\frac{d^2\sigma}{d\Omega dE'} = \frac{dN(\theta, \phi, E')/dt}{I d\Omega dE'}. \tag{2.43}$$

This quantity has the dimensions of area per energy per solid angle. The probabilistic interpretation of the DDCS should be clear from the definition; it is the unnormalized joint PDF of the random variables $\theta$, $\phi$ and $E'$. The existence of such a probability distribution can be understood as a result of the probabilistic nature of quantum physics. In general, a DDCS is a function of the energy of the incident particle. The energy-dependence is assumed throughout this work without explicitly stating it.

The differential cross section can also be a single-variate or multi-variate instead of bivariate as defined here. For example, the direction of a secondary particle generated in the interaction can be another random variable. Also, the concept of differential cross section is not limited only to scattering interactions, and it can be used, for example, for defining the distribution of energies and directions of particles generated in an absorption interaction.

To obtain a single differential cross section with respect to the solid angle, Eq. (2.43) is integrated over all possible scattering energies:

$$\frac{d\sigma}{d\Omega} = \int \frac{d^2\sigma}{d\Omega dE'} dE'. \tag{2.44}$$
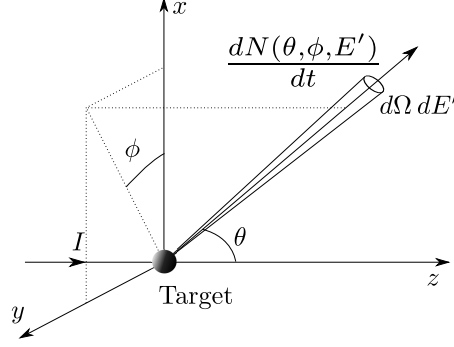
Figure 2.1: Schematic of a scattering event.

Likewise, the single differential cross section with respect to the energy of the scattered particle is given by

$$\frac{d\sigma}{dE'} = \int \frac{d^2\sigma}{d\Omega dE'} d\Omega, \tag{2.45}$$

where the differential solid angle in the spherical coordinate system is given by

$$d\Omega = \sin\theta d\theta d\phi. \tag{2.46}$$

The probabilistic interpretation of these single differential cross sections is that they are the unnormalized marginal PDFs of the direction and energy of the scattered particle, as defined in Eq. (2.12). Although Eq. (2.44) is actually an unnormalized PDF of the random variables $\theta$ and $\phi$, the direction of particle is considered as a single variable, and hence Eq. (2.44) is called a single-differential cross section.

Integrating the DDCS over all energies and angles yields the quantity

$$\sigma = \iint \frac{d^2\sigma}{d\Omega dE'} d\Omega dE', \tag{2.47}$$

which is called the microscopic cross section, expressed in units of barns ($10^{-24}$ cm$^2$). The important interpretation of the microscopic cross section is that it gives the probability that the interaction occurs between a single particle and the target. Now consider that the idealized scattering experiment is extended into multiple interaction types with the target. There could be multiple scattering interactions, each characterized by a DDCS, and also absorption processes. Each interaction type is characterized by a microscopic cross section, so that the probability for an interaction type $i$ can be written as

$$P_i = \frac{\sigma_i}{\sum_j \sigma_j} = \frac{\sigma_i}{\sigma_{\text{tot}}}. \tag{2.48}$$

The quantity $\sigma_{\text{tot}}$ is called the total microscopic cross section, which now gives the probability that any type of interaction occurs between a single particle and the target.

Often, we are interested only in the $\theta$-dependence of the differential cross section, e.g., when a photon is considered to be randomly polarized. Using (2.46), the differential cross section with respect to the polar scattering angle becomes

$$\frac{d\sigma}{d\theta} = \int_0^{2\pi} \frac{d\sigma}{d\Omega} \sin\theta d\phi = 2\pi \sin\theta \frac{d\sigma}{d\Omega}, \qquad (2.49)$$

where the last equality holds only if the integrand is independent of $\phi$. The cosine of $\theta$ is often used as variable instead of $\theta$, denoted by

$$\mu \equiv \cos\theta. \qquad (2.50)$$

The corresponding differential cross section reads as

$$\frac{d\sigma}{d\mu} = \int_0^{2\pi} \frac{d\sigma}{d\Omega} d\phi = 2\pi \frac{d\sigma}{d\Omega}. \qquad (2.51)$$

When defined as above, the integration limits are reversed, i.e. the total cross section is given by

$$\sigma = \int_{-1}^{1} \frac{d\sigma}{d\mu} d\mu. \qquad (2.52)$$

Because $\sigma^{-1}$ can be seen as a normalization constant, the PDF of $\mu$ can be expressed as

$$f(\mu) = \frac{2\pi}{\sigma} \frac{d\sigma}{d\Omega}. \qquad (2.53)$$

Differential cross sections can be obtained from theoretical models or derived from experimental results, and are presented in analytical form or as tabulated data. The theoretical treatment of differential cross sections often involves different quantum mechanical models of scattering. We do not need to understand the complicated theoretical models or experimental setups in the context of this work; it is sufficient to know that there exists adequate ways to obtain accurate probability distributions of interactions.

### 2.3.2 Macroscopic cross section

The differential and the microscopic cross section discussed in the previous section characterize the interaction in the case of a single target, but are not enough for describing the actual transport process. The macroscopic object where the particle travels consists of a large number of different types of targets, each having different differential cross sections. The material-dependent quantity called the macroscopic cross section is presented here, which leads us to an important result of the distribution function of the travelled distance between interactions.

Consider an object made of a homogeneous material consisting of multiple target types $t$, each with a number density $n_t$ and microscopic cross section $\sigma_{t,i}$ related to the interaction type $i$. A beam with an intensity $I$ hits the object on an area

*A* perpendicular to the beam direction. Let's examine a small volume *Ads* in the object where *ds* is a small distance parallel to the beam direction. The number of targets of type $t$ in the volume is $n_t Ads$, and hence the number of interactions of type $i$ with a target type $t$ per unit time is $I n_t \sigma_{t,i} Ads$. The material-dependent part of this reaction rate is the macroscopic cross section, defined as

$$\Sigma_{t,i} = n_t \sigma_{t,i}. \tag{2.54}$$

Summing over all target and interaction types gives the total macroscopic cross section in the material:

$$\Sigma_{\text{tot}} = \sum_t \sum_i \Sigma_{t,i} = \sum_t \Sigma_{t,\text{tot}}. \tag{2.55}$$

The total number of interactions in the volume per unit time and area is therefore $I\Sigma_{\text{tot}} ds$ which corresponds to the decrease in the intensity by

$$dI = -I\Sigma_{\text{tot}} ds. \tag{2.56}$$

Solving this differential equation gives the beam intensity in the object as

$$I(s) = I(0)e^{-\Sigma_{\text{tot}}s}. \tag{2.57}$$

The intensity of the beam therefore decreases exponentially in the object.

It's clear that the quantity $I(s)/I_0$ gives the probability that a particle has not interacted in a travelled distance $s$. The probability that an interaction occurs at a differential distance $ds$ is $\Sigma_{\text{tot}} ds$. Therefore, the probability that a particle travels a distance $s$ without any interaction and then interacts in the next $ds$ is given by the product $e^{-\Sigma_{\text{tot}}s}\Sigma_{\text{tot}} ds$. Hence, the PDF for the travelled distance $s$ is given by

$$f(s) = \Sigma_{\text{tot}} e^{-\Sigma_{\text{tot}}s}. \tag{2.58}$$

The mean of the random variable $s$ is given by

$$\langle s \rangle = \int_0^\infty s \Sigma_{\text{tot}} e^{-\Sigma_{\text{tot}}s} ds = \frac{1}{\Sigma_{\text{tot}}} \equiv \lambda, \tag{2.59}$$

which is called the mean free path.

In summary, the macroscopic total cross section completely specifies the probability distribution of the distance between interactions in a macroscopic object. The inverse of $\Sigma_{\text{tot}}$ is the average path length between interactions. Macroscopic cross section also gives the interaction probability per unit path length. Therefore, because $\Sigma_{j,\text{tot}} ds$ is the probability that a particle interacts with a target type $j$ in a distance $ds$, the probability for an interaction with a target type $j$ is given by

$$P_j = \frac{\Sigma_{j,\text{tot}}}{\Sigma_{\text{tot}}}. \tag{2.60}$$

## 2.4   General method for the Monte Carlo particle transport

So far, we have discussed how random variates can be generated from probability distributions, and what kind of distributions are encountered when particles travel in a macroscopic medium. Here, we combine some of these results and describe the general method for the Monte Carlo particle transport.

Some assumptions are required for the Monte Carlo transport method to be valid. First of all, the geometry where the particles travel is considered to consist of homogeneous material regions with well-defined boundaries. This restriction is imposed in order to be able to sample the free path length, and is not a restriction of the Monte Carlo method itself. The medium in each material region consist of a large number of uniformly distributed targets with which the particles interact. Any possible interactions of the simulated particles with themselves are insignificant compared to the interactions with the targets in the medium. The interactions are considered to be point-like with single targets, meaning that a particle track between two subsequent interactions is a straight line. Therefore, the scattering from several scattering centres is neglected. The movement of each particle is considered to be a random walk process with the Markov property, which means that only the current state of the particle has an effect on the future states of the particle.

Thanks to the assumptions mentioned above, the transport of particles can be simulated independently from each other. Each particle starts from a given state, which is defined by the location of the particle $\mathbf{r}_0$, the unit direction vector $\hat{\boldsymbol{\Omega}}_0$, and the energy $E_0$. These values could be, for example, sampled from a known distribution. Assume now that a particle has a state $i$, i.e. $\mathbf{r}_i$, $\hat{\boldsymbol{\Omega}}_i$, $E_i$. The free path length $s$, which the particle travels until the next interaction occurs, is a random variable which has a PDF given by Eq. (2.58). This is an exponential distribution which has a sampling formula given by Eq. (2.17). Once the free path length has been generated, the interaction location and the new position of the particle is given by

$$\mathbf{r}_{i+1} = \mathbf{r}_i + s\hat{\boldsymbol{\Omega}}_i. \tag{2.61}$$

The target and interaction type are both discrete random variables with probabilities given by Eqs. (2.60) and (2.48), respectively. Both can be sampled using the method for a discrete distribution discussed in Sec. 2.2.1.

Once the interaction and target types have been selected, the interaction itself is modelled. Naturally, the outcome depends on the nature of the interaction, but in general, interactions are divided into two groups: scattering reactions and absorptions. In a scattering interaction the direction and possibly the energy of the particle are changed. Again, both of these are random variables which joint PDF is determined by the double differential cross section. The direction and energy of the scattered particle can be sampled as described in Sec. 2.2.4 by first using a marginal distribution given by Eq. (2.44) or (2.45) and then the corresponding conditional distribution. In the case of absorption, the particle track is simply terminated. In both cases, secondary particles are generated if needed, and their directions and energies are

sampled from the distributions determined by the interaction physics. The particle track is also terminated if some stopping criterion is met, e.g., if the energy of the particle after a scattering event is below some cutoff value, or the particle travels outside the system boundaries. If the particle track is not terminated, a new direction vector $\hat{\boldsymbol{\Omega}}_{i+1}$ and energy $E_{i+1}$ are set. The new direction vector is calculated from the sampled scattering angles $\theta$ and $\phi$ and the old direction vector $\hat{\boldsymbol{\Omega}}_i$ using rotations. The process is then repeated for the new particle state $i+1$ until the particle track is terminated due to one of the reasons mentioned above.

One important factor not mentioned yet is how different material regions affect the particle transport process. As mentioned, the usual approach to present a geometry is to construct it from different types of geometrical objects with well-defined boundaries, each composed of some homogeneous material characterized by the macroscopic total cross section. When a particle crosses a boundary surface, the free path length sampled in the first material is not statistically correct in the second one, because the free path length depends on the macroscopic total cross section. Traditionally, a new free path length is sampled if the particle crosses a material boundary. This can become computationally expensive because it requires the calculation of the distance to the nearest boundary surface. Another, often faster approach is to use a statistically equivalent delta-tracking method [17] which eliminates the need for surface tracking, but introduces some limitations to the result estimation [18]. The delta-tracking method is usually faster in complicated geometries with a large number of surfaces.

The description of the Monte Carlo transport method given above is a rather simplified one, and does not involve all the sophisticated details. What should be kept in mind is that the accuracy of the Monte Carlo transport method is mostly determined by how well the interaction physics are modelled, together with the accuracy of the used data. Approximations are often needed to simplify the treatment of interactions and to speed up the computation. In general, the purpose of the code determines the needed level of details in order to produce accurate enough results in comparison to experimental measurements.

# 3 Photon interactions

A photon is the force carrier of the electromagnetic interaction which is one of the four fundamental interactions of nature, the other three being gravitational, strong nuclear and weak nuclear interactions. It is a stable, massless, and chargeless quantum of electromagnetic radiation. Photons are emitted and absorbed through various processes, for example, in electromagnetic interactions between charged particles, transitions between atomic or nuclear energy levels, and annihilation of particles and their antiparticles. Photons can also scatter from charged particles and generate secondary photons and charged particles through their interactions, which makes the accurate modelling of photon transport process challenging.

Like all elementary particles, photons exhibit the wave–particle duality meaning that they display both wave- and particle-like properties. On the one hand, a photon can be seen as an electromagnetic wave as derived from the Maxwell's equations. In this picture, the electromagnetic wave is characterized by its wavelength $\lambda$, the propagation direction $\hat{\mathbf{k}}$, and the polarization state which describes the orientation of the electric field component of the wave. The frequency $f$ of the wave is related to the wavelength by

$$f = \frac{c}{\lambda},\tag{3.1}$$

where $c$ is the speed of light in vacuum. The propagation direction is the unit vector of the wave vector $\mathbf{k}$ which is given by

$$\mathbf{k} = k\hat{\mathbf{k}} = \frac{2\pi}{\lambda}\hat{\mathbf{k}}.\tag{3.2}$$

The other side of the coin is the particle nature, which means that a photon can be seen as a single quantum of electromagnetic radiation having an energy $E_{\mathrm{k}}$ and a momentum $\mathbf{p}$. The energy of a photon and the frequency of the corresponding electromagnetic wave are connected as

$$E_{\mathrm{k}} = hf = \frac{hc}{\lambda},\tag{3.3}$$

where $h$ is the Planck constant. The momentum of a photon is given by

$$\mathbf{p} = \hbar\mathbf{k},\tag{3.4}$$

where $\hbar = h/2\pi$ is the reduced Planck constant. The electromagnetic spectrum is traditionally divided into different classes by the wavelength, for example, into visible light, X-rays, and gamma rays. Also, the classification can be based on the source of the radiation. For example, X-rays are generated by electronic transitions whereas gamma rays are produced by nuclear processes. However, such classification of photons is not used in the context of this work.

The way a photon interacts with matter depends strongly on the energy. When the photon energy is below about 1 keV, the wave nature of the photon dominates and
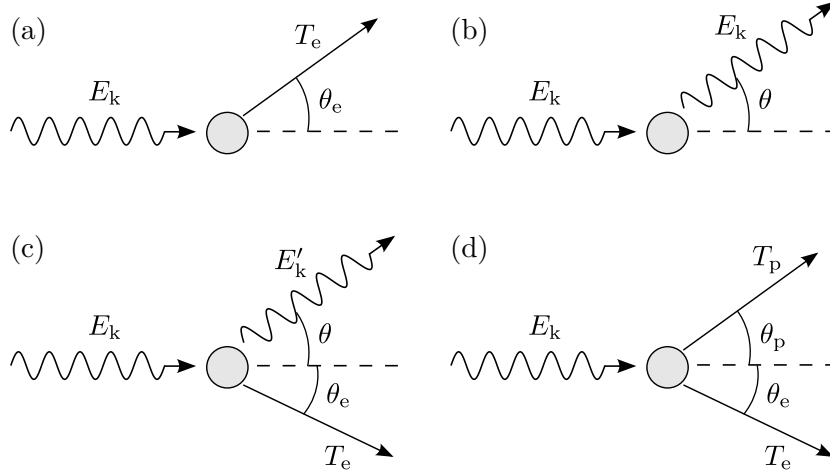
Figure 3.1: Schematics of the four main photon interactions with matter: (a) photoelectric effect, (b) Rayleigh scattering, (c) Compton scattering, and (d) electron-positron pair production. In the figure, $E_k$ is the energy of the incident photon, $E'_k$ is the energy of the scattered photon, $\theta$ is the polar scattering angle of the photon, $T_e$ and $T_p$ are the energies of the emitted electron and positron, and $\theta_e$ and $\theta_p$ are the polar emission angles of the electron and positron. Note that for Rayleigh scattering $E'_k$ is equal to $E_k$.

the photon interacts with the matter as a whole. Interactions can then strongly depend on different material properties, such as molecular effects, lattice structure or conductivity [19]. The classical theory of electromagnetic radiation can then be used to predict the behaviour of photons, at least to some extent. At energies above about 1 keV, when the wavelength of a photon is smaller than the atomic dimensions [19], the particle nature of photons dominates and the interactions with matter can be modelled as they would occur with free atoms. The Monte Carlo method presented in the previous section can then be applied for simulating the transport of photons using physical models describing interactions with free atoms.

The 1 keV energy is not a strict limit for using the Monte Carlo method in photon transport problems, but is often applied as a cutoff energy $E_{cut}$ because the accuracy of free atom cross sections decreases at energies below 1 keV or so [20]. Often, the Monte Carlo method is used for photons with energies above a few tens of keV to calculate, for example, spectrum or deposited energy of photons in some geometry. Low-energy photons can usually be ignored because they are absorbed in relatively short distances, and they do not contribute much to the spatial distribution of deposited energy.

Above 1 keV or so, the transport process of photons can be accurately modelled with only four interaction processes, which are the photoelectric effect, Rayleigh scattering, Compton scattering, and pair production. The schematics of the interaction types together with the variables related to them are shown in Fig. 3.1. The photoelectric effect results in the absorption of the photon and emission of an atomic electron. In Rayleigh scattering, which is elastic scattering from the atomic electrons, the

direction of the photon is changed whereas the energy remains the same. In Compton scattering, which is the inelastic scattering from an atomic electron, both the energy and direction of the photon are changed, and the reduced energy of the photon is given to the electron which is ejected from the atom. In pair production, the photon is destroyed in the field of nucleus or an electron, and an electron-positron pair is created. Other interaction processes are also possible, such as different photonuclear interactions and photoexcitations, but these are relatively rare and are needed to be considered only in special applications.

New photons are also often generated in secondary processes related to the mentioned interaction types. In the photoelectric effect and Compton scattering, a vacancy is generated in an electron shell due to the emission of the electron, and a part of the photon energy is lost due to the electron binding energy. However, this lost energy can be recovered in the form of photons and electrons in a process called atomic relaxation. The generated vacancy is filled in a series of transitions of electrons from outer shells, resulting in a cascade of fluorescence photons and Auger electrons. The atomic relaxation process is discussed in more detail in Sec. 4. Another source of new photons is the electron-positron annihilation discussed in Sec. 3.5.3, in which an electron and a positron are destroyed and a pair of new photons is created. The third important source of photons is bremsstrahlung which is the braking radiation emitted by charged particles — in our case electrons and positrons — as they slow down in the medium. The number of emitted bremsstrahlung photons and their energy distribution depend strongly on the energy of the electron; the phenomenon is important in the MeV range and above, especially in heavy elements. In order to estimate the bremsstrahlung radiation correctly, the energy and angular distributions of electrons and positrons created in different processes have to be taken into account. As mentioned in the introduction of this thesis, electron transport is a very complicated topic and is not implemented as a part of this work. Instead, the bremsstrahlung radiation is taken into account with a so-called thick-target bremsstrahlung (TTB) approximation, which is discussed in Sec. 5.5. It is important to note that the TTB approximation is quite a crude one; for example, the angular distribution of bremsstrahlung photons is omitted.

A schematic of the photon transport algorithm used in Serpent is illustrated in Fig. 3.2, which shows the connections between the four main photon interactions and the related secondary processes. Because the outputs of the photon interactions and secondary processes are random variables, even a simple uniform source can result in a shower of photons, electrons, and positrons with complex energy and directional distributions. For example, a high-energy photon can undergo a pair production event which results in two annihilation photons and possibly multiple bremsstrahlung photons. These photons can, for example, Compton scatter multiple times before being absorbed in the photoelectric effect, which in turn may result in fluorescence photons. These complicated random walks can be simulated in high detail with the Monte Carlo method, which in turn results in accurate estimates of the desired macroscopic variables.
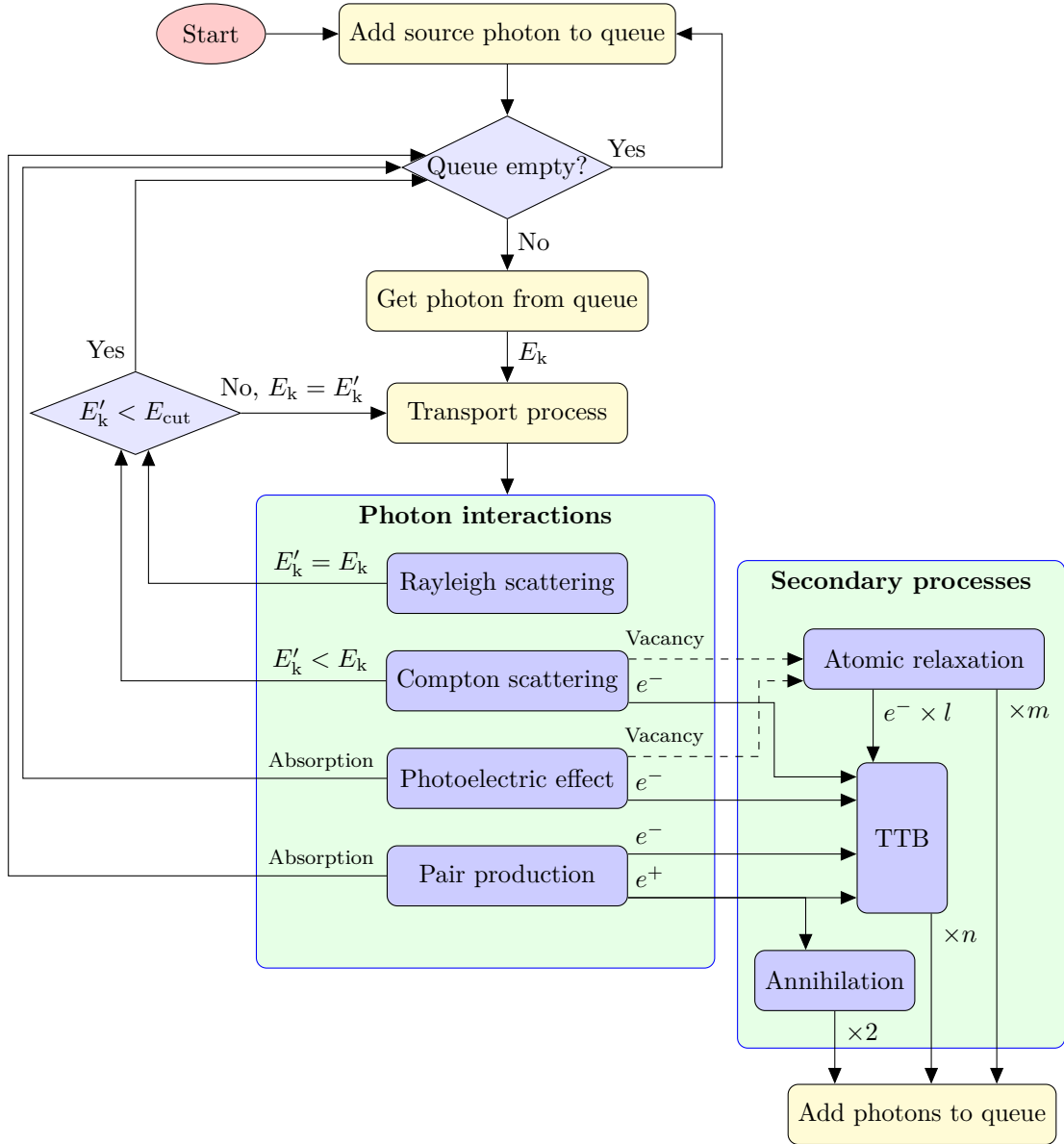
Figure 3.2: Simplified flow chart of the photon transport algorithm used in Serpent. One of the four photon interactions is selected in the transport process. The secondary processes are simulated right after the selected photon interaction. In the secondary processes, $l \in \mathbb{N}_0$ and $m \in \mathbb{N}_0$ represent the number of Auger electrons and fluorescence photons created in the atomic relaxation process, respectively, and $n \in \mathbb{N}_0$ is the number of bremsstrahlung photons produced by the TTB approximation. Electron-positron annihilation generates two photons. It is assumed that the energies of the secondary photons are above the cutoff energy $E_{\mathrm{cut}}$. Note that the outputs of the photon interactions and secondary processes are random variables. For example, the generated electrons are associated with energy and angular distributions.

Figure 3.2 can also be used to understand how the deposition of energy is handled in our model. The energy of a particle is deposited locally when it is below the cutoff energy $E_{\mathrm{cut}}$. This is carried out for Compton-scattered photons, electrons and positrons emitted in the interactions, and photons generated in the TTB and relaxation processes. However, in practice, only particles with energies above $E_{\mathrm{cut}}$ are created and thus, energy conservation is used for calculating the deposited energy in the TTB and atomic relaxation routines. In other words, the deposited energy is the energy lost by the interacting photon minus the energies of the generated fluorescence, bremsstrahlung, and annihilation photons.

The appropriate theoretical tool for describing the interactions between photons and matter is quantum electrodynamics (QED) which is the most accurate physical theory known. However, the predictions of QED cannot be given in an analytical form in general, and a comprehensive library of numerical results covering all the interactions over a wide energy range does not exist. Therefore, different approximate quantum mechanical models have been applied to obtain, for example, analytical differential cross sections. Much of the theoretical work behind these models is too broad to be covered in this work, and therefore is left out in most parts. Instead, the emphasis is on the practical use of differential cross sections and other results, i.e. presenting algorithms suitable for the Monte Carlo method. However, a variety of different models exist and are used in various Monte Carlo transport codes. Not only comparisons are needed between different models and experimental results, but also between different sampling algorithms. This can become a tedious task, and therefore, in most parts only the most important results are compared with the help of reviews and evaluations found in the literature.

One essential part of a photon transport model is the data needed for the interactions. Because vast and complex theoretical and computational work is needed for calculating, e.g., microscopic cross sections, such calculations are not performed in this work. Instead, we use the Evaluated Photon Data Library '97 Version (EPDL97) [20] for photon interactions when applicable. The EPDL97 is one of the most commonly used photon data libraries which includes interaction data for elements with atomic numbers between 1 and 100. The EPDL97 is available in the Evaluated Nuclear Data File (ENDF) format, and we use the EPDL97 data from the ENDF/B-VII.1-release [21]. However, not all the data needed for accurate modelling of the photon interactions are included in the EPDL97, and therefore, other sources of data are also used. The accuracy of the EPDL97 data is discussed and compared with other data sources when needed.

The assumptions of the Monte Carlo method discussed in Sec. 2.4 are considered to be valid in the energy range of our interest, which is from $E_{\mathrm{cut}} = 1$ keV to 100 MeV. The photon–matter interactions are assumed to occur with free atoms, and any molecular or similar effects are ignored. Also, photons are considered to be unpolarized which means that the plane of polarization of a photon is assumed to be entirely random. The polarization state of a photon can be taken into account (see, e.g., Refs. [7, 8]) but it is needed only in special applications.
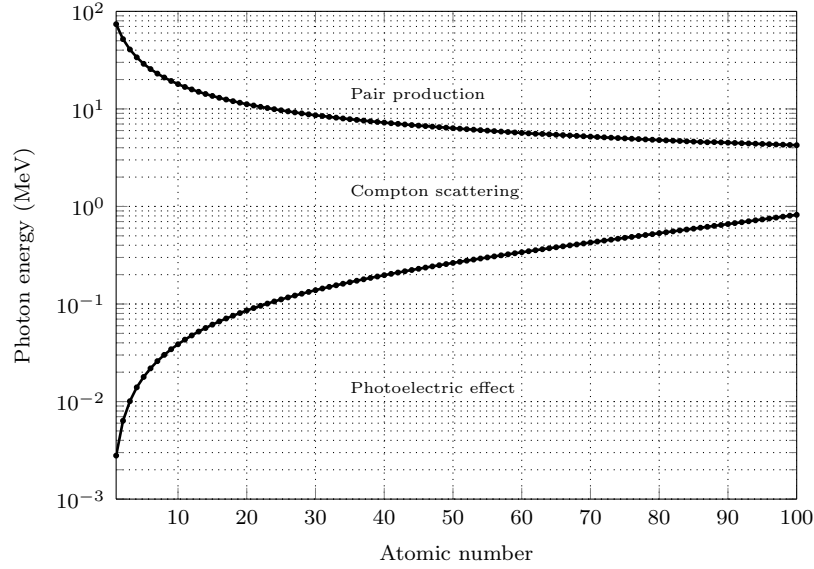
Figure 3.3: The importance regions of the photoelectric effect, Compton scattering, and pair production as a function of atomic number and photon energy. The cross sections of two interactions are equal at the plotted boundaries. Calculated from the cross section data given in the EPDL97 [20].

We first discuss the importance of the four main photon interactions as a function of photon energy and the atomic number $Z$. The energy and the $Z$-dependence of the interactions are important to know in order to understand the validity of the interaction models presented in the subsequent sections. The photoelectric effect, Rayleigh scattering, Compton scattering, and electron-positron pair production are discussed in Secs. 3.2, 3.3, 3.4, and 3.5, respectively.

## 3.1 Interaction cross sections

The importance regions of the photon interactions are shown in Fig. 3.3 as a function of energy and the atomic number. For all elements, the photoelectric effect dominates at low energies. As the energy increases, Compton scattering becomes the main interaction, and at very high energies pair production dominates. Rayleigh scattering is never the dominant interaction above 1 keV. The energy dependence of relative importances depends greatly on $Z$. For low-$Z$ elements, the photoelectric effect is the primary interaction up to energies between a few keV to a hundred keV or so. Compton scattering then dominates in a wide energy range up to about 10–70 MeV, after which pair production is the main interaction. For medium- and high-$Z$ elements, the photoelectric effect dominates up to hundreds of keV. The pair production becomes the primary interaction above about 4–5 MeV. Therefore, Compton scattering is especially important in material consisting of light elements, whereas the photoelectric effect and pair production are more significant in high-$Z$ materials.
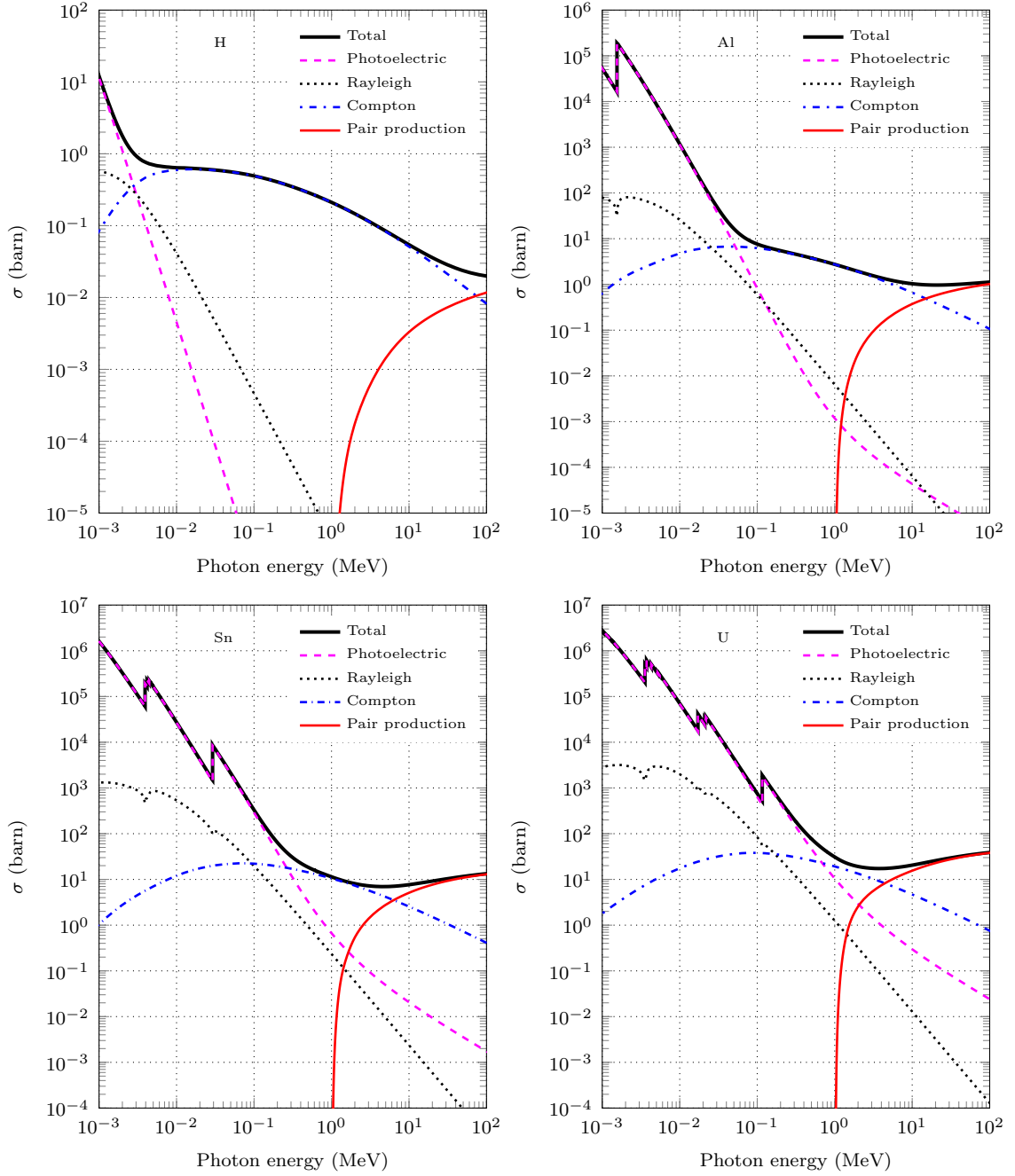
Figure 3.4: Microscopic cross sections of photon interactions as a function of photon energy for hydrogen ($Z = 1$), aluminium ($Z = 13$), tin ($Z = 50$), and uranium ($Z = 92$). The cross section data is from the EPDL97 [20].

The microscopic cross sections for the interactions and their sum, the total microscopic cross section, are presented in Fig. 3.4 as a function of energy for hydrogen, aluminium, tin, and uranium. The total cross section decreases with increasing energy in the photoelectric effect region, with the exception of the sharp peaks seen at the binding energies of electron shells. In the Compton scattering region, the decrease is much
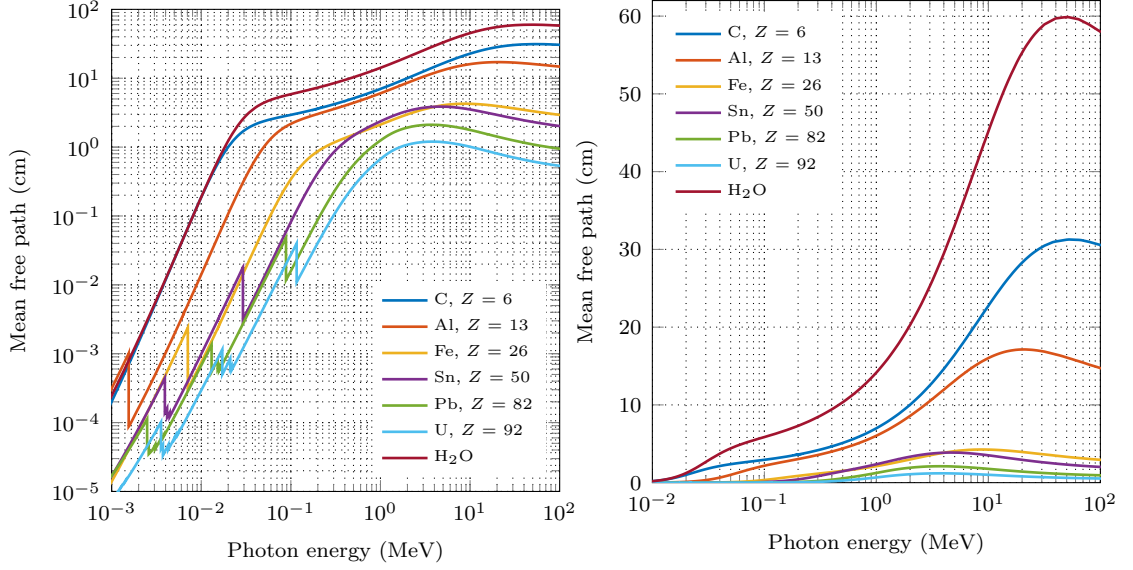
Figure 3.5: Log-log and lin-log plots of the mean free path $\lambda$ as a function of photon energy in some materials. Calculated from the cross section data of the EPDL97 [20].

smaller. The total cross section increases slightly when pair production begins to dominate. The $Z$-dependence of the importances of the interactions observed in Fig. 3.3 is also seen in Fig. 3.4. Another important observation is that the cross sections of all the interactions types increase with the atomic number.

To illustrate the effect of total cross section and material density on the photon range, the mean free path $\lambda$ given by Eq. (2.59) is plotted in Fig. 3.5 for graphite, aluminium, iron, tin, lead, uranium, and water. The atom density for the mean free path is given by

$$n = \frac{N_A \rho}{A_M}, \tag{3.5}$$

where $N_A$ is the Avogadro constant, $\rho$ is the mass density, and $A_M$ is the atomic weight. The mean free path first increases with the energy, with the exception of the sharp decreases just above the electron binding energies. Above a few MeV, the mean free path decreases due to pair production, except in light elements. Major differences can be seen between the elements in the whole energy range. Below a few hundred keV, photons are absorbed in much shorter distances in heavy elements because the photoelectric effect dominates at those energies. For example at about 20 keV, the mean free path in graphite is about 1 cm which is over three orders of magnitude larger than in uranium. Notable differences also exist between medium- and high-$Z$ elements, e.g., the mean free path is over 20 times larger in iron than in lead at 100 keV. Above a few MeV, the value of $\lambda$ is of the order of 1 cm or less in the middle- and high-$Z$ elements, whereas in graphite and aluminium it is between about 10 and 30 cm. In water, the mean free path is as large as 60 cm at about 50 MeV. One conclusion from this comparison is that heavy elements are better absorbers in general. However, the mean free path can't be used as a direct

measure of the absorption property of a material due to Compton scattering events and high-energy secondary photons generated in electron-positron annihilation and through bremsstrahlung.

## 3.2   Photoelectric effect

In the photoelectric effect, the photon is absorbed by an atomic electron, which is then emitted from an electron shell of the atom. The kinetic energy of the electron is equal to the photon energy minus the binding energy of the shell and the recoil energy of the atom. However, the recoil energy of the atom is small due its large mass and therefore can be ignored. Thus, the kinetic energy of the emitted photoelectron is given by

$$T_{\mathrm{e}} = E_{\mathrm{k}} - E_{\mathrm{b},i}, \tag{3.6}$$

where $E_{\mathrm{b},i}$ is the binding energy of the shell $i$. This also sets a threshold energy for each shell above which the photoelectric effect can occur, and causes discontinuities in the atomic photoelectric cross section. The binding energies are therefore often called edge energies. The ejection of the electron results in a vacancy in the electron shell, which is filled by an outer shell electron, emitting a fluorescence photon or an Auger electron in the process.

The photoelectric effect is the primary interaction at low photon energies, and dominates up to hundreds of keV for heavy elements. This is due to the strong $Z$-dependence of the cross section, which is roughly between $Z^4$ and $Z^5$ per atom [19]. The calculation of shell cross sections is rather difficult — at least close to the binding energies — and therefore will not be discussed here. However, the general energy-behaviour of the cross section can be described by using the fact that the photoelectric effect can occur only with bound electrons due to kinematic reasons. When the photon energy is high compared to the closest binding energy below the photon energy, electrons appear to be almost free as seen by the photon. Therefore, the interaction probability can be assumed to decrease with increasing photon energy. Also, because the inner-shell electrons are more bound to the atom than the outer-shell electrons, their interaction probabilities can be expected to be higher. Indeed, these characteristics can be seen in Fig. 3.6, where the atomic photoelectric and shell cross sections have been plotted for uranium. The atomic cross section decreases with increasing energy, until the next binding energy is reached. The cross section then increases discontinuously, and the corresponding shell electrons become the most probable ones to interact. For example, about 80% of photoelectric interactions occur with the K-shell electrons above the K-edge [22].

The data needed for simulating the photoelectric effect consists of atomic and shell cross sections and binding energies. We use the photoelectric data given by the EPDL97 [20] which include cross sections for all subshells. The estimated maximum uncertainty of these cross sections are 5% between 1.0 and 5.0 keV, 2% between 5 and 100 keV, 1–2% between 0.1 and 10 MeV, and 2–5% between 0.01 and 100 GeV.
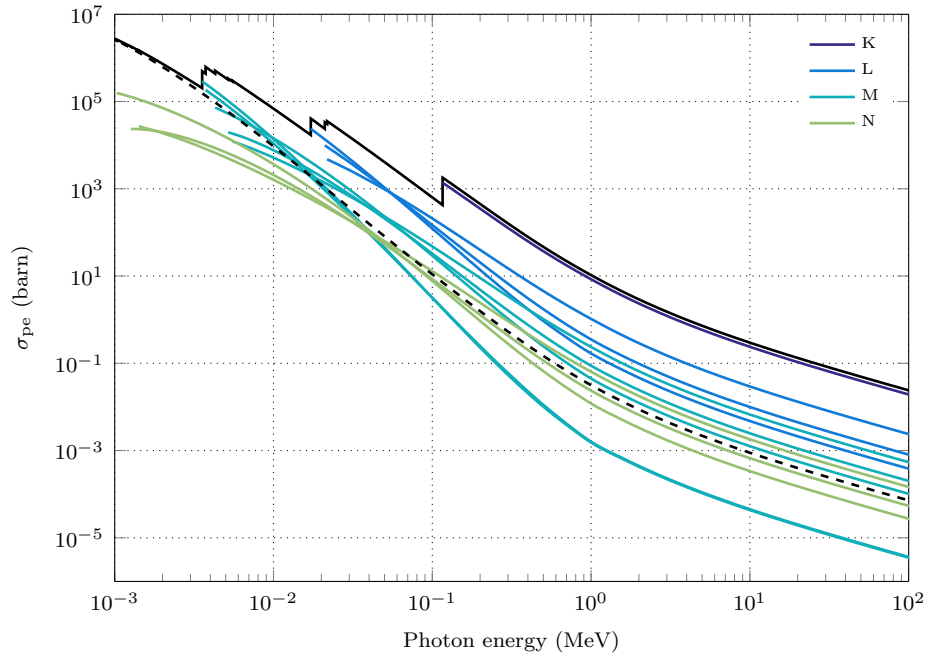
Figure 3.6: The atomic photoelectric cross section (black solid line) and cross sections for the K-, L-, M-, and N-shells of uranium. The black dashed line is the sum of the cross sections of the shells with binding energies below 1 keV. The cross section data is from the EPDL97 [20].
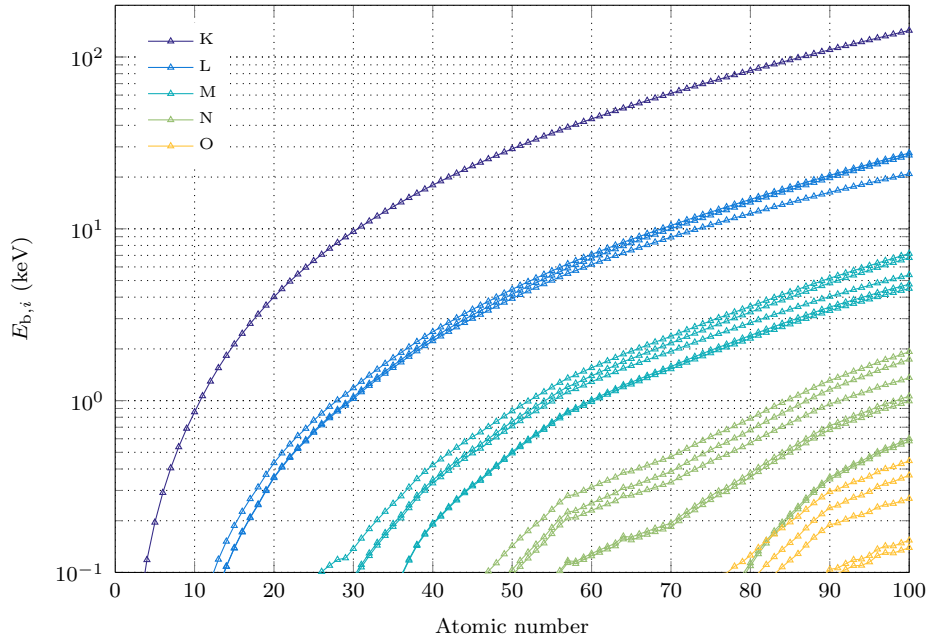


Figure 3.7: Electron binding energies above 100 eV for all the elements according to the EPDL97 [20].

At energies below 1 keV, the uncertainties are between 10 and 1000%. The atomic and inner-shell cross sections given by the EPDL97 are compatible with experimental results [23], but inconsistencies have been detected in the outer-shell cross sections, although the discrepancies may be due to limited sources of experimental data.

The binding energies above 0.1 keV given by the EPDL97 are plotted in Fig. 3.7 for all the elements. All the binding energies above the cutoff energy $E_{cut} = 1$ keV increase as a function of the atomic number. The binding energies are above the cutoff for $Z \geq 11$ in the K-shell, for $Z \geq 28$ in the $L_1$-subshell, and for $Z \geq 30$ in the $L_2$- and $L_3$-subshells. In the five subshells of the M-shell, the binding energies exceed $E_{cut}$ when $Z$ is above between 53 and 61. The first four N-subshells increase above 1 keV for $85 \leq Z \leq 99$. Thus, the number of subshells we need to consider is zero for $Z < 11$, 1 for $11 \leq Z < 30$, 4 for $30 \leq Z < 53$, 9 for $61 \leq Z < 84$, and 13 for $Z = 99$ and $Z = 100$.

Some discrepancies have been detected between the EPDL97 binding energies and other tabulations. In a recent extensive evaluation of different tabulations of binding energies [24], the ones included in the EPDL97 were considered to have the worst accuracy. The reason behind this is that the EPDL97 binding energies are based on theoretical calculations, whereas other compilations are usually based on experimental data, such as those included in Ref. [25]. We have compared the binding energies given by the EPDL97 and Ref. [25], and the maximum absolute differences were detected for K-shell binding energies of high-$Z$ elements; the EPDL97 binding energies are about 0.4–0.6 keV higher. The absolute differences are much smaller for lighter elements and other shells, naturally. Although these differences shouldn't be important in respect of this work, they can be significant in applications where atomic relaxation is important, such as X-ray fluorescence [26].

### 3.2.1 Calculating the electron energy

When a photoelectric effect occurs, the first task is to sample the electron shell, after which the energy and direction of the electron can be calculated. The electron is then used for the TTB approximation as explained in Sec. 5.5. The vacancy left in the electron shell is treated with the atomic relaxation procedure discussed in Sec. 4. The angular distribution of the photoelectron is discussed in the next section.

Because the atomic photoelectric cross section $\sigma_{pe}$ is the sum of the shell cross sections, the interaction probability for the $i$th shell is given by

$$P_i = \frac{\sigma_{pe,i}}{\sigma_{pe}}, \tag{3.7}$$

where $\sigma_{pe,i}$ is the cross section of the $i$th shell. The electron shell can be sampled by forming a discrete CDF and then using the inverse transform method as described in Sec. 2.2.1. In order to form the CDF, the shell and atomic cross sections must be interpolated at the photon energy $E_k$. However, the shell cross sections given by the

EPDL97 all have separate energy tables, which would require a table search for each shell if used directly. In order to perform the table search only once, the shell cross sections were preprocessed by interpolating them to the energy grid of the atomic photoelectric cross section. Linear interpolation on a log-log scale was applied which is the recommended method [20]. The original energy grid for each shell is preserved, because the energy grid of the atomic cross section is composed of the energy grids of the shells. Therefore, no interpolation error is introduced, as long as the same interpolation method is used in the sampling method. Probability tables for all shells with binding energies above the cutoff energy $E_{\mathrm{cut}}$ are calculated before the beginning of the transport simulation. Only non-zero shell probabilities are stored, and the locations of the probability tables on the energy grid are determined by a separate index table.

In the sampling method, the complete CDF is not constructed because log-log interpolation is rather time-consuming due to the computation of the exponential function. Instead, the shell probabilities are interpolated starting from the innermost shell until the $i$th shell is accepted when

$$\xi \leq \sum_{j,E_{\mathrm{b},j} \geq E_{\mathrm{cut}}}^{i} \mathrm{P}_j, \tag{3.8}$$

where $\xi \sim unif(0,1)$. Here, it is assumed that $E_{\mathrm{b},j} < E_{\mathrm{k}}$. Because the innermost shells usually have the highest interaction probabilities, the number of interpolations needed is small, especially above the K-shell binding energy. For example, the number of interpolations needed in uranium for 0.2 MeV photons is about 1.6 on average. However, below the K-shell binding energy $E_{\mathrm{b,K}} \approx 0.116$ MeV the number of interpolations increases. For example at 0.1 MeV, about 4 interpolations are needed on average. If no shell with a binding energy above $E_{\mathrm{cut}}$ is accepted, i.e. if

$$\xi > \sum_{j,E_{\mathrm{b},j} \geq E_{\mathrm{cut}}} \mathrm{P}_j, \tag{3.9}$$

the whole photon energy is given to the electron, i.e. $T_{\mathrm{e}} = E_{\mathrm{k}}$. Otherwise, the electron energy is given by Eq. (3.6).

Once the atomic relaxation procedure for the vacancy and the TTB approximation for the electron have been carried out, the energy deposited in the photoelectric effect is calculated as

$$E_{\mathrm{dep,pe}} = E_{\mathrm{dep,AR}} + E_{\mathrm{dep,TTB}}, \tag{3.10}$$

where $E_{\mathrm{dep,AR}}$ and $E_{\mathrm{dep,TTB}}$ are the energies deposited in the atomic relaxation and TTB processes given by Eqs. (4.7) and (5.23), respectively. If the kinetic energy of the photoelectron is smaller than $E_{\mathrm{cut}}$, $E_{\mathrm{dep,TTB}}$ is equal to $T_{\mathrm{e}}$. If the whole photon energy was given to the electron, $E_{\mathrm{dep,AR}}$ is zero.

### 3.2.2 Angular distribution of photoelectrons

The direction of the photoelectron can be sampled once its energy has been determined. In the presented photon transport model, the direction of the electron determines the direction of possible bremsstrahlung photons. However, because the photoelectric effect is important only at relatively low energies, and low-energy electrons produce a small yield of low-energy bremsstrahlung photons, the angular distribution of photoelectrons may be insignificant. Nevertheless, the calculation of the photoelectron direction was included, because the model presented here is very simple, and the angular distribution could be needed if full electron transport was implemented in Serpent in the future.

The most commonly used model for the angular distribution of photoelectrons is the cross section given by Sauter [27], which was derived for relativistic K-shell photoelectrons for light elements. It has been implemented, e.g., in EGS5 [8], Geant4 [13] and PENELOPE [28] Monte Carlo codes. It is also possible to calculate the direction for L-shell electrons [29]. Due to a limited amount of experimental results, photoelectric angular distribution models have not been validated thoroughly [23]. When compared with more detailed theoretical results [30,31], the Sauter distribution agrees well for low-$Z$ elements, but deviates from them for high-$Z$ elements. These deviations can have an effect on thin target simulations [32]. However, the Sauter distribution should be sufficient for our purposes, because our photon transport model is not suitable for thin target calculations due to the neglecting of electron transport and the usage of the TTB approximation. Also, when considering electron transport calculations in thick targets, more accurate distribution is not often needed because the direction of the electron changes strongly in a very short path length compared with the mean free path of photons.

The angle-dependent part of the Sauter distribution for linearly polarized photons with a polarization direction $\boldsymbol{\epsilon}$ is given as [27]

$$\left(\frac{d\sigma_{\mathrm{pe}}}{d\Omega_{\mathrm{e}}}\right)_{\mathrm{Sauter}} \propto \frac{\sin^2\theta_{\mathrm{e}}}{(1-\beta_{\mathrm{e}}\cos\theta_{\mathrm{e}})^3}\left[\frac{\cos^2\phi_{\mathrm{e}}}{1-\beta_{\mathrm{e}}\cos\theta_{\mathrm{e}}} - \frac{1-\sqrt{1-\beta_{\mathrm{e}}^2}}{2(1-\beta_{\mathrm{e}}^2)}\cos^2\phi_{\mathrm{e}}\right.$$
$$\left. + \frac{(1-\sqrt{1-\beta_{\mathrm{e}}^2})^2}{4(1-\beta_{\mathrm{e}}^2)^{3/2}}\right], \tag{3.11}$$

where $d\Omega_{\mathrm{e}} = d\cos\theta_{\mathrm{e}}d\phi_{\mathrm{e}}$, $\theta_{\mathrm{e}}$ is the angle between the incident photon direction $\mathbf{k}$ and the emitted electron direction $\mathbf{v}_{\mathrm{e}}$, and $\phi_{\mathrm{e}}$ is the angle between the plane of $\mathbf{k}$ and $\mathbf{v}_{\mathrm{e}}$ and the plane of $\mathbf{k}$ and $\boldsymbol{\epsilon}$. The variable $\beta_{\mathrm{e}}$ is the ratio of the velocity of the electron to the speed of light

$$\beta_{\mathrm{e}} = \frac{|\mathbf{v}_{\mathrm{e}}|}{c} = \frac{\sqrt{T_{\mathrm{e}}(T_{\mathrm{e}}+2m_{\mathrm{e}}c^2)}}{T_{\mathrm{e}}+m_{\mathrm{e}}c^2}, \tag{3.12}$$

where $m_{\mathrm{e}}$ is the rest mass of electron and the second equality is obtained from the relativistic kinetic energy equation. We consider only unpolarized photons, in which
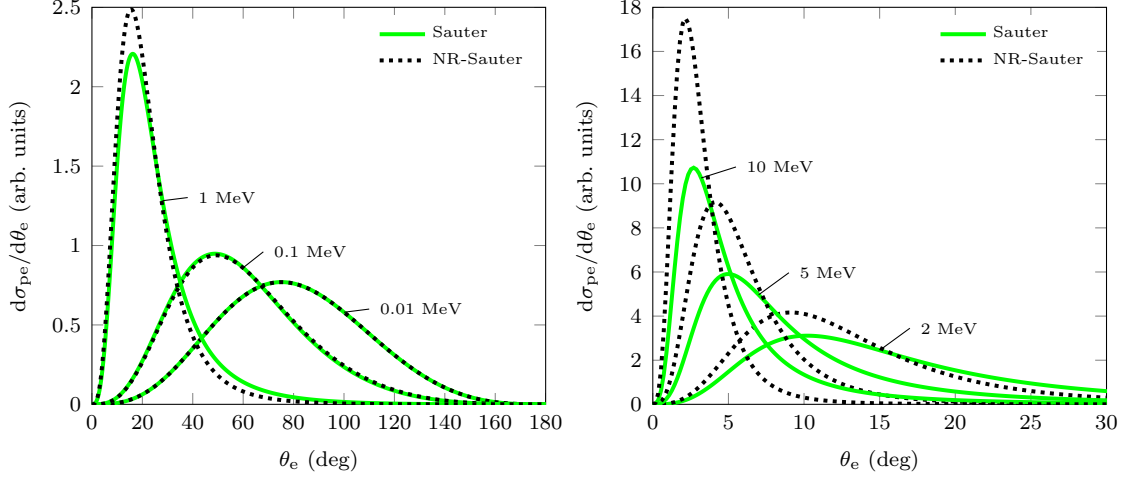
Figure 3.8: Normalized angular distribution of photoelectrons according to the Sauter distribution (3.14) and the non-relativistic approximation (3.15) for different electron kinetic energies.

case $\phi_e$ is uniformly distributed in the interval $[0, 2\pi]$. We can integrate Eq. (3.11) over this interval with respect to $\phi_e$, which gives

$$\left(\frac{d\sigma_{pe}}{d\cos\theta_e}\right)_{Sauter} \propto \frac{\sin^2\theta_e}{(1-\beta_e\cos\theta_e)^3}\left[\frac{1}{1-\beta_e\cos\theta_e} + \frac{3-2\beta_e^2-3\sqrt{1-\beta_e^2}}{2(1-\beta_e^2)^{3/2}}\right]. \quad (3.13)$$

Using the Lorentz factor $\gamma = (1-\beta_e^2)^{-1/2}$, Eq. (3.13) can be written in the simple form

$$\left(\frac{d\sigma_{pe}}{d\cos\theta_e}\right)_{Sauter} \propto \frac{\sin^2\theta_e}{(1-\beta_e\cos\theta_e)^4}\left[1 + \frac{1}{2}\gamma(\gamma-1)(\gamma-2)(1-\beta_e\cos\theta_e)\right]. \quad (3.14)$$

For non-relativistic electrons $\gamma \to 1$, in which case the Sauter distribution can be approximated as

$$\left(\frac{d\sigma_{pe}}{d\cos\theta_e}\right)_{Sauter,NR} \propto \frac{\sin^2\theta_e}{(1-\beta_e\cos\theta_e)^4}. \quad (3.15)$$

The Sauter distribution and the non-relativistic approximation are plotted in Fig. 3.8 for electron energies between 0.01 and 10 MeV. With small kinetic energies, most of the photoelectrons are ejected perpendicular to the direction of the incident photon [19]. When the kinetic energy increases, the angular distribution shifts to the forward direction while still always remaining zero at $\theta_e = 0°$. The non-relativistic distribution approximates very well the Sauter distribution below 1 MeV. With higher energies, the non-relativistic distribution tends to be more forward-shifted. However, close to 1 MeV and above, most of the electrons are ejected with small angles in both models. Moreover, at these energies, the photoelectric effect is important only for high-$Z$ elements. For our purposes, the non-relativistic approximation should be sufficient, because the TTB approximation most likely introduces more error to the angular distribution of bremsstrahlung photons.

The benefit of using the non-relativistic Sauter distribution is that it can be sampled faster and with a better efficiency. The algorithms developed for sampling the electron direction from Eq. (3.14) are quite inefficient. For example, the sampling algorithm used in PENELOPE has an efficiency of about 0.33 at low energies [7], whereas the algorithm used in Geant4 (G4PEEffectFluoModel) has an efficiency of about 0.5 when $T_e < m_e c^2$ and about 0.25 when $m_e c^2 < T_e < 2 m_e c^2$ [13]. Thus, we use the non-relativistic approximation for sampling the electron direction. The exact Sauter distribution should be used at high energies, say above 1 MeV, but the implementation is left for future work.

It is possible to sample $\cos \theta_e$ from Eq. (3.15) directly with the inverse transform method discussed in Sec. 2.2.1, which leads to finding a root of a third-order polynomial. However, a faster and simpler sampling algorithm can be obtained with the rejection sampling method discussed in Sec. 2.2.2. First, Eq. (3.15) is written as a PDF of the variable $\mu_e = \cos \theta_e$ as

$$f(\mu_e) = \frac{3}{2} \psi(\mu_e) g(\mu_e), \tag{3.16}$$

where

$$g(\mu_e) = \frac{1 - \beta_e^2}{2} \frac{1}{(1 - \beta_e \mu_e)^2}, \tag{3.17}$$

$$\psi(\mu_e) = (1 - \beta_e^2) \frac{1 - \mu_e^2}{(1 - \beta_e \mu_e)^2}. \tag{3.18}$$

In the interval [-1, 1], the function $g(\mu_e)$ is a normalized PDF of $\mu_e$ and the function $\psi(\mu_e)$ satisfies the condition $0 \leq \psi(\mu_e) \leq 1$. The variable $\mu_e$ can be sampled from the distribution $g(\mu_e)$ using the inverse transform method, which leads to a sampling formula

$$\mu_e = \frac{2\xi_1 + \beta_e - 1}{2\beta_e \xi_1 - \beta_e + 1}, \tag{3.19}$$

where $\xi_1 \sim unif(0, 1)$. We can now use the rejection sampling method by first sampling $\mu_e$ from Eq. (3.17) and then using Eq. (3.18) as a rejection function. The sampled $\mu_e$ is accepted if

$$\psi(\mu_e) \geq \xi_2$$
$$(1 - \beta_e^2) \frac{1 - \mu_e^2}{(1 - \beta_e \mu_e)^2} \geq \xi_2$$
$$4(1 - \xi_1)\xi_1 \geq \xi_2, \tag{3.20}$$

where $\xi_2 \sim unif(0, 1)$. It is clear that $\mu_e$ needs to be calculated from Eq. (3.19) only after $\xi_1$ has been accepted. The efficiency of this sampling method is 2/3 as indicated by Eq. (2.24). The azimuthal direction angle of the electron $\phi_e$ is sampled from a uniform distribution.

## 3.3   Rayleigh scattering

Rayleigh scattering is an elastic scattering mechanism of a photon from the electron cloud of an atom. The incident photon is scattered with a scattering angle $\theta$, and the target atom absorbs the transferred momentum without excitation or ionization. The recoil of the target atom is negligible due to its large mass, and hence the scattered photon has approximately the same energy as the incident one. In general, Rayleigh scattering is sharply peaked in the forward direction. The scattering angle decreases with increasing photon energy, but increases with $Z$. The atomic cross section for Rayleigh scattering is nearly always less than 10% of the total microscopic cross section [19]. The probability of a Rayleigh scattering event is at its highest at the energy range of 10–100 keV, depending on the target atom.

Rayleigh scattering is the main contributor to the elastic scattering of photons at most energies and scattering angles. Other components of elastic scattering, which stem from photonuclear interactions, are important only for large scattering angles at high energies [19]. Because Compton scattering and pair production dominate at high energies, and Rayleigh scattering is highly forward-directed, other elastic scattering components can be ignored. Often, the term "coherent scattering" is used instead of elastic scattering. In this context, coherence means that the relative phases of different scattering processes are preserved. However, using the term coherent scattering is somewhat ambiguous, because an elastic scattering process is not necessarily coherent, and coherent scattering can be inelastic.

### 3.3.1   Form factor approximation

A common way to formalize Rayleigh scattering is to extend the classically-predicted free point charge Thomson scattering to bound atomic electrons using form factors. Thomson scattering is derived by assuming that the electric field component of the incident wave sets the electron into a resonant oscillation. The oscillating electron in turn emits electromagnetic radiation due to its acceleration. The resulting differential cross section for unpolarized photons is given by [22]

$$\frac{d\sigma_{\mathrm{Th}}}{d\Omega} = \frac{r_{\mathrm{e}}^2}{2}(1 + \cos^2\theta), \tag{3.21}$$

where

$$r_{\mathrm{e}} = \frac{e^2}{4\pi\epsilon_0 m_{\mathrm{e}}c^2} \tag{3.22}$$

is the classical electron radius. However, the elastic scattering of a photon from atomic electrons can't be described accurately with the Thomson scattering because the atom is not a point charge, but instead, the atom has a certain charge distribution. In the form factor approximation, the differential cross section for Rayleigh scattering is expressed as

$$\frac{d\sigma_{\mathrm{R}}}{d\Omega} = \frac{d\sigma_{\mathrm{Th}}}{d\Omega}\left|F(\mathbf{q}, Z)\right|^2 = \frac{r_{\mathrm{e}}^2}{2}(1 + \cos^2\theta)\left|F(\mathbf{q}, Z)\right|^2, \tag{3.23}$$

where $F(\mathbf{q}, Z)$ is the atomic form factor which is a function of atomic number $Z$ and the momentum transfer vector

$$\hbar\mathbf{q} = \hbar(\mathbf{k} - \mathbf{k}'), \tag{3.24}$$

where $\mathbf{k}$ and $\mathbf{k}'$ are the wave vectors of the incident and scattered photon, respectively. The momentum transfer vector is the momentum obtained by the atom in the interaction. The atomic form factor represents a probability that the atomic electrons take up the recoil momentum without any energy loss of photon.

Formally, the form factor approach (3.23) can be derived by using the first-order Born approximation for the scattered wave function of the photon [33]. In the Born approximation, it is assumed that the effect of the scattering potential to the incident plane wave is small, which in practice means that the scattered wave function is approximated by a plane wave. The use of the Born approximation results in a scattering amplitude which is the amplitude of the Thomson scattering times the form factor $F_0(\mathbf{q}, Z)$, defined as [34]

$$F_0(\mathbf{q}, Z) = \sum_{j=1}^{Z} \left\langle \Psi_0 \left| e^{i\mathbf{q}\cdot\mathbf{r}_j} \right| \Psi_0 \right\rangle, \tag{3.25}$$

where $\Psi_0$ is the ground state wave function of the atom and $\mathbf{r}_j$ is the vector distance of the $j$th electron from the nucleus. The form factor can also be represented in the integral form [34]

$$F_0(\mathbf{q}, Z) = \int \rho(\mathbf{r}) e^{i\mathbf{q}\cdot\mathbf{r}} d^3\mathbf{r}, \tag{3.26}$$

where $\rho(\mathbf{r})$ is the electron number distribution. From the integral form it can be seen that the form factor is actually a Fourier transform of the spatial electron number distribution to the momentum space. Assuming a spherically symmetric atom, the form factor can be written as [34]

$$F_0(q, Z) = 4\pi \int_0^{\infty} \rho(r) \frac{\sin(qr)}{qr} r^2 dr, \tag{3.27}$$

where the electron number distribution is normalized as

$$4\pi \int_0^{\infty} \rho(r) r^2 dr = Z. \tag{3.28}$$

The distribution $\rho(r)$ is derived either from non-relativistic or relativistic wave functions, resulting in non-relativistic and relativistic form factors, respectively. Using $\mathbf{k}$ for the incident and $\mathbf{k}'$ for the scattered wave vector in Fig. 3.1b, we can obtain the magnitude of the momentum transfer vector and express $q$ as

$$q = k\sqrt{(1 - \cos\theta)^2 + \sin^2\theta} = k\sqrt{2 - 2\cos\theta} = 4\pi\sin(\theta/2)/\lambda, \tag{3.29}$$

where we have used the fact that the magnitudes of $\mathbf{k}$ and $\mathbf{k}'$ are equal. The form factor is often given as a function of the variable

$$x = \frac{\sin(\theta/2)}{\lambda} = \frac{E_{\mathrm{k}}}{hc}\sin(\theta/2) \tag{3.30}$$
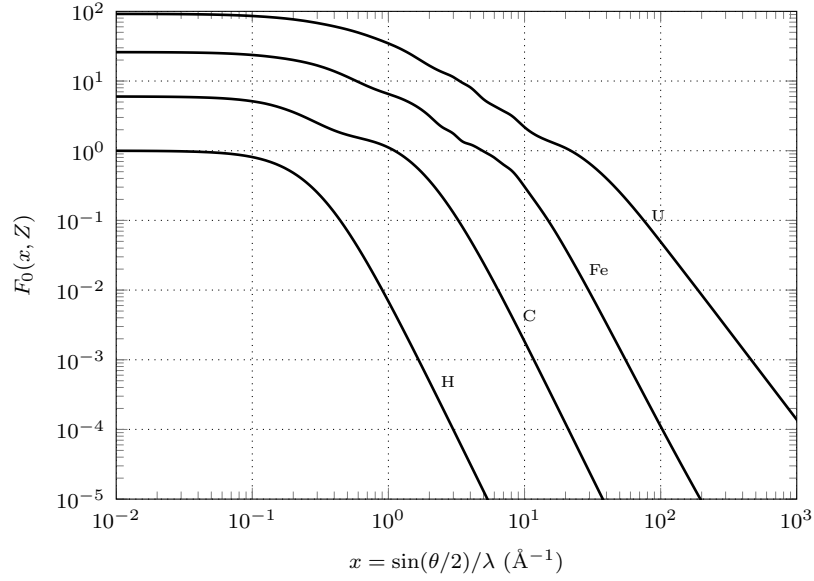
Figure 3.9: Non-relativistic atomic form factor as a function of the momentum transfer variable $x$ for hydrogen, carbon, iron, and uranium. The data is from the EPDL97 [20].

in the units of Å$^{-1}$.

The general energy and angle dependence of the atomic form factor can be seen from Eqs. (3.27) and (3.29). The behaviour of the form factor is also illustrated in Fig. 3.9 for four elements. When the scattering angle or the photon energy becomes small, $q \to 0$ and $\sin(qr)/(qr) \to 1$, and hence the form factor approaches $Z$. On the contrary, when the angle or the photon energy increases, the form factor decreases monotonically. The decrease is more rapid for low-$Z$ elements, which can be seen from Fig. 3.9.

The differential cross section for Rayleigh scattering according to the form factor approximation is plotted for hydrogen and uranium at four energies between 1 and 10 keV in Fig. 3.10. Also, the energy-independent Thomson cross section is shown in Fig. 3.10. At low energies, the differential cross section is close to Thomson scattering cross section multiplied by $Z^2$. As the photon energy increases, the peak of the differential cross section shifts more to the forward direction. The change is more rapid for low-$Z$ elements, which is due to the $Z$-dependence of the form factor. At high energies, the atomic cross section for Rayleigh scattering decreases as $E^{-2}$, which is caused by the $E^{-1}$ term in the form factor integral in Eq. (3.27).

### 3.3.2 Modified form factors and anomalous scattering factors

The form factor approximation, either non-relativistic or relativistic one, predicts the differential cross section adequately at energies above the K-shell binding energy for all angles in low-$Z$ and medium-$Z$ elements, and for small angles in high-$Z$ elements. However, it fails at energies close to and below the K-shell binding energy,
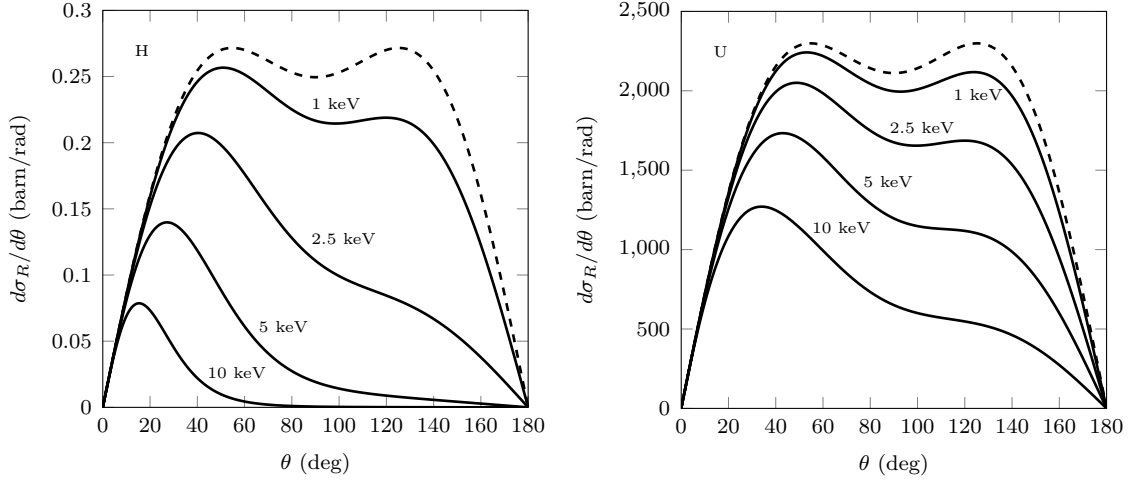
Figure 3.10: Differential cross section for Rayleigh scattering as a function of the polar scattering angle for hydrogen and uranium. The cross section for Thomson scattering multiplied by $Z^2$ is plotted in dashed line. The form factors used for calculating the cross sections were the non-relativistic ones given by the EPDL97 [20].

especially near the electronic transition energies [35]. Also, the error of the form factor approximation increases at small scattering angles for very high photon energies, notably for high-$Z$ elements [35]. The reason for the failure below the K-shell binding energy is that the form factor approximation doesn't take into account the effects related to the energy structure of the atom. The increasing error at small angles at high energies also indicates that the form factor approximation doesn't predict the high-energy limit of the Rayleigh scattering correctly. To reduce these errors, some modifications to the form factor approximation has been presented.

When electron binding energies are not small compared with $m_ec^2$, relativistic binding effects affect the Rayleigh scattering distribution. In order to take into account these effects, the modified relativistic form factor, or simply the modified form factor, has been represented [36]. In this model, the form factor is calculated separately for each electron, which are then summed as

$$G_0(q, Z) = 4\pi \sum_i \int_0^\infty \rho_i(r) \frac{\sin(qr)}{qr} \frac{m_ec^2}{E_i - V(r)} r^2 dr, \qquad (3.31)$$

where $\rho_i$ is the charge distribution of the $i$th electron, $E_i$ is the total energy of the $i$th electron, and $V(r)$ is the common central potential. The main improvement obtained with the modified form factor is that it predicts the differential cross section very well for small angles at high energies. This suggests that the modified form factor gives the correct high-energy behaviour of Rayleigh scattering at small angles [35].

Another problem in the presented form factor approach is that the resonances caused by the internal energy structure of the atom are neglected. When the energy of the incident photon equals to the difference between electron energy levels, or is above it, an absorption of the photon can also occur instead of scattering. To take the effects

of absorption into account, the form factor is modified by introducing the anomalous scattering factors $f'$ and $f''$ to the atomic form factor as [19]

$$F(q, Z) = F_0(q, Z) + f'(E_\mathrm{k}, Z) + i f''(E_\mathrm{k}, Z). \tag{3.32}$$

The term "anomalous" refers to the fact that the scattering cross section changes rapidly close to absorption energies. This can be seen in the atomic cross section for Rayleigh scattering in Fig. 3.4.

### 3.3.3  Comparison of Rayleigh scattering data

In order to decide a suitable theoretical model of Rayleigh scattering for the Monte Carlo method, we discuss some of the available data, and compile some results of comparisons of different models. Besides the form factor approximation, we discuss some results obtained by using the scattering matrix (S-matrix) method. However, the S-matrix method is not covered here in detail.

The most accurate model to describe Rayleigh scattering of photons is the S-matrix method, which describes scattering process in quantum electrodynamics [37]. The cross sections calculated with the S-matrix method have been shown to be in good agreement with experimental results [37–39]. Tabulations of the differential cross sections for photon energies 0.0543–2754.1 keV for $Z = 1$–100 have been published in RTAB database [40], which also includes the nuclear Thomson scattering. In a recent extensive evaluation [39], the RTAB cross sections were regarded as the state-of-the-art when compared with different form factor approximations. The downside in using the RTAB database is that it requires two-dimensional interpolation over energy and angle, which is computationally more intensive than one-dimensional interpolation of the form factors. The simulation of elastic scattering using the RTAB database is about a factor two slower than using models based on the form factor approximation [39]. However, the increase in the total simulation time is smaller because the cross section for Rayleigh scattering is usually less than 10% of the total microscopic cross section. To our knowledge, the cross sections calculated with the S-matrix method are not in use in general-purpose Monte Carlo codes.

Regarding different form factor tabulations, the best results have been obtained using the modified form factors with angle-independent anomalous scattering factors provided in the RTAB database [37, 39, 41]. However, these tabulations have not been exploited in general-purpose Monte Carlo codes. Instead, the most widely used form factors are the non-relativistic ones provided by the EPDL97, which are applied at least by MCNP [10], FLUKA [11, 12], and PENELOPE [7]. EPDL97 also provides anomalous scattering factors, but these are often ignored by assuming that the anomalous scattering becomes only important when the photoelectric effect dominates and the probability of Rayleigh scattering is small. Also, according to Ref. [39], including the anomalous scattering factors to the non-relativistic form factors given by the EPDL97 does not improve the agreement with experiments. Another interesting observation is that the relativistic form factors seem to be less

accurate than the non-relativistic ones [38, 39]. The reason for this is supposedly that the relativistic effects are substantially cancelled by other effects [35].

The atomic cross section for Rayleigh scattering can be calculated by numerically integrating the differential cross section over the scattering angle. In the form factor approximation, it is necessary to take into account the anomalous scattering factors to correctly estimate the atomic cross section below the K-shell binding energy. Therefore, the atomic cross sections given by the EPDL97 have been calculated using the anomalous scattering factors. According to Ref. [39], the atomic cross sections provided by the EPDL97 are compatible with the ones based on the S-matrix results of the RTAB database. Also, the atomic cross sections calculated using the modified form factors with anomalous scattering factors agree with the S-matrix results.

Based on the discussion above, the form factor approximation without the anomalous scattering factors was chosen to be implemented in Serpent 2. The chosen form factors were the non-relativistic ones provided by the EPDL97. The same combination is used in several Monte Carlo codes, and it should be sufficiently accurate for our photon transport model. Most importantly, because the atomic cross section for Rayleigh scattering is small in comparison to the other interactions, and the differential cross section is peaked in the forward direction, the form factor approximation shouldn't produce any significant error in comparison to more accurate models.

### 3.3.4  Sampling the photon direction

When Rayleigh scattering occurs, the only task is to calculate the direction of the scattered photon. Because in our model photons are considered unpolarized, the azimuthal scattering angle $\phi$ is sampled uniformly between 0 and $2\pi$. For sampling the cosine of the polar angle, $\mu$, we apply the commonly used rejection sampling method [42] using Eq. (3.23) as a PDF for $x^2$ by presenting it in a form

$$f(x^2) = C\psi(x^2)g(x^2),  \tag{3.33}$$

where

$$g(x^2) = \frac{|F(x, Z)|^2}{\int_0^{x^2_{\max}} |F(x, Z)|^2 \, dx^2},  \tag{3.34}$$

$$\psi(x^2) = \frac{1}{2}\left(1 + \left[\mu\left(x^2\right)\right]^2\right),  \tag{3.35}$$

and $C$ is a normalization constant. The variable $x$ defined in Eq. (3.30) obtains values from 0 to

$$x_{\max} = \frac{1}{\lambda} = \frac{E_k}{hc}.  \tag{3.36}$$

The variable $\mu$ can be solved from Eq. (3.30) as a function of $x^2$, which gives

$$\mu\left(x^2\right) = 1 - 2\frac{x^2}{x^2_{\max}}.  \tag{3.37}$$

The function $g(x^2)$ is the PDF of $x^2$ in the interval $[0, x_{\max}^2]$, and can be used for sampling the variable $x^2$. As it's easy to see, function $\psi(x^2)$ is confined in the interval $[1/2, 1]$, and can be therefore used as a rejection function, i.e. $x^2$ is accepted if

$$\xi \leq \psi(x^2), \tag{3.38}$$

where $\xi \sim unif(0, 1)$. The scattering cosine $\mu$ then follows from Eq. (3.37).

The recommended interpolation method for the EPDL97 form factors is linear interpolation on a log-log scale. Therefore, Eq. (2.38) is used for sampling the variable $x^2$ from the function $g(x^2)$ in an unnormalized form, i.e. $|F(x, Z)|^2$ is used as an unnormalized PDF and the integral denominator of $g(x^2)$ is taken account by multiplying the random variable $\xi$ in Eq. (2.38) by $\int_0^{x_{\max}^2} |F(x, Z)|^2 \, dx^2$. This integral is solved using Eq. (2.37).

## 3.4 Compton scattering

Compton scattering is an inelastic scattering process of a photon in which its direction and energy are changed. The residual energy is given to a single electron which is ejected from the atom, creating a vacancy in the electron shell. The atomic cross section for Compton scattering is approximately proportional to $Z$ above the highest binding energy. Compton scattering dominates in a wide energy range for low-$Z$ elements, from a few keV up to tens of MeV. As $Z$ increases, the dominant energy range becomes narrower due to the stronger $Z$-dependences of the photoelectric effect and pair production. Nevertheless, Compton scattering is the main scattering interaction for all the elements at most energies, except at low energies where Rayleigh scattering is the dominant scattering process. It also has an important role in the creation of recoil electrons and vacancies which lead into secondary bremsstrahlung and fluorescence radiation. Therefore, a special attention is given to Compton scattering in this thesis in order to model this interaction accurately.

We first discuss the simple scattering process from a free stationary electron. More sophisticated models are then represented and compared, namely the incoherent scattering function approach and the relativistic impulse approximation, which are more suitable for describing the scattering process from atomic electrons. The relatively unimportant Raman–Compton resonances and infrared divergence, which are not included in these approximations, are discussed only in brief. Different methods for modelling the angular distribution of Compton electrons are also examined. Finally, a detailed algorithm for simulating a Compton scattering event is presented.

### 3.4.1 Scattering from a free electron

When the electron is free and stationary, one-to-one relation exists between the scattering angle $\theta$ and the energy $E'_{\mathrm{k}}$ of the scattered photon. This relation can be

solved using the conservation of energy and momentum

$$E_k + E_e = E'_k + E'_e, \tag{3.39}$$

$$\hbar\mathbf{k} + \mathbf{p}_e = \mathbf{p}'_e + \hbar\mathbf{k}', \tag{3.40}$$

where $E_e$ and $E'_e$ are the total energy of the electron before and after the interaction, respectively, and $\mathbf{p}_e$ and $\mathbf{p}'_e$ are the corresponding momenta. For a free stationary electron, $E_e = m_e c^2$ and $\mathbf{p}_e = 0$. The momentum $\mathbf{p}'_e$ can be solved from Eq. (3.40) as

$$p'^2_e = \hbar^2(k^2 + k'^2 - 2kk'\cos\theta). \tag{3.41}$$

Inserting $\mathbf{p}'_e$ and $E'_e$ from Eq. (3.39) into the relativistic electron energy equation

$$E'^2_e = p'^2_e c^2 + m_e^2 c^4 \tag{3.42}$$

gives the relation between the energy of the scattered photon and the scattering angle:

$$E'_k = \frac{E_k}{1 + E_k/m_e c^2(1 - \cos\theta)} \equiv E_C. \tag{3.43}$$

From this equation it can be seen that the maximum and minimum scattered photon energies are obtained at the scattering angles of 0° and 180°, respectively.

The differential cross section for Compton scattering from a free stationary electron is given by the Klein–Nishina cross section [43]

$$\left(\frac{d\sigma_{Co}}{d\Omega}\right)_{KN} = \frac{r_e^2}{2}\left(\frac{E'_k}{E_k}\right)^2\left(\frac{E'_k}{E_k} + \frac{E_k}{E'_k} - \sin^2\theta\right). \tag{3.44}$$

The cross section differential in $E'_k$ can be obtained using the chain rule as

$$\left(\frac{d\sigma_{Co}}{dE'_k}\right)_{KN} = \left(\frac{d\sigma_{Co}}{d\Omega}\right)_{KN}\left(\frac{dE_C}{d\Omega}\right)^{-1} = 2\pi\left(\frac{d\sigma_{Co}}{d\Omega}\right)_{KN}\left(\frac{dE_C}{d\cos\theta}\right)^{-1}$$

$$= 2\pi\frac{m_e c^2}{E_C^2}\left(\frac{d\sigma_{Co}}{d\Omega}\right)_{KN}, \tag{3.45}$$

where $dE_C/d\cos\theta$ is obtained from Eq. (3.43). The Klein–Nishina differential cross section describes the scattering process from atomic electrons reasonably well above a few MeV when the electrons are essentially free with respect to the photon. However, at lower energies the Klein–Nishina equation is not adequate because the electron binding and the momentum of atomic electrons have a large impact on the cross section. These effects are discussed in the next sections, after which the angular and energy distributions of the Klein–Nishina equation are compared with more accurate models in Sec. 3.4.5.
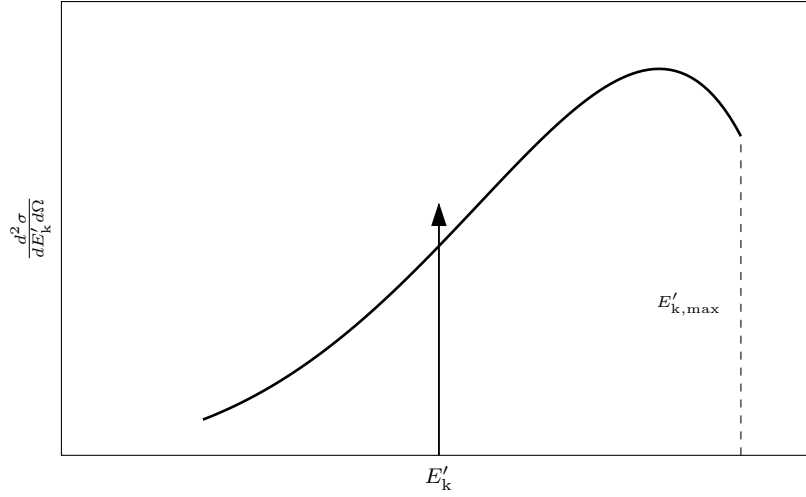
Figure 3.11: Schematic of the binding effects on the double differential cross section for Compton scattering at a fixed angle. The arrow presents the free electron value of the cross section.

### 3.4.2 Scattering from atomic electrons

The scattering from a bound atomic electron differs greatly from the free electron scattering. The binding effects on the double differential cross section at a fixed angle are illustrated in Fig. 3.11. The most apparent effect is the so-called Doppler broadening of the spectrum of the scattered photon, which is caused by the momentum distribution of the atomic electron. Instead of a delta function corresponding to Eq. (3.43), a wider distribution of the scattered energy is observed at fixed angle. The broadening increases with the binding energy of the electron, because the momentum distribution is wider for tighter bound electrons [44]. Thus, the Compton scattering spectrum is wider for inner-shell electrons. When considering the scattering spectrum from the whole atom at a certain angle, outer-shell electrons cause a peak in the spectrum while inner-shells form the tails of the distribution.

The electron binding also causes the peak of the Doppler-broadened cross section to be shifted from the free electron value. This shift is known as the Compton defect, and its magnitude and direction depend on the shell [44]. Binding also introduces a kinematic limit to the scattered photon energy. It is clear that Compton scattering is possible only when the binding energy of the electron is smaller than the photon energy. This also limits the maximum scattered photon energy to

$$E'_{k,max} = E_k - E_{b,i}. \tag{3.46}$$

In the free electron scattering, the maximum energy of the scattered photon is obtained in the forward direction which is seen from Eq. (3.43). However, the kinematic limit forbids the high scattering energies, and therefore Compton scattering from atomic electrons is suppressed in the forward direction, especially at lower incident photon energies [44].

In order to describe the scattering from bound electrons, a DDCS (differential with respect to the scattered photon energy and angle) or a triply differential cross section (differential also with respect to the electron direction) must be used. The state-of-the-art theoretical models for Compton scattering are based on the S-matrix method [45, 46], but the corresponding differential cross section must be calculated numerically. The S-matrix treatment is also limited to incident photon energies below about 1 MeV [47]. Therefore, the S-matrix approach hasn't been applied in Monte Carlo photon transport calculations. Instead, much simpler but still relatively accurate models are being used. Next, we first discuss an approach called the incoherent scattering function approximation which has been derived for describing the angular distribution of photons scattering from atomic electrons. This method takes into account the electron binding to some extent, but ignores the Doppler broadening of the cross section. Then, we present the relativistic impulse approximation which quite accurately describes the Doppler broadening of the spectrum.

### 3.4.3 Incoherent scattering function approximation

In the incoherent scattering function approximation (ISF), the atomic differential cross section is obtained by multiplying the Klein–Nishina DCS (3.44) by the incoherent scattering function, $S(E_k, \theta, Z)$, which gives the DCS

$$\left(\frac{d\sigma_{Co}}{d\Omega}\right)_S = \left(\frac{d\sigma_{Co}}{d\Omega}\right)_{KN} S(E_k, \theta, Z). \tag{3.47}$$

This form of an expression actually arises from the Born approximation [33], being similar to the form factor approximation of Rayleigh scattering discussed in Sec. 3.3.1. The incoherent scattering function can be interpreted as a measure of the number of atomic electrons behaving as free electrons. Therefore, $S$ can be expected to be close to $Z$ when the photon energy is high compared with the highest electron binding energy, whereas for low photon energies it should approach zero.

The incoherent scattering function can be expressed using a generalized form factor

$$F_\epsilon(\mathbf{q}, Z) = \left\langle \Psi_\epsilon \left| \sum_{j=1}^{Z} e^{i\mathbf{q}\cdot\mathbf{r}_j} \right| \Psi_0 \right\rangle, \tag{3.48}$$

where the variable $\epsilon$ indicates the energy of an excited or ionized state $\Psi_\epsilon$, $\mathbf{r}_j$ is the vector distance of the $j$th electron from the nucleus, $\Psi_0$ is the ground state of the atom, and the momentum transfer vector $\hbar\mathbf{q}$ is defined in Eq. (3.24). The magnitude of $\mathbf{q}$ is now given by

$$q = \frac{1}{c\hbar}\sqrt{E_k^2 + E_k'^2 - 2E_k E_k' \cos\theta}. \tag{3.49}$$

Using the variable $\mathbf{q}$ instead of $E_k$ and $\theta$, the incoherent scattering function is defined as

$$S(\mathbf{q}, Z) = \sum_{\epsilon>0} |F_\epsilon(\mathbf{q}, Z)|^2, \tag{3.50}$$

in which the sum means a sum over the discrete states, excluding the ground state, and an integral over the continuum states [34]. Including the ground state to the sum and then subtracting it yields

$$S(\mathbf{q}, Z) = \sum_{\epsilon=0} \left\langle \Psi_0 \left| \sum_{n=1}^{Z} e^{-i\mathbf{q}\cdot\mathbf{r}_n} \right| \Psi_\epsilon \right\rangle \left\langle \Psi_\epsilon \left| \sum_{m=1}^{Z} e^{i\mathbf{q}\cdot\mathbf{r}_m} \right| \Psi_0 \right\rangle$$
$$- \left| \left\langle \Psi_0 \left| \sum_{j=1}^{Z} e^{i\mathbf{q}\cdot\mathbf{r}_j} \right| \Psi_0 \right\rangle \right|^2. \tag{3.51}$$

Identifying the last term as a squared form factor in Eq. (3.25) and using the identity

$$\sum_{\epsilon=0} |\Psi_\epsilon\rangle \langle \Psi_\epsilon| = 1, \tag{3.52}$$

the incoherent scattering function can be expressed using only ground state wave functions as

$$S(\mathbf{q}, Z) = \sum_{m=1}^{Z} \sum_{n=1}^{Z} \left\langle \Psi_0 \left| e^{i\mathbf{q}\cdot(\mathbf{r}_m - \mathbf{r}_n)} \right| \Psi_0 \right\rangle - |F(\mathbf{q}, Z)|^2. \tag{3.53}$$

Different theories of calculating the incoherent scattering function have been developed [48], of which the most successful and commonly used is the Waller–Hartree theory (WH) [49]. This theory assumes that the electrons behave independently of each other, meaning that an ionization or excitation of an electron leaves the other electrons undisturbed. It is also assumed that the scattered photon energy is equal to the incident one, and the energy conservation is ignored when summing the final states. The incoherent scattering function then reduces to [49, 50]

$$S_{\mathrm{WH}}(q, Z) = Z - \sum_{j=1}^{Z} |f_{jj}(q)|^2 - \sum_{j=1}^{Z} \sum_{i\neq j}^{Z} |f_{ji}(q)|^2, \tag{3.54}$$

where the form factor $f_{ji}$ is given for one-electron wave functions $\psi_j$ and $\psi_i$ by

$$f_{ji}(q) = \left\langle \psi_j \left| e^{i\mathbf{q}\cdot\mathbf{r}} \right| \psi_i \right\rangle. \tag{3.55}$$

Because the approximation $E_{\mathrm{k}} = E'_{\mathrm{k}}$ is made, $q$ reduces to the one defined in Eq. (3.29). To avoid confusion with the definition (3.49), $S_{\mathrm{WH}}$ is from now on given as a function of the variable $x$ defined in Eq. (3.30).

A comprehensive compilation of Waller–Hartree incoherent scattering function results have been tabulated by Hubbel et al. [34]. These are the most commonly used incoherent scattering functions, e.g., they are included in the EPDL97 [20]. In Fig. 3.12, $S_{\mathrm{WH}}$ given by the EPDL97 is plotted for hydrogen, carbon, iron, and uranium. At low values of $x$, i.e. when the photon energy or the scattering angle is small, $S_{\mathrm{WH}}$ becomes very small, meaning that the DCS is suppressed at low energies and in the forward direction. At high values of $x$, $S_{\mathrm{WH}}$ approaches $Z$ and hence
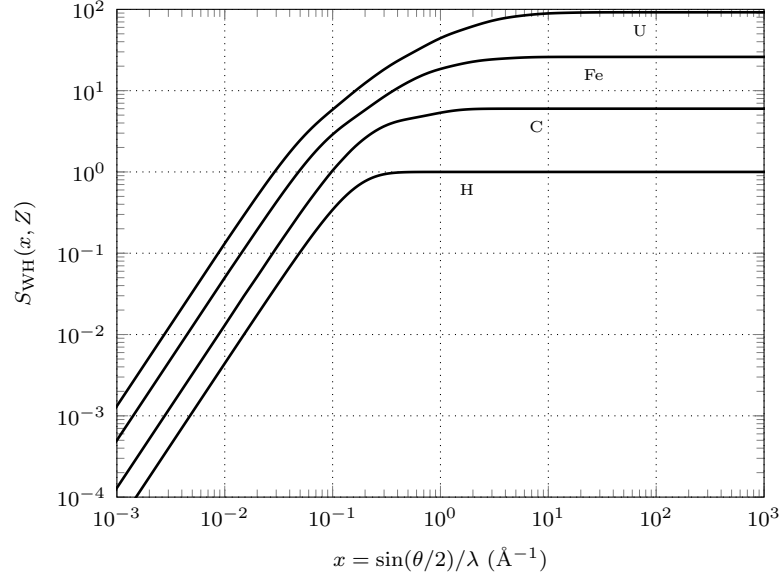
Figure 3.12: Waller–Hartree incoherent scattering function as a function of the momentum transfer variable $x$ for hydrogen, carbon, iron, and uranium. The data is from the EPDL97 [20].

the atomic DCS becomes the Klein–Nishina cross section multiplied by $Z$. The value of $S_{\mathrm{WH}}$ approaches $Z$ slower for heavy elements which is due to the higher binding energies of the inner-shell electrons. The angular and energy distributions of scattered photons according to the ISF approximation are presented in Sec. 3.4.5.

To summarize this section, the angular DCS for Compton scattering with the Waller–Hartree incoherent scattering function is denoted by

$$\left(\frac{d\sigma_{\mathrm{Co}}}{d\Omega}\right)_{\mathrm{ISF}} = \left(\frac{d\sigma_{\mathrm{Co}}}{d\Omega}\right)_{\mathrm{KN}} S_{\mathrm{WH}}\left(x, Z\right). \tag{3.56}$$

The cross section differential in the scattered photon energy is obtained in the same way as Eq. (3.45), and is expressed as

$$\left(\frac{d\sigma_{\mathrm{Co}}}{dE_{\mathrm{k}}'}\right)_{\mathrm{ISF}} = 2\pi \frac{m_{\mathrm{e}}c^2}{E_{\mathrm{C}}^2} \left(\frac{d\sigma_{\mathrm{Co}}}{d\Omega}\right)_{\mathrm{KN}} S_{\mathrm{WH}}\left(x, Z\right). \tag{3.57}$$

### 3.4.4   Relativistic impulse approximation

In the impulse approximation (IA), the scattering from an atomic electron is treated as a scattering from a free electron with a momentum distribution determined by its wave function. In other words, the electron binding is not explicitly taken into account and only the momentum distribution of the electron is considered. This approximation can be justified by the impulsive nature of the Compton scattering process. Because the time period of the interaction is short, and the atomic relaxation

occurs only after the Compton electron has escaped from the atom, the potential seen by the electron is the same immediately before and after the interaction [51]. Therefore, the photon seems to interact only with a single free electron which appears to have a certain momentum distribution, while the other electrons essentially act as spectators during the interaction. The IA is valid when the energy transfer to the Compton electron is much larger than its binding energy [51]. This condition is often fulfilled when considering the average scattering from the whole atom, because outer shells have more electrons and lower binding energies than inner shells, and the interaction probability of a shell is approximately proportional to the electron number. Also, Compton scattering is the main interaction at energies much higher than the K-shell binding energy for every element, and the photoelectric effect dominates when the IA is not valid.

A commonly used IA model is the relativistic impulse approximation (RIA) developed by Ribberfors [52], which is based on relativistic treatment of two colliding monoenergetic beams of photons and electrons. An approximate DDCS for an electron in the $i$th shell is given by [52,53]

$$\left(\frac{d^2\sigma_{\mathrm{Co}}}{dE'_{\mathrm{k}}d\Omega}\right)_{\mathrm{RIA},i} = \frac{r_{\mathrm{e}}^2}{2}\frac{E'_{\mathrm{k}}m_{\mathrm{e}}c}{E_{\mathrm{k}}c\hbar q}\left[1+\left(\frac{p_z}{m_{\mathrm{e}}c}\right)^2\right]^{-1/2}X(R,R')J_i\left(p_z\right), \qquad (3.58)$$

where the function $X(R,R')$ and its variables $R$ and $R'$ are defined as

$$X(R,R') = \frac{R}{R'} + \frac{R'}{R} + 2\left(\frac{1}{R} - \frac{1}{R'}\right) + \left(\frac{1}{R} - \frac{1}{R'}\right)^2, \qquad (3.59)$$

$$R = \frac{E_{\mathrm{k}}}{m_{\mathrm{e}}c^2}\left\{\left[1+\left(\frac{p_z}{m_{\mathrm{e}}c}\right)^2\right]^{1/2} + \frac{E_{\mathrm{k}} - E'_{\mathrm{k}}\cos\theta}{c\hbar q}\frac{p_z}{m_{\mathrm{e}}c}\right\}, \qquad (3.60)$$

$$R' = R - \frac{E_{\mathrm{k}}E'_{\mathrm{k}}}{m_{\mathrm{e}}^2c^4}\left(1 - \cos\theta\right). \qquad (3.61)$$

The magnitude of the momentum transfer vector $\hbar\mathbf{q}$ is given by Eq. (3.49). The variable $p_z$ is the projection of the initial electron momentum on the direction of the vector $-\mathbf{q}$, i.e.

$$p_z = -\frac{\mathbf{p}_{\mathrm{e}}\cdot\mathbf{q}}{q}. \qquad (3.62)$$

This variable can be written as a function of photon energy and scattering angle by applying the conservation of energy and momentum

$$E_{\mathrm{k}} + E_{\mathrm{e}} = E'_{\mathrm{k}} + E'_{\mathrm{e}} + E_{\mathrm{b},i}, \qquad (3.63)$$

$$\hbar\mathbf{k} + \mathbf{p}_{\mathrm{e}} = \hbar\mathbf{k}' + \mathbf{p}'_{\mathrm{e}}, \qquad (3.64)$$

where the notation $E_{\mathrm{b},i} > 0$ is used. Using Eq. (3.64) and its square

$$\hbar^2\left(k^2 + k'^2 - 2kk'^2\cos\theta\right) = p_{\mathrm{e}}^2 + p_{\mathrm{e}}'^2 - 2\mathbf{p}_{\mathrm{e}}\cdot\mathbf{p}'_{\mathrm{e}}, \qquad (3.65)$$

together with the energy equations

$$E_e^2 = p_e^2 c^2 + m_e^2 c^4, \tag{3.66}$$
$$E_e'^2 = p_e'^2 c^2 + m_e^2 c^4, \tag{3.67}$$

we can write Eq. (3.62) as

$$p_z = \frac{1}{\hbar q}\left(p_e^2 - \mathbf{p}_e \cdot \mathbf{p}_e'\right) = \frac{1}{2c^2 \hbar q}\left(E_k^2 + E_k'^2 - 2E_k E_k' \cos\theta + E_e^2 - E_e'^2\right). \tag{3.68}$$

Solving $E_e'^2$ from Eq. (3.63), we obtain

$$p_z = \frac{E_k E_k'(1 - \cos\theta) + (E_k - E_k')(E_{b,i} - E_e) + E_{b,i}E_e - \frac{1}{2}E_{b,i}^2}{c^2 \hbar q}. \tag{3.69}$$

Because in the IA it is assumed that the scattering occurs with free electrons, we set $E_{b,i} = 0$. Since the kinetic energy of an atomic electron is small in comparison to $m_e c^2$, we can set $E_e = m_e c^2$, which gives us the final form to be used in Eq. (3.58):

$$p_z = \frac{E_k E_k'(1 - \cos\theta) - m_e c^2(E_k - E_k')}{c^2 \hbar q}. \tag{3.70}$$

This can also be written in the form

$$\frac{p_z}{m_e c} = \frac{E_k(E_k' - E_C)}{E_C c \hbar q} \equiv \tilde{p}_z, \tag{3.71}$$

from which can be seen that the free electron scattering energy $E_k' = E_C$ corresponds to $p_z = 0$. The minimum and maximum values of $p_z$ are obtained at $E_k' = 0$ and $E_k' = E_k - E_{b,i}$, respectively, giving

$$p_{z,\min} = -m_e c, \tag{3.72}$$
$$p_{z,\max_i} = \frac{E_k(E_k - E_{b,i})(1 - \cos\theta) - m_e c^2 E_{b,i}}{c\sqrt{2E_k(E_k - E_{b,i})(1 - \cos\theta) + E_{b,i}^2}}. \tag{3.73}$$

The maximum value of $p_z$ therefore depends on the electron shell, and can also be negative. The variable $p_z$ is often expressed in the units of $\alpha m_e c$ where $\alpha \approx 1/137$ is the fine-structure constant.

The only shell-dependent part of Eq. (3.58), excluding the kinematic limit, is the so-called Compton profile $J_i(p_z)$ which accounts for the Doppler broadening of the DDCS. It is defined as

$$J_i(p_z) = \iint \rho_i(\mathbf{p}_e) dp_x dp_y, \tag{3.74}$$

where $\rho_i(\mathbf{p}_e) = |\psi(\mathbf{p}_e)|^2$ is the initial electron momentum distribution and $\psi(\mathbf{p}_e)$ is the electron wave function. Due to wave function normalization, Compton profiles are normalized to unity as

$$\int_{-\infty}^{\infty} J_i(p_z) dp_z = 1. \tag{3.75}$$
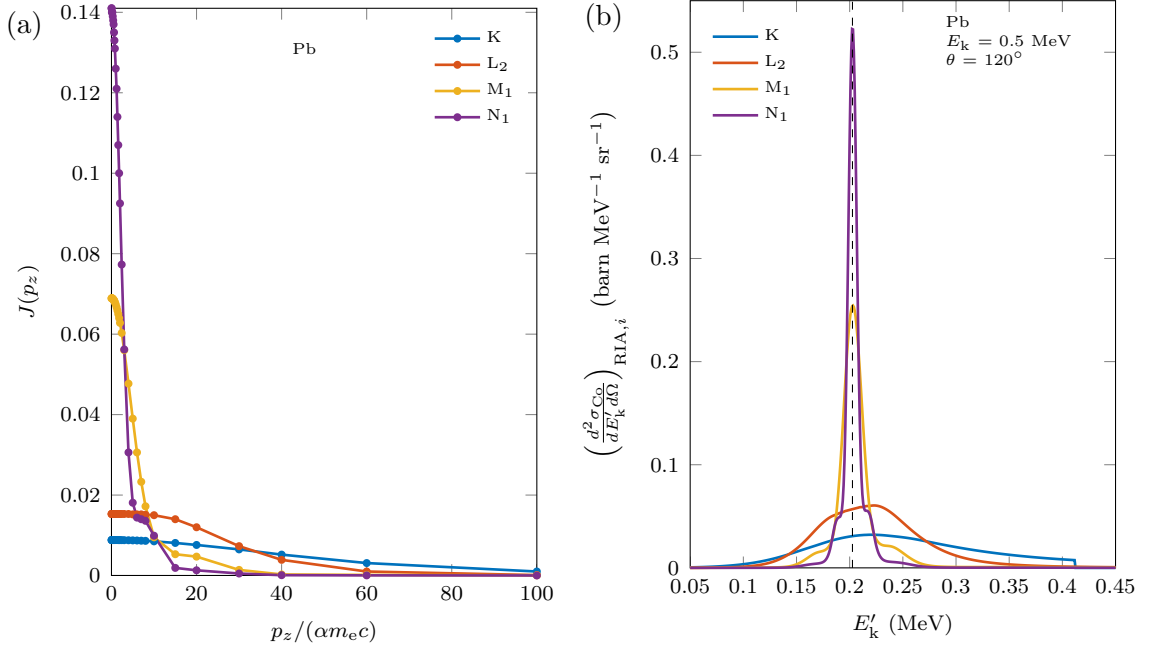
Figure 3.13: (a) Hartree–Fock Compton profiles for K-, $L_2$-, $M_1$-, and $N_1$-shell electrons of lead [54], and (b) the corresponding DDCSs according to Eq. (3.58) for the scattering of 0.5 MeV photons into 120°. The dashed black line in (b) presents the free electron scattering energy $E_C$ given by Eq. (3.43).

The most extensive and commonly used Compton profiles are the Hartree–Fock Compton profiles calculated by Biggs et al. [54]. In the Hartree–Fock approximation, the electron momentum distribution is isotropic, and the Compton profile reduces to [51]

$$J_i(p_z) = 2\pi \int_{|p_z|}^{\infty} p\rho_i(p)dp. \tag{3.76}$$

The Compton profile can be interpreted as a probability density function of $p_z$. In the case of Hartree–Fock Compton profiles, $J_i(p_z)$ is symmetric about $p_z = 0$ for all the shells of every element. Also, the maximum of $J_i(p_z)$ is obtained at $p_z = 0$ for all the shells. Examples of Hartree–Fock Compton profiles for four shells of lead are illustrated in Fig. 3.13a. In general, $J_i(p_z)$ is broader for inner shells and becomes highly peaked at $p_z = 0$ as the shell number increases. The effect of the Compton profile on the DDCS (3.58) can be seen in Fig. 3.13b, which presents the DDCSs for the same shells as in 3.13a. Much like the Compton profiles, the DDCS is broad for inner shells, whereas for outer shells the DDCS is narrowly peaked at $E_C$ corresponding to $p_z = 0$. When considering the atomic DDCS, the most probable scattered photon energy is usually equal to $E_C$.

The kinematic limit stated by Eq. (3.46) can be taken into account by Heaviside step function

$$H(v_i) = \begin{cases} 0, & v_i < 0 \\ 1, & v_i \geq 0 \end{cases}, \tag{3.77}$$

where $v_i = E_\mathrm{k} - E'_\mathrm{k} - E_{\mathrm{b},i}$. The atomic DDCS is obtained by multiplying Eq. (3.58) by the number of electrons per shell $f_i$ and $H(v_i)$, and then summing over all shells:

$$\left(\frac{d^2\sigma_\mathrm{Co}}{dE'_\mathrm{k}d\Omega}\right)_\mathrm{RIA,a} = \frac{r_\mathrm{e}^2}{2}\frac{E'_\mathrm{k}m_\mathrm{e}c}{E_\mathrm{k}c\hbar q}\left(1 + \tilde{p}_z^2\right)^{-1/2} X(R,R') \sum_i f_i H(v_i) J_i\left(p_z\right). \qquad (3.78)$$

This equation is difficult to use as such, and therefore different approximations have been presented in order to efficiently sample the scattered photon energy [55, 56]. Here, we follow the approximation presented in Ref. [55]. First, Eq. (3.78) is written in the form

$$\left(\frac{d^2\sigma_\mathrm{Co}}{dE'_\mathrm{k}d\Omega}\right)_\mathrm{RIA,a} = \frac{r_\mathrm{e}^2}{2}\frac{E'_\mathrm{k}}{E_\mathrm{k}}\left(\frac{E_\mathrm{k}}{E_\mathrm{C}} + \frac{E_\mathrm{k}\cos\theta - E'_\mathrm{k}}{c\hbar q}\tilde{p}_z\right)^{-1}\left(1 + \tilde{p}_z^2\right)^{-1/2}$$
$$\times X(R,R')\left(\sum_i f_i H(v_i) J_i\left(p_z\right)\right)\frac{dp_z}{dE'_\mathrm{k}}, \qquad (3.79)$$

where

$$\frac{dp_z}{dE'_\mathrm{k}} = \frac{m_\mathrm{e}c}{c\hbar q}\left(\frac{E_\mathrm{k}}{E_\mathrm{C}} + \frac{E_\mathrm{k}\cos\theta - E'_\mathrm{k}}{c\hbar q}\tilde{p}_z\right). \qquad (3.80)$$

This equation can be approximated using the fact that the most probable values of $p_z$ are close to zero corresponding to $E'_\mathrm{k} \approx E_\mathrm{C}$, except for the inner shells of heavy elements. The first approximation is to set $p_z = 0$ and $E'_\mathrm{k} = E_\mathrm{C}$ for $X(R,R')$ which mostly accounts for relativistic effects [53]. The variable $X(R,R')$ then reduces to the Klein–Nishina type of expression [53]

$$X_\mathrm{KN}(\theta) = \frac{E_\mathrm{C}}{E_\mathrm{k}} + \frac{E_\mathrm{k}}{E_\mathrm{C}} - \sin^2\theta, \qquad (3.81)$$

which is a function of only the scattering angle. The remaining factor in Eq. (3.79) to be approximated is

$$F\left(E'_\mathrm{k}\right) = \frac{E'_\mathrm{k}}{E_\mathrm{k}}\left(\frac{E_\mathrm{k}}{E_\mathrm{C}} + \frac{E_\mathrm{k}\cos\theta - E'_\mathrm{k}}{c\hbar q}\tilde{p}_z\right)^{-1}\left(1 + \tilde{p}_z^2\right)^{-1/2}. \qquad (3.82)$$

The simplest approximation for $F$ is to set $p_z = 0$ which gives $F \approx E'_\mathrm{k}E_\mathrm{C}/E_\mathrm{k}^2$. Another presented approximation is to use the first term of the Taylor expansion of $F$ [56]. However, this approximation would somewhat complicate the sampling procedure. For the sake of simplicity, Eq. (3.79) is approximated as

$$\left(\frac{d^2\sigma_\mathrm{Co}}{dE'_\mathrm{k}d\Omega}\right)_\mathrm{RIA,a} \approx \frac{r_\mathrm{e}^2}{2}\frac{E'_\mathrm{k}E_\mathrm{C}}{E_\mathrm{k}^2}X_\mathrm{KN}(\theta)\left(\sum_i f_i H(v_i) J_i\left(p_z\right)\right)\frac{dp_z}{dE'_\mathrm{k}}. \qquad (3.83)$$

The atomic DDCS can now be expressed differential in $p_z$ using the chain rule

$$\left(\frac{d^2\sigma_\mathrm{Co}}{dp_z d\Omega}\right)_\mathrm{RIA,a} = \left(\frac{d^2\sigma_\mathrm{Co}}{dE'_\mathrm{k}d\Omega}\right)_\mathrm{RIA,a}\left(\frac{dp_z}{dE'_\mathrm{k}}\right)^{-1}$$
$$\approx \frac{r_\mathrm{e}^2}{2}\frac{E'_\mathrm{k}E_\mathrm{C}}{E_\mathrm{k}^2}X_\mathrm{KN}(\theta)\sum_i f_i H(v_i) J_i\left(p_z\right). \qquad (3.84)$$

For this form, the scattered photon energy $E'_\mathrm{k}$ can be solved from Eq. (3.71), giving

$$E'_\mathrm{k} = \frac{E_\mathrm{k}}{\tilde{p}_z^2 - \nu^2} \left( \tilde{p}_z^2 \cos\theta - \nu - \tilde{p}_z \sqrt{1 - \tilde{p}_z^2 \sin^2\theta + \nu\left(\nu - 2\cos\theta\right)} \right), \qquad (3.85)$$

where $\nu = E_\mathrm{k}/E_\mathrm{C}$.

The exact atomic RIA cross section differential in the scattered photon energy must be calculated numerically from the integral

$$\left( \frac{d\sigma_\mathrm{Co}}{dE'_\mathrm{k}} \right)_\mathrm{RIA,a} = \int \left( \frac{d^2\sigma_\mathrm{Co}}{dE'_\mathrm{k}\,d\Omega} \right)_\mathrm{RIA,a} d\Omega. \qquad (3.86)$$

The atomic RIA cross section differential in the solid angle must also be calculated numerically by integrating Eq. (3.78) over $E'_\mathrm{k}$, or approximately by integrating Eq. (3.84) over $p_z$. In order to enable straightforward integration, the remaining $E'_\mathrm{k}$ in Eq. (3.84) is also approximated as $E'_\mathrm{k} \approx E_\mathrm{C}$. The DCS then becomes

$$\left( \frac{d\sigma_\mathrm{Co}}{d\Omega} \right)_\mathrm{RIA,a} \approx \frac{r_\mathrm{e}^2}{2} \left( \frac{E_\mathrm{C}}{E_\mathrm{k}} \right)^2 X_\mathrm{KN}(\theta) \sum_i f_i H(E_\mathrm{k} - E_{\mathrm{b},i}) \int_{p_{z,\mathrm{min}}}^{p_{z,\mathrm{max}_i}} J_i\left(p_z\right) dp_z$$

$$= \left( \frac{d\sigma_\mathrm{Co}}{d\Omega} \right)_\mathrm{KN} S_\mathrm{IA}\left(E_\mathrm{k},\theta\right), \qquad (3.87)$$

where the function

$$S_\mathrm{IA}\left(E_\mathrm{k},\theta\right) = \sum_i f_i H(E_\mathrm{k} - E_{\mathrm{b},i}) \int_{p_{z,\mathrm{min}}}^{p_{z,\mathrm{max}_i}} J_i\left(p_z\right) dp_z \qquad (3.88)$$

is called the incoherent scattering function in the IA. Therefore, the DCS is approximately given by the Klein–Nishina cross section multiplied by $S_\mathrm{IA}$ which is the incoherent scattering function approximation discussed in Sec. 3.4.3. Unfortunately, $S_\mathrm{IA}$ cannot be expressed simply as a function of $x$ like $S_\mathrm{WH}$, and tabulation of $S_\mathrm{IA}$ as a function of both $E_\mathrm{k}$ and $\theta$ would be impractical. Naturally, the incoherent scattering function in the RIA can also be calculated exactly as

$$S_\mathrm{IA}\left(E_\mathrm{k},\theta\right) = \frac{\int_0^{E_\mathrm{k}} \left( \dfrac{d^2\sigma_\mathrm{Co}}{dE'_\mathrm{k}\,d\Omega} \right)_\mathrm{RIA,a} dE'_\mathrm{k}}{\left( \dfrac{d\sigma_\mathrm{Co}}{d\Omega} \right)_\mathrm{KN}}. \qquad (3.89)$$

### 3.4.5   Energy and angular distribution of scattered photons

Now that different theoretical models for describing Compton scattering have been presented, we can compare their energy and angular differential cross sections and atomic cross sections. The validity of the free electron model and the ISF approximation are studied graphically in comparison to the exact RIA. Also, the approximated RIA equations presented in the previous section are discussed.
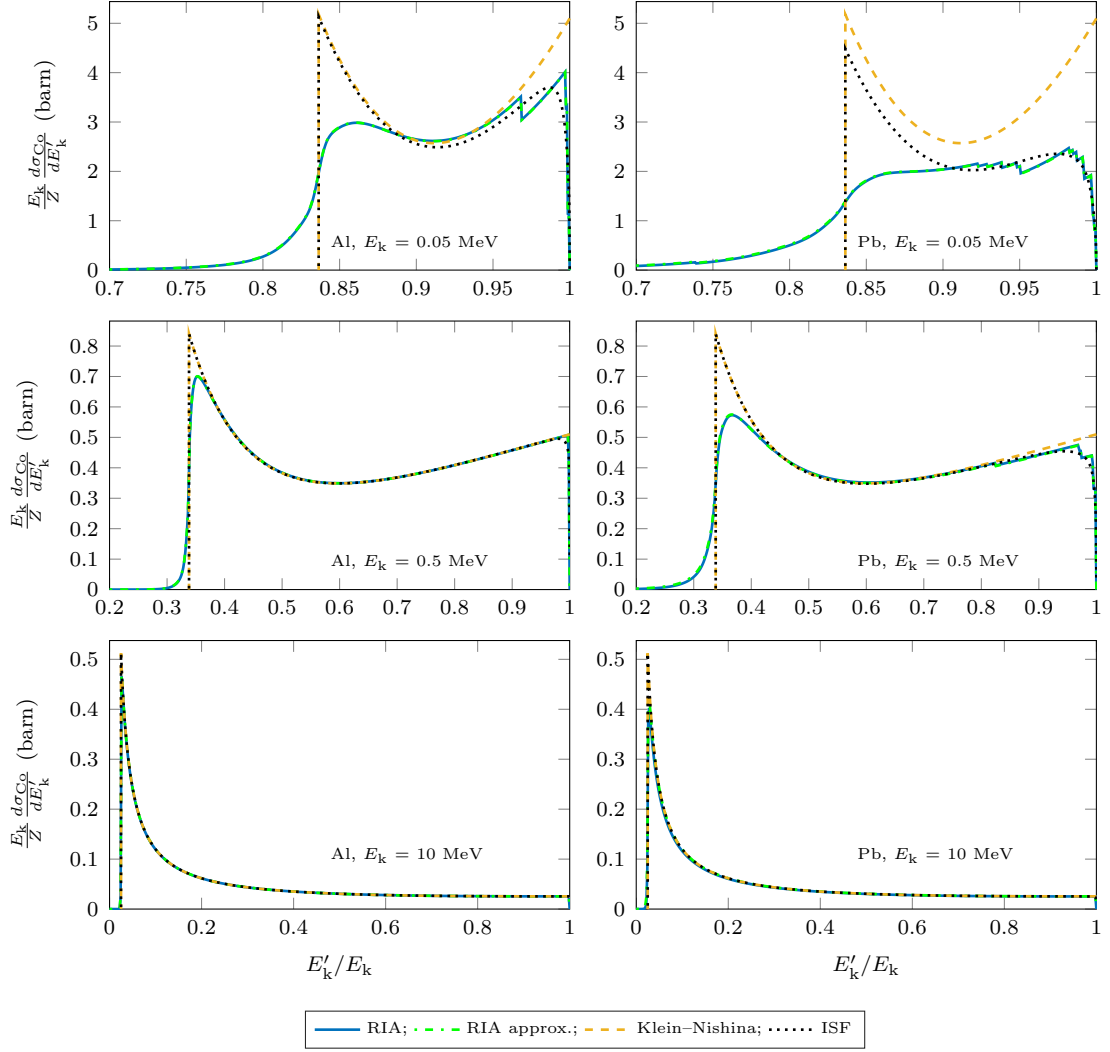
Figure 3.14: Compton cross section differential with respect to the scattered photon energy for aluminium and lead according to the RIA, Eq. (3.86); the RIA approximation integrated from Eq. (3.83); the Klein–Nishina theory, Eq. (3.45); and the ISF approximation, Eq. (3.57).

The energy DCSs according to the RIA, the RIA approximation given by Eq. (3.83), the free electron model, and the ISF approximation are shown in Fig. 3.14 for aluminium and lead at incident photon energies of 0.05, 0.5, and 10 MeV. A common property of the compared energy DCSs is that at small incident photon energies, $E'_k/E_k$ is distributed close to unity, and the distribution broadens as the energy increases. There are major differences between the compared models especially at low energies. The most striking difference is the Doppler broadening of the RIA DCS at 0.05 MeV, which is more significant for lead at this energy. The RIA energy spectrum is not confined by the minimum energy of the free electron theory, and the backscattering and forward scattering peaks are much smaller. Another difference is the discontinuities seen at the high end of the RIA spectrum, which are due to the kinematic limit set by Eq. (3.46) for each shell. The ISF DCS resembles the
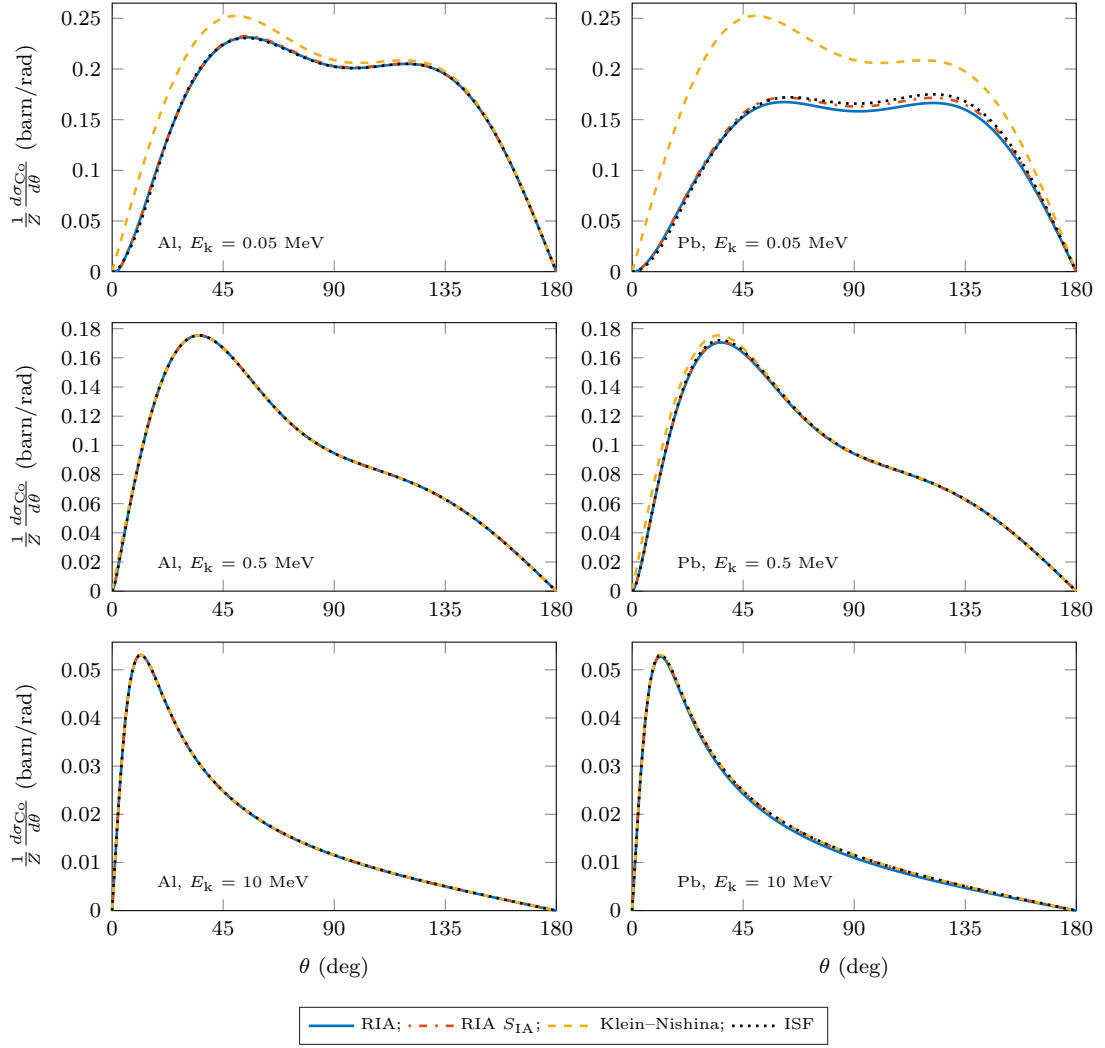
Figure 3.15: Compton cross section differential with respect to the photon scattering angle for aluminium and lead according to the numerically integrated RIA, Eq. (3.78); RIA $S_{IA}$, Eq. (3.87); Klein–Nishina theory, Eq. (3.44); and the ISF approximation, Eq. (3.56).

RIA DCS at the high end of the spectrum because the incoherent scattering factor suppresses the DCS in the forward direction. The RIA and the ISF DCSs begin to resemble the Klein–Nishina DCS as the incident photon energy increases. However, the RIA DCS differs slightly from the Klein–Nishina DCS at the low end of the spectrum even at 10 MeV, the difference being greater for lead than aluminium. In this graphical comparison, the approximate DCS calculated from Eq. (3.83) seems to be very accurate in all the tested cases.

The angular distribution of scattered photons given by the RIA, the RIA $S_{IA}$ (Eq. (3.87)), the free electron model, and the ISF approximation are compared in Fig. 3.15 for aluminium and lead at incident photon energies of 0.05, 0.5 and 10 MeV. At 0.05 MeV, the Klein–Nishina DCS deviates greatly from the other distributions. The difference is greater for lead, which is due to its higher electron
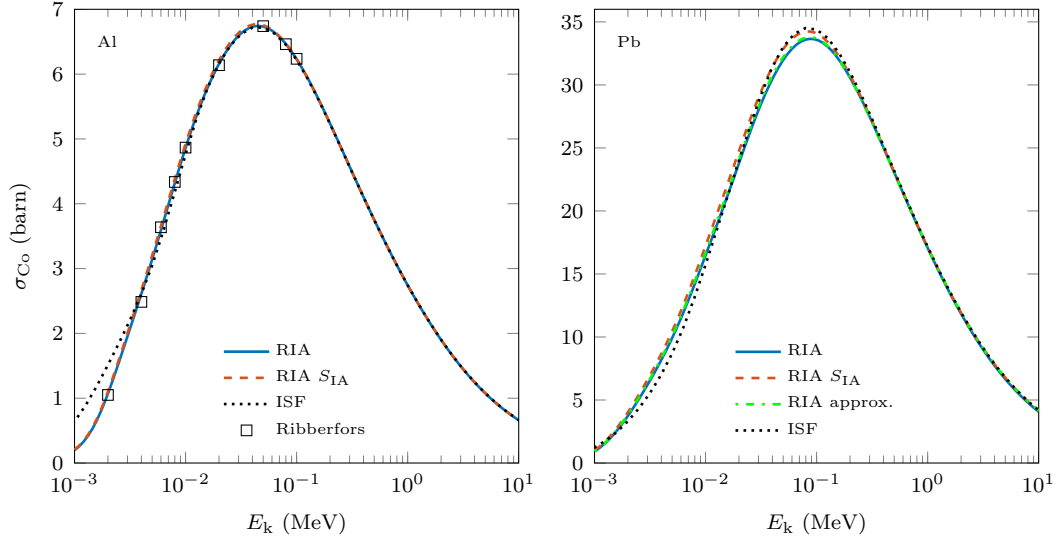
Figure 3.16: Atomic cross sections for Compton scattering per atom for aluminium and lead according to the RIA, Eq. (3.78); the RIA $S_{IA}$, Eq. (3.87); and the ISF approximation, Eq. (3.56). For aluminium, the results according to the RIA given by Ribberfors [57] are also presented. For lead, the cross section according to the RIA approximation Eq. (3.83) is also given. The ISF cross sections are from the EPDL97 [20], the other cross sections were obtained by numerical integration.

binding energies. At this energy, the ISF differs from the RIA more in lead than in aluminium, and there is also some deviation between the RIA and the RIA $S_{IA}$ distributions in lead. When the photon energy increases, the distributions shift to the forward direction, and the other DCSs approach the Klein–Nishina distribution. At 10 MeV in aluminium, the distributions are alike for all models. However, there is slight difference between the RIA and the other models in lead at 10 MeV, which is caused by the $X(R, R')$-term accounting for relativistic effects in the scattering process. Overall, the simple ISF approach is a good approximation when compared with the RIA and the RIA $S_{IA}$ at these energies.

The atomic cross section for Compton scattering is illustrated in Fig. 3.16 for lead and aluminium according to the RIA, the RIA $S_{IA}$, and the ISF approximation. For aluminium, the numerical results for the atomic cross section according to the RIA given by Ribberfors are also presented [57], and for lead, the atomic cross section integrated from Eq. (3.83) is also shown. The RIA $S_{IA}$ results for aluminium are very close to the ones given by the RIA. Also, the values given by Ribberfors agree well with the calculated results. The small differences between the values given by Ribberfors and the ones calculated here may be due to the different binding energies used, which affect the atomic cross section at low photon energies. The atomic cross section according to the ISF approach deviates greatly form the RIA at low energies. However, between 0.02 and 10 MeV, the difference is less than 0.3%. For lead, the differences between the atomic cross sections are much larger than for aluminium. The RIA $S_{IA}$ values are several percent larger than the RIA results below 0.1 MeV,

and the atomic cross section integrated from Eq. (3.83) is much closer to the RIA results below a few hundred keV. This difference between the RIA $S_{\text{IA}}$ and Eq. (3.83) is caused by the approximation $E'_k \approx E_C$ made in Eq. (3.87). The atomic cross section given by the ISF approximation differs greatly from the RIA below 0.02 MeV, for example, the difference is about 15% at 0.003 MeV. The ISF cross section is about 3% higher at 0.05 MeV, but the difference decreases to about 0.5% close to 0.7 MeV. The difference then increases to about 2.5% at 10 MeV.

### 3.4.6   Energy and angular distribution of Compton electrons

So far, only the energy and angular distributions of Compton-scattered photons have been discussed. However, we are also interested in the energy and angular distributions of the recoil electrons produced by Compton scattering. First of all, Compton scattering dominates up to tens of MeV for light elements, and up to several MeV for heavy elements. At high incident photon energies, the Compton scattering DCS in Fig. 3.14 peaks at the low end of the photon spectrum, and therefore a substantial amount of the incident photon energy can be transferred into the kinetic energy of the recoil electron. A part of the kinetic energy of the electron is then transformed into bremsstrahlung photons as discussed in Sec. 5.5. Here, we discuss the energy distribution of recoil electrons according to the RIA and the free electron model. We also represent different angular distribution models for the Compton electrons.

The kinetic energy of the recoil electron ejected from $i$th shell of an atom is simply given by

$$T'_e = E_k - E'_k - E_{b,i}. \tag{3.90}$$

For Compton scattering from a free electron, the DCS differential in electron kinetic energy is obtained by substituting $E'_k = E_k - T'_e$ in Eq. (3.45), giving

$$\left( \frac{d\sigma_{\text{Co}}}{dT'_e} \right)_{\text{KN}} = 2\pi \frac{m_e c^2}{(E_k - T'_e)^2} \left. \left( \frac{d\sigma_{\text{Co}}}{d\Omega} \right)_{\text{KN}} \right|_{E'_k = E_k - T'_e}. \tag{3.91}$$

In the case of the RIA, making the substitution $E'_k = E_k - T'_e - E_{b,i}$ in Eq. (3.78) and integrating over the solid angle gives the DCS

$$\left( \frac{d\sigma_{\text{Co}}}{dT'_e} \right)_{\text{RIA}} = \frac{r_e^2 m_e c}{2E_k} \left( \sum_i f_i H(E_k - T'_e - E_{b,i}) \right.$$
$$\left. \times \int \frac{E_k - T'_e - E_{b,i}}{c\hbar q} \left( 1 + \tilde{p}_z^2 \right)^{-1/2} X(R, R') J_i(p_z) \, d\Omega \right), \tag{3.92}$$

where the substitution is made in the integrand for variables depending on $E'_k$. These DCSs are illustrated in Fig. 3.17 for aluminium and lead at incident photon energies of 0.05, 0.5 and 10 MeV. The DCS given by Eq. (3.91) simply mirrors the Klein–Nishina DCS seen in Fig. 3.14. The RIA DCS (3.92) however is a continuous function of $T'_e$
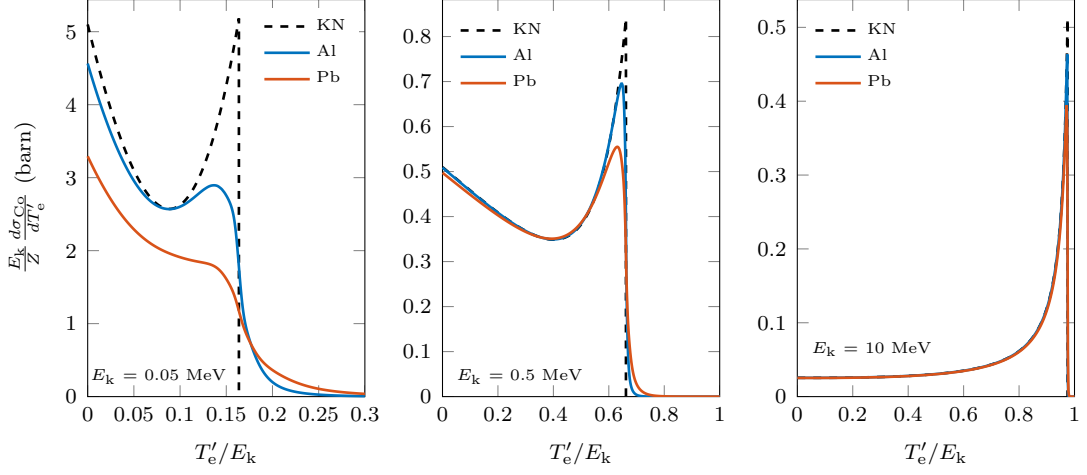
Figure 3.17: Compton DCS differential in the kinetic energy of the recoil electron for aluminium and lead according to the RIA (Eq. (3.92)) and the free electron theory (Eq. (3.91)).

and therefore does not mirror the scattered photon energy distribution. Similarly to Fig. 3.14, the RIA DCS for aluminium is closer to the free electron DCS than for lead. Also, the Doppler broadening of the RIA DCS is evident at low incident photon energies. As the energy increases, the RIA DCS approaches the free electron DCS and peaks at the high end of the spectrum.

In the case of free electron scattering, the angular distribution of the Compton electrons can be derived using the formalism of Sec. 3.4.1. The dot product $\hbar \mathbf{k} \cdot \mathbf{p}'_e$ and the conservation of momentum yields

$$\hbar k p'_e \cos \theta_e = \hbar^2 k^2 - \hbar^2 k k' \cos \theta. \tag{3.93}$$

Using $p'_e$ from Eq. (3.41), the relation of the photon scattering angle and the electron recoil angle can be written as

$$\cos \theta_e = \frac{E_k - E_C \cos \theta}{\sqrt{E_k^2 + E_C^2 - 2E_k E_C \cos \theta}}$$
$$= \left( \frac{E_k}{m_e c^2} + 1 \right) \left[ \frac{E_k}{m_e c^2} \left( \frac{E_k}{m_e c^2} + 2 \right) + \frac{2}{1 - \cos \theta} \right]^{-1/2}, \tag{3.94}$$

where the second equality is obtained after substituting $E_C$ and some algebra. Conversely, the relation can be expressed as

$$\cos \theta = 1 + \frac{2 \cos^2 \theta_e}{\frac{E_k}{m_e c^2} \left( \frac{E_k}{m_e c^2} + 2 \right) (\cos^2 \theta_e - 1) - 1}. \tag{3.95}$$

The DCS differential in electron solid angle is

$$\left( \frac{d\sigma_{Co}}{d\Omega_e} \right)_{KN} = \left( \frac{d\sigma_{Co}}{d\Omega} \right)_{KN} \left| \frac{d\Omega}{d\Omega_e} \right| = \left( \frac{d\sigma_{Co}}{d\Omega} \right)_{KN} \left| \frac{d(\cos \theta)}{d(\cos \theta_e)} \right|, \tag{3.96}$$

where the last term is obtained by differentiating Eq. (3.95):

$$\frac{d(\cos\theta)}{d(\cos\theta_{\mathrm{e}})} = -\frac{4\left(\frac{E_{\mathrm{k}}}{m_{\mathrm{e}}c^2}+1\right)^2\cos\theta_{\mathrm{e}}}{\left[\frac{E_{\mathrm{k}}}{m_{\mathrm{e}}c^2}\left(\frac{E_{\mathrm{k}}}{m_{\mathrm{e}}c^2}+2\right)(\cos^2\theta_{\mathrm{e}}-1)-1\right]^2}. \tag{3.97}$$

Due to the conservation of momentum, the recoil electron angle $\theta_{\mathrm{e}}$ is constrained between 0 and 90°, and the electron momentum vector is on the plane defined by the incident and scattered photon.

In the case of scattering from a bound atomic electron, the angular distribution of the recoil electron is affected by the pre-collision electron momentum. Therefore, the recoil electron momentum is not constrained as in the free electron case discussed above. Nevertheless, the direction of the recoil electron is often approximated with Eq. (3.94). Another approximation used is that the direction of the recoil electron equals to the direction of momentum transfer vector, i.e.

$$\cos\theta_{\mathrm{e}} \approx \cos\theta_q = \frac{E_{\mathrm{k}} - E_{\mathrm{k}}'\cos\theta}{c\hbar q}. \tag{3.98}$$

This approximation also results in a constrained angular distribution. Recently, a new model for calculating the direction of the recoil electron was proposed, called the Monash University Compton scattering model [58], which uses a two-body relativistic three-dimensional scattering framework, resulting in a non-constrained electron angular distribution. We present a similar model called here "$\mathbf{p}_{\mathrm{e}}$ sampling model" but with a simpler formalism than in Ref. [58].

In the $\mathbf{p}_{\mathrm{e}}$ sampling model, the variables $E_{\mathrm{k}}'$, $\theta$, and $p_z$ are assumed to be known variables (e.g., they have been calculated using the sampling method described in Sec. 3.4.8), and the electron distribution of each shell is assumed to be spherically symmetric. The direction of the pre-collision electron can be sampled from an isotropic distribution, which is then used for solving the pre-collision electron momentum from Eq. (3.62) as

$$p_{\mathrm{e}} = -\frac{p_z}{\cos\delta}, \tag{3.99}$$

where $\delta$ is the angle between $\mathbf{p}_{\mathrm{e}}$ and $\mathbf{q}$. If this equation yields a negative $p_{\mathrm{e}}$, the electron direction is rejected and a new direction is sampled. Once a positive $p_{\mathrm{e}}$ is obtained, the recoil electron momentum can then be solved from the conservation of momentum as

$$p_{\mathrm{e}}'c = \sqrt{p_{\mathrm{e}}^2 c^2 + (c\hbar q)^2 - 2c\hbar q p_z c}. \tag{3.100}$$

Note that $p_{\mathrm{e}}'c$ cannot be calculated using the kinetic energy of the recoil electron given by Eq. (3.90), because the conservation of momentum would not hold in this framework. The polar angle of the recoil electron $\theta_{\mathrm{e}}$ can be solved using the dot product $\hbar\mathbf{k}\cdot\mathbf{p}_{\mathrm{e}}'$ together with the conservation of momentum, yielding

$$\cos\theta_{\mathrm{e}} = \frac{E_{\mathrm{k}} - E_{\mathrm{k}}'\cos\theta + p_{\mathrm{e}}\cos\chi}{p_{\mathrm{e}}'c}, \tag{3.101}$$
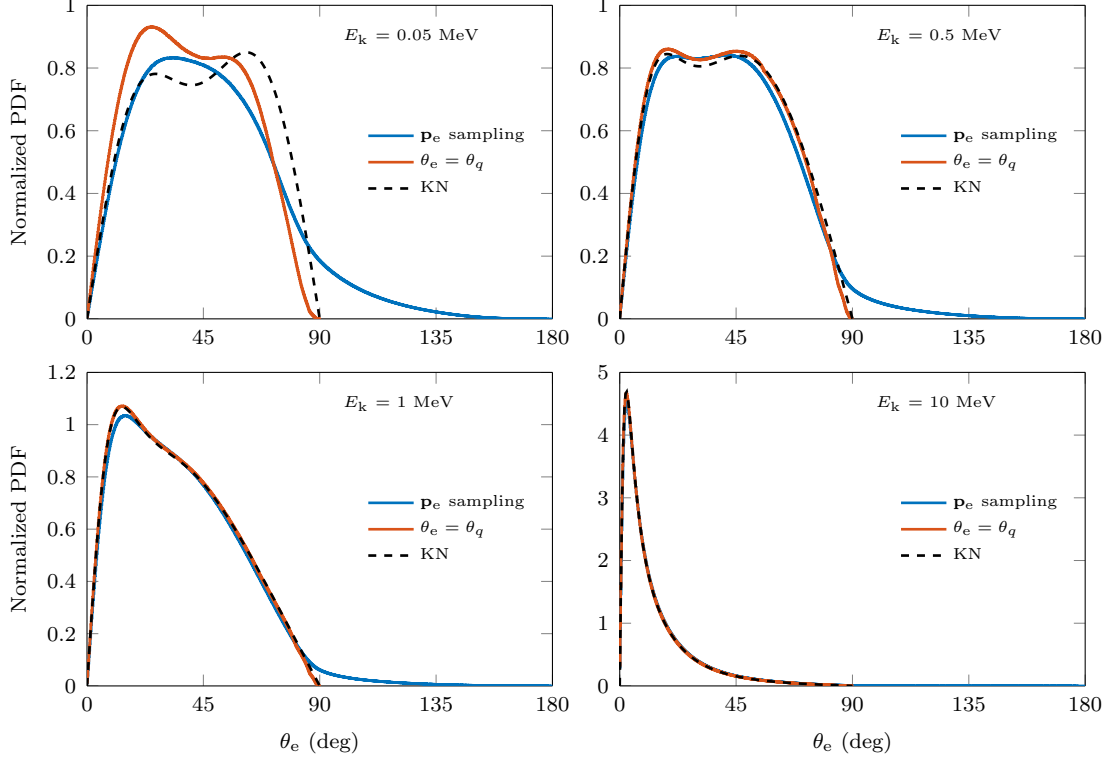
Figure 3.18: Distributions for the polar angle $\theta_e$ of the Compton electrons in lead according to the $\mathbf{p}_e$ sampling model; $\theta_q$ approximation, Eq. (3.98); and the free electron model, Eq. (3.96). The $\mathbf{p}_e$ sampling model and $\theta_q$ results were obtained from Monte Carlo simulations in which the photon directions and energies were sampled as described in Sec. 3.4.8.

where $\chi$ is the angle between $\mathbf{p}_e$ and $\mathbf{k}$. The direction of the electron can then be fully determined using the angle between $\mathbf{p}_e$ and $\mathbf{p}'_e$ defined here as $\alpha$, and the angle between $\mathbf{k}'$ and $\mathbf{p}'_e$ defined as $\beta$. Similarly to Eq. (3.101), these are solved as

$$\cos\alpha = \frac{c\hbar q \cos\delta + p_e c}{p'_e c}, \tag{3.102}$$

$$\cos\beta = \frac{E_k \cos\theta_e + p_e c \cos\alpha - p'_e c}{E'_k}. \tag{3.103}$$

Another angle of interest is the azimuthal angle of the recoil electron, $\phi_e$, which can be calculated from the dot product of the projections of $\mathbf{k}'$ and $\mathbf{p}'_e$ on the plane perpendicular to $\mathbf{k}$ as

$$\cos\phi_e = \frac{\left(\mathbf{k}' - k'\cos\theta\frac{\mathbf{k}}{k}\right) \cdot \left(\mathbf{p}'_e - p'_e \cos\theta_e\frac{\mathbf{k}}{k}\right)}{k'\sin\theta p'_e \sin\theta_e}$$

$$= \frac{\cos\beta - \cos\theta\cos\theta_e}{\sin\theta\sin\theta_e}. \tag{3.104}$$
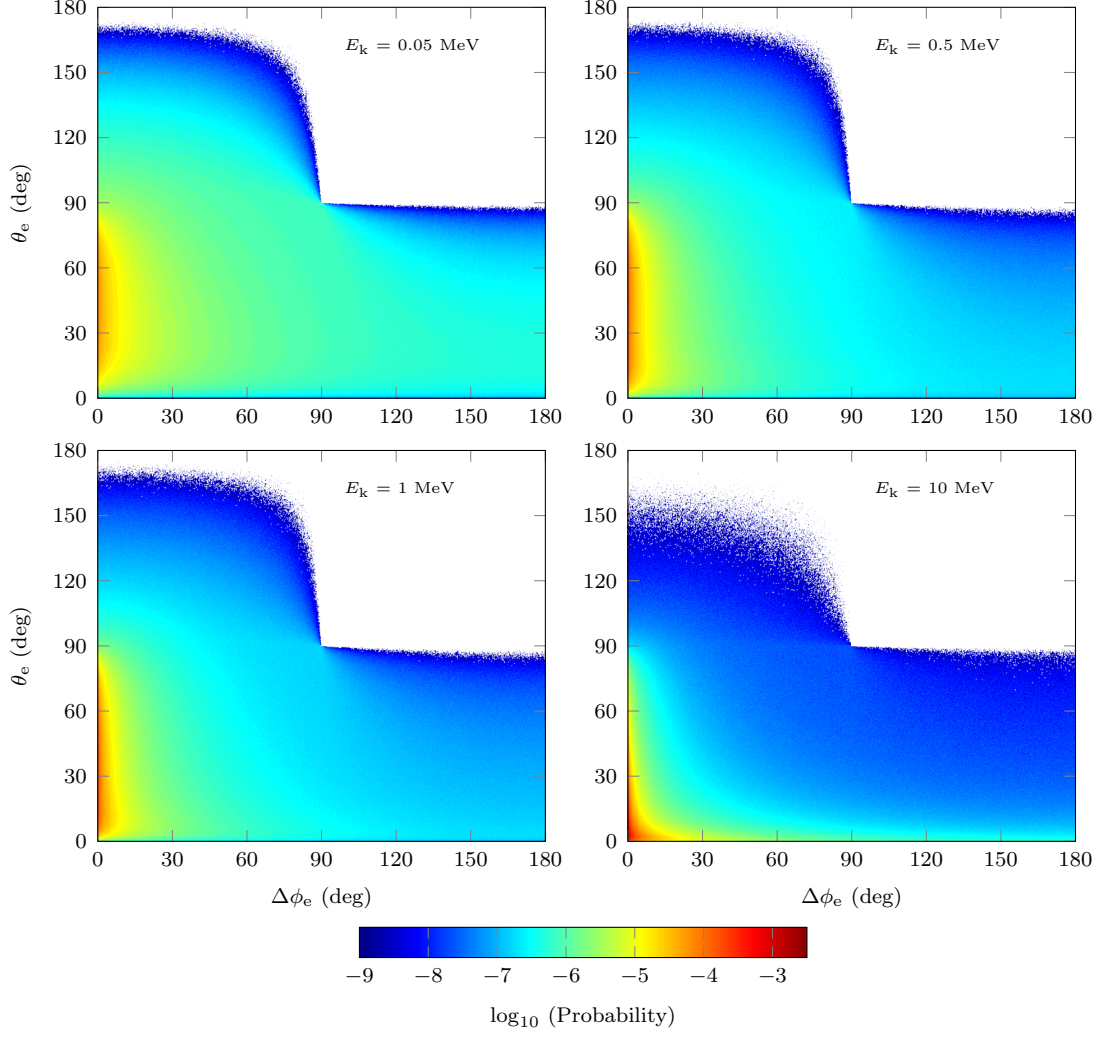
Figure 3.19: Log-probability histograms of the azimuthal angle $\Delta\phi_e = 180° - \phi_e$ and the polar angle $\theta_e$ of the Compton electrons in lead. The angles were calculated using the $\mathbf{p}_e$ sampling model together with the sampling method of photons described in Sec. 3.4.8.

The $\mathbf{p}_e$ sampling model was tested in a Monte Carlo simulation by first sampling $E'_k$, $\theta$ and $p_z$ using the method described in Sec. 3.4.8, and then calculating the polar angle with Eq. (3.101) and the azimuthal angle with Eq. (3.104). This calculation was conducted for lead at incident photon energies of 0.05, 0.5, 1, and 10 MeV. The number of sampled angles was 1 billion in each case. The same calculations were also conducted using the $\theta_q$-approximation in Eq. (3.98). The obtained polar angle distributions are shown in Fig. 3.18 together with the angular distribution of the free electron model given by Eq. (3.96). At 0.05 MeV, the distribution given by the $\mathbf{p}_e$ sampling model differs greatly from the $\theta_q$-approximation as it's not constrained between 0 and 90°, but instead has a thick tail between 90° and 180°. Also, the double-peaked shape of the $\theta_q$ distribution is not present in the $\mathbf{p}_e$ sampling model distribution. As the energy increases, the tail decreases and the $\mathbf{p}_e$ sampling model distribution begins to resemble the $\theta_q$ distribution. At 10 MeV, the distributions are
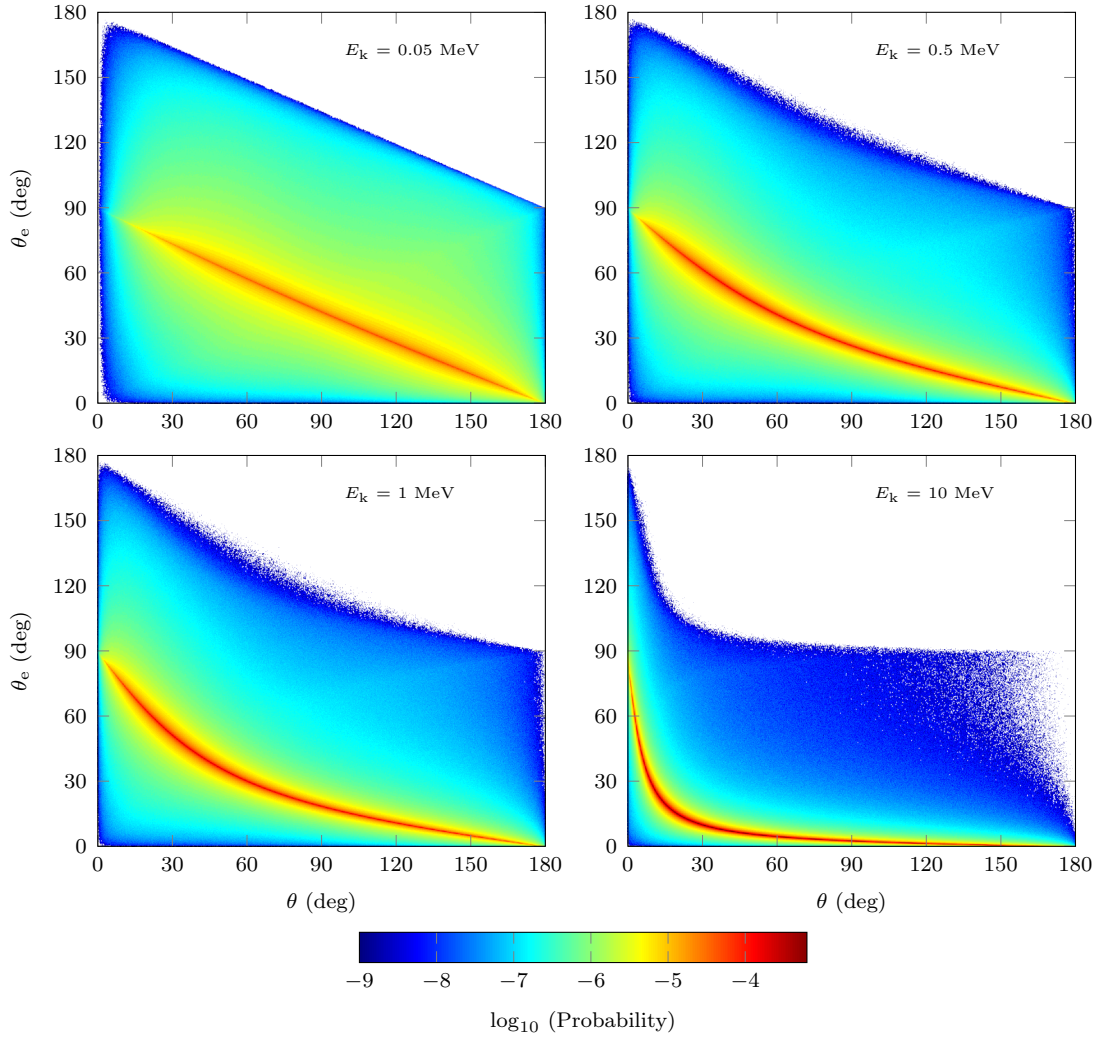
Figure 3.20: Log-probability histograms of photon scattering angle $\theta$ and polar electron angle $\theta_e$ for Compton scattering in lead. The variable $\theta$ was calculated using the sampling method described in Sec. 3.4.8 and $\theta_e$ was calculated with the $\mathbf{p}_e$ sampling model.

almost equal. These results are comparable to the ones obtained in Ref. [58]. The theoretical free electron distribution fails at 0.05 MeV due to neglecting of electron binding and Doppler broadening, but is close to the $\theta_q$ distribution above 0.5 MeV.

The relation between the polar angle $\theta_e$ and the azimuthal angle $\phi_e$ according to the $\mathbf{p}_e$ sampling model is shown in Fig. 3.19 which presents the log-probability histogram of $\theta_e$ and $\Delta\phi_e = 180° - \phi_e$. For all energies, the distribution of $\phi_e$ is highly peaked at 180°, i.e. the recoil electron momentum is on the plane defined by the incident and scattered photon momentum vectors. However, $\phi_e$ is distributed between 0 and 180°, and not confined unlike in the free electron and $\theta_q$ approximations. The distribution is more widespread at low energies.

The log-probability histogram of $\theta$ and $\theta_e$ given by the $\mathbf{p}_e$ sampling model is shown in Fig. 3.20. The general feature for all energies is that a small $\theta$ corresponds to a

value of $\theta_e$ to be close to 90°, and a large $\theta$ corresponds to a small $\theta_e$. However, $\theta_e$ is not confined by the free electron relation of the angles Eq. (3.94), but is distributed between 0 and some maximum value depending on $E_k$ and $\theta$. The most probable value of $\theta_e$ for a given $\theta$ is still given by Eq. (3.94). At 0.05 MeV, the most probable relation between $\theta$ and $\theta_e$ is almost linear. As the incident photon energy increases, the most probable values $\theta$ and $\theta_e$ decrease. Also, large photon scattering angles result in smaller and smaller values of $\theta_e$. At 10 MeV for example, the probability of $\theta_e$ being below 10° is almost 0.9 when $\theta$ is above 30°. The spread of the $\theta$-$\theta_e$ distribution from the free electron relation decreases with increasing incident photon energy.

The presented $\mathbf{p}_e$ sampling model is probably too detailed in respect of this work, taking into account that the TTB approximation is used on the recoil electrons. The differences seen in the polar angle distributions between $\mathbf{p}_e$ sampling model and the $\theta_q$ approximation are non-negligible only at low incident photon energies for which the kinetic energy of the recoil electron is small. Also, at large polar angles the kinetic energy of the electron is smaller on average than at small angles. Because the bremsstrahlung yield is low at low electron energies as discussed in Sec. 5.5, the amount of bremsstrahlung produced by recoil electrons emitted at large polar angles is small. Another important argument is that coarse approximations are made in the TTB model, most importantly the direction of the bremsstrahlung radiation is assumed to be equal to the electron direction. Therefore, the effect of the $\mathbf{p}_e$ sampling model on the angular distribution of bremsstrahlung radiation is expected to be negligible in comparison to the approximations made in the TTB model. However, the $\mathbf{p}_e$ sampling model could be useful in detailed full electron transport calculations if such an option was implemented in the future.

### 3.4.7 Model selection

In an extensive summary by Hubbell [48], numerous experimental results of incoherent scattering factors and the accuracy of $S_{WH}$ values tabulated by Hubbell et al. [34] are discussed. As a general conclusion, Hubbell states that for forward scattering angles and for low- and medium-$Z$ elements, $S_{WH}$ appears to be accurate to the order of 5% or better. For large angles and high-$Z$ elements the tabulated values may be too high by as much as 20%. Nevertheless, Hubbell notes that despite its shortcomings the incoherent scattering function is a useful tool for radiation transport calculations. The ISF approximation is used in many Monte Carlo transport codes to calculate the scattering angle, e.g., in EGS5 and MCNP6. Comprehensive tabulations obtained from more accurate methods such as the S-matrix theory are not available. As was seen in Fig. 3.15, the ISF approach agrees well with the numerically integrated RIA DCS, except at low energies for high-$Z$ elements. However, at low energies the photoelectric effect dominates for high-$Z$ elements, diminishing this error. The results obtained using the RIA $S_{IA}$ weren't significantly better. Also, the scattering angle is much simpler to sample from Eq. (3.56) than using the RIA $S_{IA}$ in Eq. (3.88).

Because of to these factors, we use the incoherent scattering factors given by the EPDL97 [20] for calculating the scattering angle.

As was seen in Fig. 3.14, the ISF approximation fails to describe the energy DCS at low energies. Although the RIA is considered to be more accurate, it is still important to note that the RIA does not take into account the electron binding resulting in Raman–Compton resonances [44]. Another effect neglected by the RIA is the infrared divergence of the cross section at low energies. However, it should be safe to ignore this phenomenon due to the energy range of our interest, and in more generally the bremsstrahlung background is usually larger than the infrared rise [44]. Both of these effects are covered by the S-matrix approach. In comparison with the S-matrix calculations, the main discrepancies of the RIA DDCS generally occur for K-shell electrons in heavy elements [59,60]. Kane [61] has proposed the following conditions for the validity of the RIA by using an empirical examination of experimental results and theoretical calculations:

$$E_k \geq 6E_{b,i}, \tag{3.105}$$

$$E_k - E_C \geq E_{b,i}, \tag{3.106}$$

$$E'_k > 2E_{b,i}. \tag{3.107}$$

The second equation specifies a condition for the validity of the scattering angle, given by

$$\cos\theta \leq 1 - \frac{1}{E/E_{b,i} - 1}\frac{m_e c^2}{E}. \tag{3.108}$$

Under these conditions, the largest errors should exist for scattering from inner-shell electrons of high-$Z$ elements at low incident photon energies compared with the binding energy, and for small scattering angles. However, as the shell interaction probability is approximately proportional to the number of electrons per shell, the error caused by the inner-shell scattering on the whole atom single differential cross section should be small. Also, the conditions (3.105)–(3.107) may be stronger than necessary, especially Eq. (3.106) [61].

The RIA approximation (3.83) was chosen as a basis for calculating the energy of the scattered photon. In general, this is a good approximation to the exact RIA as discussed in Sec. 3.4.5. However, in more detailed comparisons it was noted that the approximation (3.83) results in higher inner-shell probabilities and thus more broadened spectrum, especially for high-$Z$ elements at low energies. Besides the fact that the RIA more or less fails under conditions, there are also other sources of error due to different approximations made. Most importantly, using the ISF approximation for sampling the scattering angle is inconsistent with Eq. (3.83) which naturally introduces some error to the shell probabilities and photon energy distribution. Also, the interpolation, extrapolation and normalization of Compton profiles, and the sampling procedure of the shell involves approximations, which are discussed in the next section. The effect of these sources of error should be revisited in the future. As far as we know, these or other approximations made on the RIA have not been compared in Monte Carlo calculations.

For most parts, the atomic cross sections given by the ISF approach agree well with the integrated RIA cross sections as discussed in Sec. 3.4.5. The calculation and verification of atomic cross sections based on the RIA for all the elements would be too much work for this thesis, mainly because the effect of different variables should be studied, e.g., the binding energies used and normalization of the Compton profiles. Therefore, the ISF atomic cross sections given by the EPDL97 are used.

### 3.4.8 Calculation method

The first part of calculating the direction of the scattered photon is to sample the variable $\mu = \cos\theta$ from the Klein–Nishina DCS (3.44). A variety of methods exist for sampling $\mu$ [62, 63], of which the recommended method for high energies $(E_\mathrm{k}/m_\mathrm{e}c > 1 + \sqrt{3})$ is the direct sampling method given by Koblinger [64]. For lower energies, the rejection sampling method proposed by Kahn [65] has been recommended [66]. Recently, a step sampling with rejection method [63] was recommended over Kahn's method due to higher computational speed. However, because the Kahn's and Koblinger's methods were already implemented in Serpent, and the computational cost of sampling the scattering angle is small compared with the Doppler broadening sampling routine, no changes were made in the previously selected approach. The azimuthal angle of the scattered photon is sampled from a uniform distribution.

Once the variable $\mu$ has been sampled from the Klein–Nishina DCS, the final scattering angle is sampled using the ISF approximation. Eq. (3.56) can be written as a PDF of the variable $\mu$

$$f(\mu) = C \left(\frac{d\sigma_\mathrm{Co}}{d\Omega}\right)_\mathrm{KN} \frac{S_\mathrm{WH}\left(x(\mu), Z\right)}{S_\mathrm{WH}\left(x_\mathrm{max}, Z\right)}, \tag{3.109}$$

where $C$ is a normalization constant. The variable $x(\mu)$ is obtained from Eq. (3.30) as

$$x(\mu) = \frac{E}{\sqrt{2}hc}\sqrt{1 - \mu}, \tag{3.110}$$

and $x_\mathrm{max}$ is given by Eq. (3.36). Because $S_\mathrm{WH}$ is a monotonically increasing function of $x$, the maximum value of $S_\mathrm{WH}$ is obtained at $x_\mathrm{max}$. Therefore, the last term of the PDF (3.109) can be interpreted as a rejection function, i.e. $\mu$ is accepted if

$$\frac{S_\mathrm{WH}\left(x(\mu), Z\right)}{S_\mathrm{WH}\left(x_\mathrm{max}, Z\right)} \geq \xi, \tag{3.111}$$

where $\xi \sim unif(0, 1)$. The incoherent scattering function values $S_\mathrm{WH}\left(x(\mu), Z\right)$ and $S_\mathrm{WH}\left(x_\mathrm{max}, Z\right)$ are interpolated linearly on a log-log scale.

As a default option, the photon energy is sampled from the RIA approximation (3.83), resulting in Doppler-broadened spectrum. However, as was discussed in Sec. 3.4.5, Klein–Nishina equation and the incoherent scattering function method are adequate approximations at high energies. Therefore, an option was included to use mere

Klein–Nishina equation to sample both the direction and energy above a user-set value of incident photon energy. Another option included is to ignore the Doppler broadening completely and to use the incoherent scattering function to determine both the direction and energy of the photon by the relation (3.43).

To sample the Doppler-broadened energy of the scattered photon, Compton profiles and their integrals are needed. Biggs et al. [54] have calculated Hartree–Fock Compton profiles for each shell of the elements $Z = 1 - 102$ for values of $p_z$ ranging from 0 to 100 $\alpha m_e c$. This data introduces some questions about the appropriate extrapolation and interpolation techniques. First of all, the tabulated Compton profiles do not cover the whole range of $p_z$ because $p_{z,\min}/(\alpha m_e c) \approx -137$. Also, the maximum value of $p_z/(\alpha m_e c)$ can be much larger than 100. Taking look at the Compton profiles plotted in Fig. 3.13a, one sees that this isn't much of a problem for outer shells for which the Compton profiles are highly peaked at $p_z = 0$. However, inner shells have much broader distributions, meaning that the $p_z$ grid of the Biggs' data is not sufficient and the Compton profiles must be extrapolated above $p_z/(\alpha m_e c) = 100$. Another issue is the proper interpolation of the Compton profiles which again is more of a problem for broader profiles. As seen in Fig. 3.13a, most of the Compton profile values are given at small values of $p_z$, making linear interpolation sufficient for outer shells. For the broad inner-shell profiles roughly above $p_z/(\alpha m_e c) = 30$, linear interpolation is not adequate as it causes artefacts in the DDCS.

Unfortunately, neither the correct interpolation nor extrapolation method for the Biggs' data are given in the literature. One can however measure the validity of interpolation and extrapolation schemes using the normalization condition given by Eq. (3.75) together with graphical analysis. Linear interpolation and extrapolation on a log-linear scale proved to be reasonably good approximations. Instead of using these interpolation and extrapolation schemes directly, additional points were added to the original Compton profile data using linear interpolation in log-linear scale. The included points were at the $p_z/(\alpha m_e)$ values of 12, 17, 25, 35, 45, 50, 55, 65, 70, 80, 90, 110, 120, 130, and $1/\alpha$. This allows the use of the fast linear interpolation and trapezoidal integration between 0 and $1/\alpha$. Above $1/\alpha$, the extrapolation is used directly. The extrapolated values are given by

$$J_i(p_z) = J_i(p_{z,N})e^{a_i(p_z - p_{z,N})}, \quad p_z > p_{z,N}, \tag{3.112}$$

where

$$a_i = \frac{\ln J_i(p_{z,N}) - \ln J_i(p_{z,N-1})}{p_{z,N} - p_{z,N-1}}, \tag{3.113}$$

and $p_{z,N-1}$ and $p_{z,N}$ are the last two values in the $p_z$ grid of the Biggs' data. Between 0 and $1/\alpha$, Compton profiles are integrated using the trapezoidal rule. Between $1/\alpha$ and $p_{z,\max_i}/(\alpha m_e c)$, integrating Eq. (3.112) gives

$$\int_{m_e c}^{p_{z,\max_i}} J_i(p_z)dp_z = \frac{J_i(m_e c)}{a_i}\left(e^{a_i(p_{z,\max_i} - m_e c)} - 1\right), \quad p_{z,\max_i} > m_e c. \tag{3.114}$$
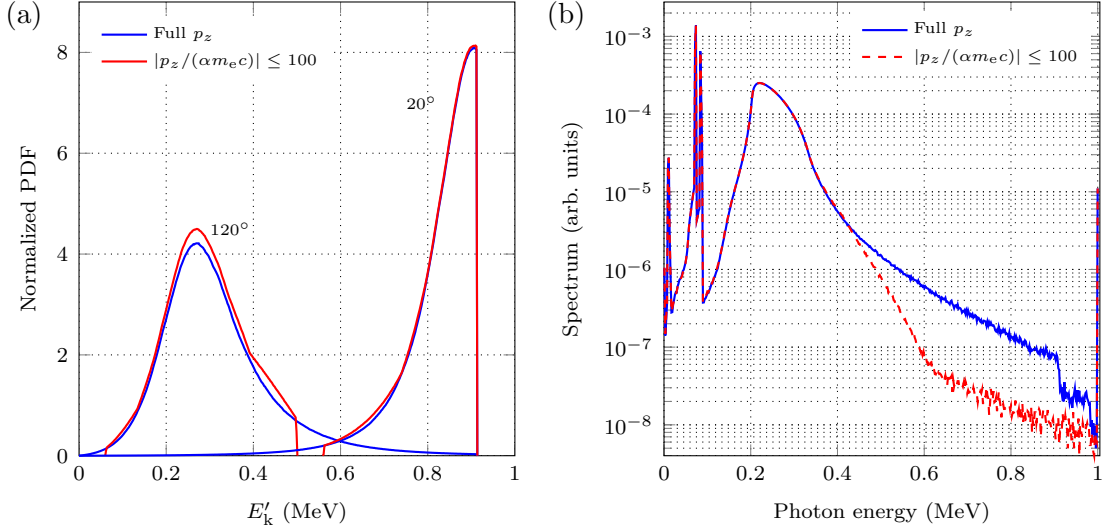
Figure 3.21: (a) Energy distribution of 1 MeV photons scattered from the K-shell electrons of lead at 20° and 120°. (b) Energy spectrum of photons scattered between 90° and 180° from a lead target for a 1 MeV photon beam. The target was a cylinder with a radius of 0.5 cm and height of 1 cm. In the "Full $p_z$" case, $p_z$ was sampled between $p_{z,\mathrm{min}}$ and $p_{z,\mathrm{max}_i}$. In the "$|p_z/(\alpha m_{\mathrm{e}}c)| \leq 100$" case, $p_z/(\alpha m_{\mathrm{e}}c)$ was sampled between $-100$ and $100$ using rejection sampling.

Because $a_i$ is negative, in the limit $p_{z,\mathrm{max}_i} \to \infty$ the integral gives

$$\int_{m_{\mathrm{e}}c}^{\infty} J_i(p_z)dp_z = -\frac{J_i(m_{\mathrm{e}}c)}{a_i}. \tag{3.115}$$

With this scheme, most of the integrated shell-wise Compton profiles are within 1% of unity. However, for very high-$Z$ elements, the integrated K-shell Compton profiles are about 3–4% lower than unity, whereas the integrated $L_1$-shell profiles are 4–5% higher. Therefore the applied interpolation and extrapolation scheme is somewhat incorrect. A better choice would probably be to fit a two-parameter extrapolation function [67] by preserving the correct value of the integrated Compton profile.

The difference between using the Biggs' with and without the added points and extrapolation is illustrated in Fig. 3.21. Fig. 3.21a presents the energy distribution of 1 MeV photons scattered from the K-shell electrons of lead at the angles of 20° and 120°. At the scattering angle of 120°, the distribution obtained using linear interpolation on the original Biggs' data without extrapolation is constrained between 0.06 and 0.5 MeV, and has a deviating shape between 0.4 and 0.5 MeV. Using the added interpolated points and the extrapolation described above fixes these abnormalities. At the scattering angle of 20°, the distributions are much closer to each other, with the exception that in the case of using only the Biggs' data the distribution is constrained above 0.56 MeV. The effect of neglecting the extrapolation of the Biggs' data in a full photon transport simulation is shown in Fig. 3.21b, which presents the energy spectrum of backscattered photons for a 1 MeV photon beam directed at a small lead target. Above 0.4 MeV, the intensity of the spectrum obtained by

using only the Biggs' data is much smaller than obtained with the extrapolation. The maximum relative difference is over an order of magnitude. Therefore, using the Biggs' data without extrapolation can lead into underestimation of the high-end spectrum of backscattered photons. Because the low-end spectrum is dominated mostly by bremsstrahlung photons, the difference in the energies corresponding to the values of $pz/(\alpha m_e c)$ between $-1/\alpha$ and $-100$ is not visible.

In the Doppler broadening of the scattered photon energy, we have decided to use the binding energies given by Biggs instead of the ones included in the EPDL97. The reason for this is that there are some differences in the electron numbers of shells and shell numbering in these two data sets. However, the correct shell number is needed for the atomic relaxation procedure which uses the ENDF/B-VII.1 relaxation data. One option would have been to map the Compton profiles to the shells included in the relaxation data. Instead, a simpler solution was implemented. For most shells, the electron numbers are the same in both data sets, requiring no further action. However, if the electron numbers disagree for a given shell, and the binding energy of the shell is above the cutoff energy $E_{\text{cut}} = 1$ keV, the shell number for the atomic relaxation procedure is determined by a simple sampling routine. The increase in the computational time is small, because most discrepancies in the electron numbers are found for outer shells with binding energies less than $E_{\text{cut}}$. The binding energies given by Biggs are comparable to the ones found in Ref. [25].

The first step in the calculation of the Doppler-broadened photon energy is the sampling of the interaction shell. The exact probability for each shell is given by the integrated shell cross section for a given scattering angle. However, this would require time-consuming numerical integration of each shell cross section. Instead, the shell probability is approximated in the first step by integrating only the Compton profiles, i.e. the probability for photon interacting with the $i$th shell is given by

$$\mathrm{P}_i = \frac{f_i H(E_\mathrm{k} - E_{\mathrm{b},i}) \int_{p_{z,\min}}^{p_{z,\max_i}} J_i\left(p_z\right) dp_z}{\sum_j f_j H(E_\mathrm{k} - E_{\mathrm{b},j} \int_{p_{z,\min}}^{p_{z,\max_j}} J_j\left(p_z\right) dp_z}. \tag{3.116}$$

In the second step, the $E_\mathrm{k}'$ term in Eq. (3.84) is used as rejection function once the scattered photon energy has been calculated, increasing the accuracy of the shell probabilities. In our tests, this approximation yields slightly higher K-shell probabilities for very high-$Z$ elements compared to the numerically integrated values. The probabilities depend also on the scattering angle, naturally. The full analysis of the shell probabilities is left out of this work.

Instead of integrating the Compton profiles for all the shells, rejection sampling is used by first selecting the shell according to the number of electrons per shell, and then using the integrated and normalized Compton profile as a rejection function. Therefore, integration of all the Compton profiles of the atom is not needed. The Compton profiles are normalized and integrated using the created $p_z$ grid as discussed above. The integral of the Compton profile between 0 and $p_z$ is here denoted by

$$K_i\left(p_z\right) \equiv \int_0^{|p_z|} J_i\left(p_z\right) dp_z. \tag{3.117}$$

The shell is sampled using the following algorithm:

(i) Sample the shell number $i$ according to the number of electrons per shell.

(ii) Calculate $p_{z,\max_i}$ from Eq. (3.73).

(iii) Calculate the integral $K_i(p_{z,\max_i})$. If $p_{z,\max_i} \geq m_e c$, the integral is the sum of the integral from Eq. (3.114) and $K_i(m_e c)$. Else, find $|p_{z,\max_i}|$ from the created $p_z$ grid and calculate the integral using the trapezoidal rule.

(iv) The integrated Compton profile is given by

$$\int_{p_{z,\min}}^{p_{z,\max_i}} J_i(p_z)\, dp_z = K_i(m_e c) + \mathrm{sgn}(p_{z,\max_i}) K_i(p_{z,\max_i}). \qquad (3.118)$$

(v) Generate a random number $\xi \sim unif(0,1)$. Accept the shell if

$$\xi \leq \int_{p_{z,\min}}^{p_{z,\max_i}} J_i(p_z)\, dp_z, \qquad (3.119)$$

otherwise, go to step (i).

Once the shell number $i$ has been determined, the photon energy can be sampled using the following algorithm:

(i) Generate a random number $\xi \sim unif(0,1)$. If $p_{z,\max_i} > 0$, set

$$K_{p_z} = \xi \int_{p_{z,\min}}^{p_{z,\max_i}} J_i(p_z)\, dp_z. \qquad (3.120)$$

Then, if $K_{p_z} < K_i(m_e c)$, $p_z$ is negative. Else, $p_z$ is positive, and make a replacement

$$K_{p_z} \Leftarrow K_{p_z} - K_i(m_e c). \qquad (3.121)$$

If $p_{z,\max_i} \leq 0$, set

$$K_{p_z} = K_i(p_{z,\max_i}) + \xi \int_{p_{z,\min}}^{p_{z,\max_i}} J_i(p_z)\, dp_z, \qquad (3.122)$$

and $p_z$ is negative.

(ii) Calculate $p_z$. If $K_{p_z} > K_i(m_e c)$, $p_z$ is given by

$$p_z = m_e c + \frac{1}{a_i} \ln\left[ a_i \frac{K_{p_z} - K_i(m_e c)}{J_i(m_e c)} + 1 \right], \qquad (3.123)$$

which is obtained from Eq. (3.114) using the inverse transform method. Else, find the index $j$ from the integrated Compton profile array which satisfies

$$K_i(p_{z,j}) \leq K_{p_z} < K_i(p_{z,j+1}), \qquad (3.124)$$

and calculate

$$b_j = \frac{J_i(p_{z,j+1}) - J_i(p_{z,j})}{p_{z,j+1} - p_{z,j}}. \tag{3.125}$$

The value of $p_z$ is then given by

$$p_z = \begin{cases} p_{z,j} + \frac{K_{p_z} - K_i(p_{z,j})}{J_i(p_{z,j})} & \text{if } b_j = 0 \\ p_{z,j} + \frac{\sqrt{(J_i(p_{z,j}))^2 - 2b_j(K_i(p_{z,j}) - K_{p_z})} - J_i(p_{z,j})}{b_j} & \text{if } b_j \neq 0 \end{cases}, \tag{3.126}$$

which is obtained using the inverse transform method on a linearly interpolated function as discussed in Sec. 2.2.3. The sign of $p_z$ is set as determined in the previous step.

(iii) Solve the photon energy $E_{\text{k}}'$ using Eq. (3.85).

(iv) Generate a new random number $\xi \sim unif(0, 1)$ and accept the photon energy if

$$\xi E_{\text{k}} \leq E_{\text{k}}', \tag{3.127}$$

otherwise, go to step (i) of the shell sampling algorithm.

The last step of this algorithm takes into account the $E_{\text{k}}'$ term in Eq. (3.84), as already mentioned.

The energy of the recoil electron is given by Eq. (3.90) and the direction is approximated to be equal to direction of the momentum transform vector as discussed in Sec. 3.4.6. Alternatively, the direction can be determined using the "$\mathbf{p}_{\text{e}}$ sampling model" discussed in Sec. 3.4.6. The direction of the electron is then solved from the angles given by Eqs. (3.101), (3.102), and (3.103). Once the electron energy and direction have been determined, the TTB approximation is used for the electron as explained in Sec. 5.5. The vacancy left in the electron shell is treated with the atomic relaxation procedure discussed in Sec. 4. The energy deposited in the Compton scattering event is calculated as

$$E_{\text{dep,Co}} = E_{\text{dep,AR}} + E_{\text{dep,TTB}}, \tag{3.128}$$

where $E_{\text{dep,AR}}$ and $E_{\text{dep,TTB}}$ are the energies deposited in the atomic relaxation and TTB processes given by Eqs. (4.7) and (5.23), respectively. Note that because different binding energies are used in the atomic relaxation and Compton scattering routines, energy conservation is violated here. The study of the significance of this violation and possible corrections are left for future work.

## 3.5   Electron-positron pair production

Electron-positron pair production can occur when a photon interacts with the field of a charged particle, such as a nucleus or an electron. The photon is absorbed in

the process and its energy is transformed into the masses and kinetic energy of the created pair, and also into the kinetic energy of the target particle. Pair production is the dominant photon interaction for low-$Z$ elements at photon energies of above 100 MeV, and for high-$Z$ elements at energies of above a few MeV. For example, for uranium, pair production has the highest atomic cross section of the photon interactions at energies above 5 MeV. It is important to model pair production correctly because a significant portion of the energy of the pair is transformed into bremsstrahlung radiation, especially in heavy elements at high energies. Also, the generated positron eventually annihilates with an electron, which results in the emission of two 0.511 MeV photons. Therefore, a part of the energy of the incident photon is always transformed into at least two new energetic photons.

Due to the conservation of momentum, pair production cannot occur in free space, and thus, a target particle is always required. When the pair production occurs in the field of a nucleus, most of the photon energy is transformed into the rest mass and kinetic energy of the electron-positron pair. The amount of energy received by the nucleus is small due to its large mass compared with the rest mass of electron, and therefore, the electron-positron pair can be assumed to obtain the whole photon energy. Also due to the mass difference, the threshold energy for pair production in the field of a nucleus is approximately given by the rest mass energy of the generated pair, i.e $2m_{\mathrm{e}}c^2 \approx 1.022$ MeV. The atomic cross section for pair production in the field of a nucleus is approximately proportional to $Z^2$ [22].

If the pair production occurs in the field of an atomic electron, energy and momentum can be transferred to the atom by ionization or excitation. The pair production by ionization is called triplet production because the target electron is ejected from the atom. The threshold photon energy for this process is $4m_{\mathrm{e}}c^2 \approx 2.044$ MeV when the binding energy of the target electron is ignored [68]. Pair production by excitation can occur below this threshold energy, but with a very small cross section [68]. Often, pair production by excitation is also included under the term triplet production. The atomic cross section for triplet production is proportional to $Z$ [22].

According to Ref. [28], all general-purpose Monte Carlo codes treat triplet production as pair production, i.e. the transport of the target electron is not simulated. We have also decided to exclude the simulation of triplet production because it is relatively unimportant, and the differential cross section models of triplet production are more complicated than the ones of pair production. Omitting the triplet production means that the energy of the electron-positron pair is slightly overestimated. This on the other hand results in an overestimation of the bremsstrahlung radiation, because the bremsstrahlung yield increases with the energy of electron or positron. However, we can reason that the overall effect of neglecting triplet production is small. First of all, the ratio of the atomic cross section of triplet production and pair production is approximately $1/(\eta Z)$ [22], where the parameter $\eta$ is above 1.5 at photon energies below 10 MeV and approaches unity at higher energies. Therefore, triplet production is relatively unimportant for high-$Z$ elements, but it can make a significant contribution for low-$Z$ elements, especially at high energies. However,

experimental results and theoretical models [69] show that for hydrogen, the recoil momentum of the target electron becomes negligible at photon energies of above a few tens of MeV. The recoil momentum can be important at least below 6 MeV [70]. However, pair production is important in light elements for energies above 10–100 MeV. For example, for 10 MeV in hydrogen, the ratio of the pair production cross section to the total photon cross section is about 6% [68]. Another important fact is that the bremsstrahlung yield is low at small electron energies, especially for low-$Z$ elements. Therefore, it should be reasonably safe to neglect triplet production. Also, the binding energy of the recoil electron is small compared with the energy of the electron-positron pair, and therefore it can also be ignored.

Extensive calculations for the atomic cross sections of pair and triplet production for elements $Z = 1$–100 at photon energies from the threshold energy to 100 GeV have been performed by Hubbel et al. [68]. These cross sections are based on combinations of various theoretical models, which are too complicated to be covered here. This dataset is included in the EPDL97 library [20] and is commonly used in Monte Carlo codes. The cross sections are considered to be quite accurate, the improvement to the values by using more accurate models is expected to be 2–3% at most [71].

In order to simulate a pair production event, a differential cross sections is needed for sampling the energy and direction of the pair. However, a complete and accurate theoretical model applicable to Monte Carlo simulations for all energies has not been developed. Therefore, we apply some commonly used approximations and present a new method for fast sampling of the energy of the pair. This model is compared with the energy distributions used in PENELOPE and Geant4 Monte Carlo transport codes, and also to more accurate theoretical results.

### 3.5.1 Energy distribution of electron-positron pair

Due to the assumption that the energy of the photon is completely given to the created pair, the energy DCS can be given with respect to the electron reduced energy, defined as

$$\epsilon = \frac{T_e + m_e c^2}{E_k}. \tag{3.129}$$

The minimum and maximum of the reduced energy are obtained when the kinetic energy of the electron or positron is zero, i.e.

$$\epsilon_{min} = \frac{m_e c^2}{E_k},$$

$$\epsilon_{max} = \frac{(E_k - 2m_e c^2) + m_e c^2}{E_k} = 1 - \epsilon_{min}. \tag{3.130}$$

As a starting point for the energy distribution, we use the commonly applied single differential cross section given by Davies, Bethe, and Maximon [72]

$$\left(\frac{d\sigma_{\text{pp}}}{d\epsilon}\right)_{\text{DBM}} = \alpha Z^2 r_e^2 \left[ \left(2\epsilon^2 - 2\epsilon + 1\right)\left(\Phi_1(\zeta) - \frac{4}{3}\ln Z - 4f_{\text{C}}(Z)\right) \right.$$
$$\left. +\frac{2}{3}\epsilon(1-\epsilon)\left(\Phi_2(\zeta) - \frac{4}{3}\ln Z - 4f_{\text{C}}(Z)\right)\right], \qquad (3.131)$$

where the screening functions $\Phi_1(\zeta)$ and $\Phi_2(\zeta)$ take into account the screening effect due to the atomic electrons, and $f_{\text{C}}$ is the Coulomb correction function.

The screening functions $\Phi_1(\zeta)$ and $\Phi_2(\zeta)$ involve integral functions depending on the variable $\zeta$, defined as

$$\zeta = \frac{100}{Z^{1/3}}\frac{\epsilon_{\min}}{\epsilon(1-\epsilon)}, \qquad (3.132)$$

and the atomic form factor $F(q, Z)$ discussed in Sec. 3.3.1. Because the integral functions can only be solved numerically, analytical approximations must be used for $\Phi_1(\zeta)$ and $\Phi_2(\zeta)$. We use the following approximations given in Ref. [73]:

$$\Phi_1(G) = \begin{cases} 20.867 - 3.242G + 0.625G^2 & , G \leq 1 \\ 21.12 - 4.184\ln(G + 0.952) & , G > 1 \end{cases}, \qquad (3.133)$$

and

$$\Phi_2(G) = \begin{cases} 20.209 - 1.930G - 0.086G^2 & , G \leq 1 \\ \Phi_1(G) & , G > 1 \end{cases}, \qquad (3.134)$$

where $G = 1.36\zeta$. These equations are derived using the atomic form factors for Thomas–Fermi model of atoms which is reasonably accurate for elements with $Z \geq 5$. More accurate calculations of the screening functions for Thomas–Fermi atoms are given in Ref. [74]. According to Ref. [8], Eqs. (3.133) and (3.134) agree very well with these calculations; their difference is less than 0.4% for $Z \geq 5$. For hydrogen, the values of Eqs. (3.133) and (3.134) are within 5% of the estimates given by Ref. [74].

Eq. (3.131) is the same as the differential cross section given by Bethe and Heitler [75] with the exception of the Coulomb correction function

$$f_{\text{C}}(Z) = a^2 \sum_{n=1}^{\infty} \frac{1}{n^2(n^2 + a^2)}$$
$$\approx a^2 \left[(1 + a^2)^{-1} + 0.202059 - 0.03693a^2 + 0.00835a^4 \right.$$
$$\left. - 0.00201a^6 + 0.00049a^8 - 0.00012a^{10} + 0.00003a^{12}\right], \qquad (3.135)$$

where $a = \alpha Z$. This correction function was introduced in Eq. (3.131) because the Bethe–Heitler cross section was derived using the Born approximation, which neglects the higher-order terms of the perturbation series of the Coulomb interaction. Strictly speaking, Eq. (3.135) is the first term of the Coulomb correction series, and it has a good accuracy only at high photon energies of above 100 MeV [68]. Below

5 MeV, exact calculations for the Coulomb correction for all elements have been obtained [76], and between 5 and 20 MeV, some calculations have been performed using the distorted wave Born approximation (DWBA), as compiled in Ref. [77]. However, no comprehensive model for the differential cross section has been presented between the energies of 5 and 100 MeV.

If Eq. (3.131) is used with the Coulomb correction function given by Eq. (3.135) without any further corrections, the boundaries of $\epsilon$ are shifted above $\epsilon_{\min}$ and below $\epsilon_{\max}$ at low energies. This effect is notable especially for high-$Z$ elements, even at photon energies of about 15 MeV. Another issue with Eq. (3.131) is that with the screening and correction functions defined above, the DCS is symmetric about $\epsilon = 1/2$, meaning that that electrons and positrons have identical energy distributions. However, this is physically incorrect because the electric field of an atom accelerates positrons and decelerates electrons, which is especially seen in heavy elements at low energies. The differential cross section becomes asymmetric so that the probability of low-energy electrons and high-energy positrons increases, i.e. the mean is shifted below $\epsilon = 1/2$ [78].

As there is no detailed model for the differential cross section below 100 MeV, we use the Coulomb correction function $f_{\mathrm{C}}(Z)$ for all energies. To overcome the physically incorrect shifted boundaries of $\epsilon$, we use the correction factor $F_0(\epsilon_{\min}, Z)$ used in PENELOPE code [7], defined as

$$
\begin{aligned}
F_0(\epsilon_{\min}, Z) = {} & -(0.1774 + 12.10a - 11.18a^2)(2\epsilon_{\min})^{1/2} \\
& + (8.523 + 73.26a - 44.41a^2)(2\epsilon_{\min}) \\
& - (13.52 + 121.1a - 96.41a^2)(2\epsilon_{\min})^{3/2} \\
& + (8.946 + 62.05a - 63.41a^2)(2\epsilon_{\min})^2.
\end{aligned} \tag{3.136}
$$

This factor has been determined by requiring that the atomic pair production cross section coincides with the tabulated values given in Ref. [68]. Even with this correction factor, the minimum and maximum $\epsilon$ are slightly shifted for higher-$Z$ elements above photon energies of 11 MeV. However, the shift is so small that it can be safely ignored. To our knowledge, the asymmetry of the differential cross section at low energies is neglected in the commonly used Monte Carlo photon transport codes. As we are not aware of any detailed model taking the asymmetry into account, we have also decided to ignore it. We summarize the differential cross section which is used for sampling the variable $\epsilon$:

$$
\frac{d\sigma_{\mathrm{pp}}}{d\epsilon} = \left(2\epsilon^2 - 2\epsilon + 1\right)\phi_1(\epsilon, E_{\mathrm{k}}, Z) + \frac{2}{3}\epsilon(1-\epsilon)\phi_2(\epsilon, E_{\mathrm{k}}, Z), \tag{3.137}
$$

where

$$
\phi_1(\epsilon, E_{\mathrm{k}}, Z) = \Phi_1(G) - \frac{4}{3}\ln Z - 4f_{\mathrm{C}}(Z) + F_0(\epsilon_{\min}, Z), \tag{3.138}
$$

$$
\phi_2(\epsilon, E_{\mathrm{k}}, Z) = \Phi_2(G) - \frac{4}{3}\ln Z - 4f_{\mathrm{C}}(Z) + F_0(\epsilon_{\min}, Z). \tag{3.139}
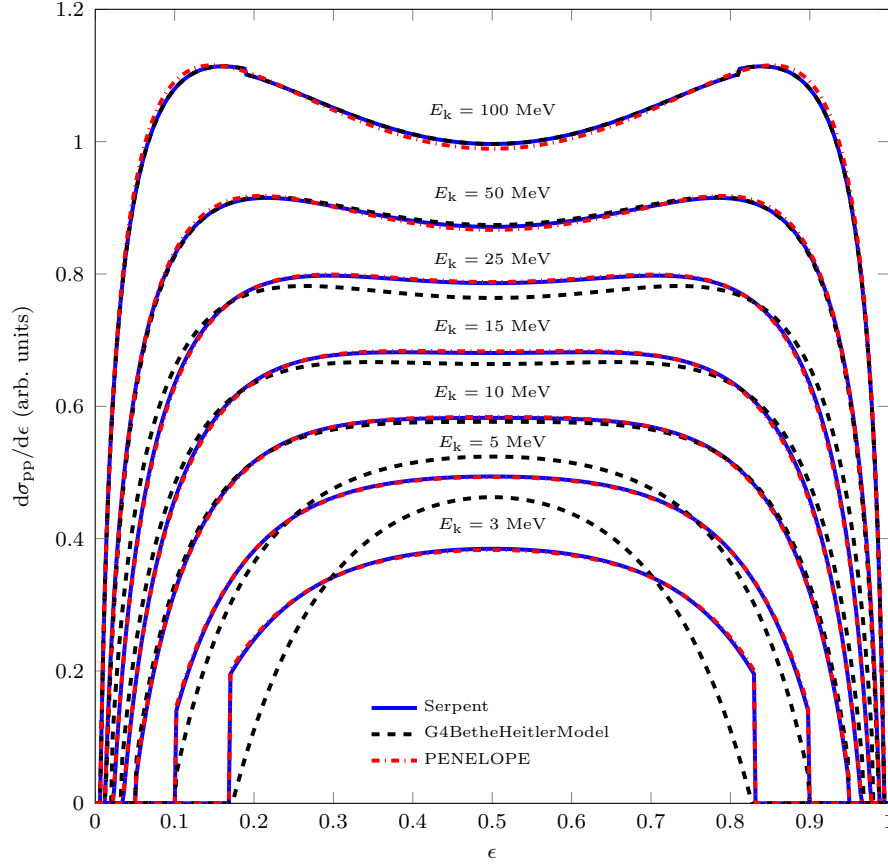$$

Figure 3.22: Normalized differential cross section for pair production as a function of the electron reduced energy in uranium for several photons energies according to Eq. (3.137) (Serpent), G4BetheHeitlerModel in Geant4, and PENELOPE. The distributions are scaled for illustration purposes.

Note that Eq. (3.137) is given here without constant factors.

The presented differential cross section model was compared with the ones used in PENELOPE [7] and Geant4 (G4BetheHeitlerModel) [13]. All the models are based on the Davies–Bethe–Maximon (or the Bethe–Heitler) differential cross section, though some differences exist between them. In the Geant4 model, the Coulomb correction function is used only at energies of above 50 MeV. The PENELOPE model uses more complex screening functions than the ones given by Eqs. (3.133) and (3.134). The differential cross sections given by these three models are shown in Fig. 3.22 in uranium for photon energies between 3 and 100 MeV. In general, the model presented here is in a good agreement with the PENELOPE model at all energies. Negligible differences exist at high energies close to $\epsilon = 1/2$. Also, small discontinuities caused by the screening functions (3.133) and (3.134) can be seen at 100 MeV. Between 10 and 50 MeV, the Geant4 distribution is slightly broader than the other two, and it becomes narrower below 5 MeV. For low-$Z$ elements, the differences between the differential cross sections are similar.
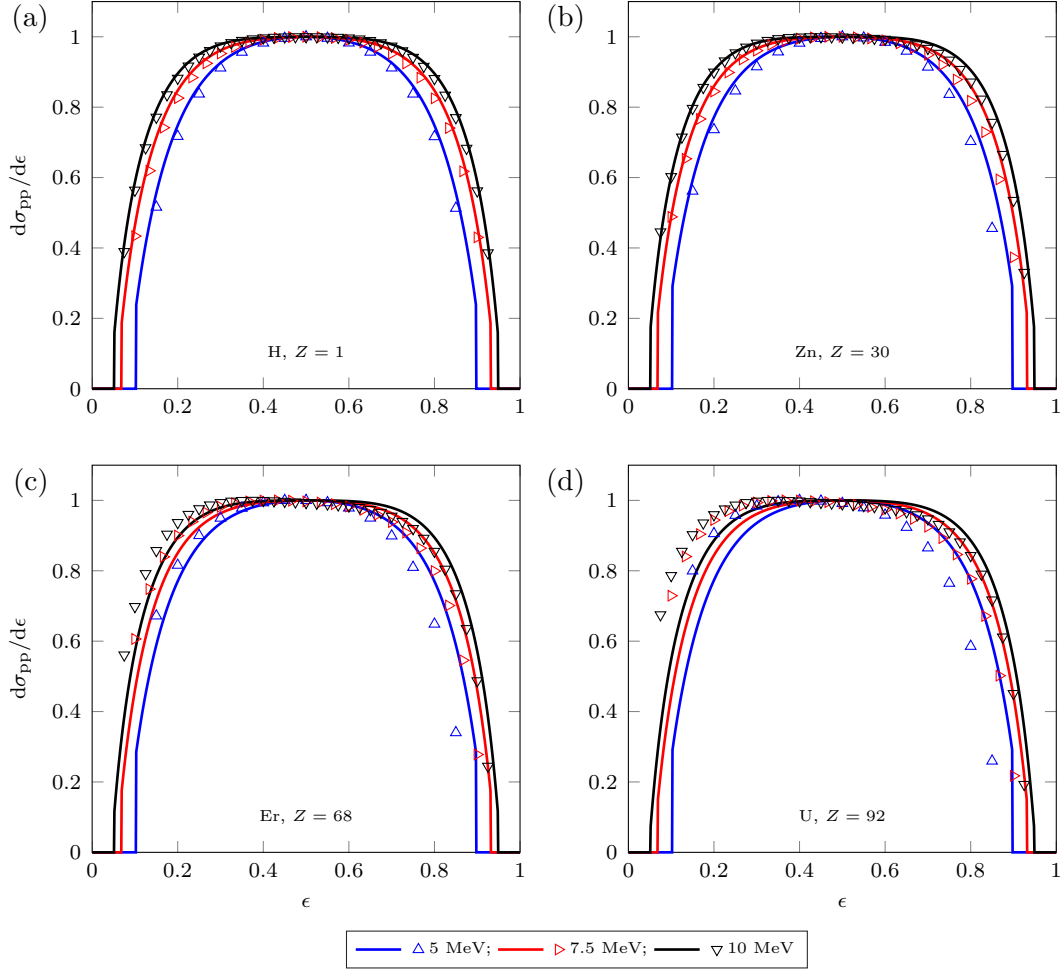
Figure 3.23: Differential pair production cross section as a function of the electron reduced energy for (a) hydrogen, (b) zinc, (c) erbium, and (d) uranium at photon energies of 5, 7.5, and 10 MeV. Solid lines represent the distribution given by Eq. (3.137) and the triangular markers represent the DWBA results given by Ref. [79]. The distributions are normalized to unit maximum.

The presented model was also compared with the more accurate DWBA calculations performed in Ref. [79] for four elements at energies of 5, 7.5, and 10 MeV. The comparison is shown in Fig. 3.23. For low-$Z$ elements, the presented model agrees very well with the DWBA results. However, for high-$Z$ elements, the DWBA differential cross section is clearly shifted towards the lower $\epsilon$ values. This feature is present even at the photon energy of 10 MeV. Therefore, the number of high-energy positrons and low-energy electrons are underestimated in heavy elements in symmetric pair production models. The way this affects the total bremsstrahlung yield of electrons and positrons is not trivial to see because the yield increases with the energy of a charged particle, but on the other hand, positrons have lower yield than electrons. However, because the thick-target bremsstrahlung model discussed in Sec. 5.5 is a rough approximation, the error introduced by using a symmetric DCS might be small compared with other errors.

To sample $\epsilon$ from Eq. (3.137), we use the rejection sampling method discussed in Sec. 2.2.2 by employing the maximum of Eq. (3.137) as a majorizing function. The sampling algorithm proceeds as follows:

(i) Generate a random variate $\epsilon_u \sim unif(\epsilon_{\min}, \epsilon_{\max})$ and $\xi \sim unif(0,1)$.

(ii) If $\xi \max_{\epsilon} \frac{d\sigma_{\mathrm{pp}}}{d\epsilon} \leq \frac{d\sigma_{\mathrm{pp}}}{d\epsilon}(\epsilon_u)$, accept $\epsilon_u$. Else, go to step (i).

This method provides a good efficiency because the differential cross section is close to a uniform distribution when the photon energy is below about 100 MeV. The efficiency is between about 82% and 90% in the energy range from 2 MeV to 10 MeV, and it increases to above 90% when the photon energy is 100 MeV. The maximum of Eq. (3.137) can be accurately approximated with a rational function

$$\Lambda(E_{\mathrm{k}}, Z) = \frac{p_1(Z)E_{\mathrm{k}}^2 + p_2(Z)E_{\mathrm{k}} + p_3(Z)}{E_{\mathrm{k}}^2 + q_1(Z)E_{\mathrm{k}} + q_2(Z)}. \tag{3.140}$$

To use this approximation, the maximum of Eq. (3.137) was numerically calculated at 10,000 equidistant points in the photon energy range from 2 to 100 MeV for all the elements. Eq. (3.140) was then fitted to the calculated maxima by requiring that the ratio of the fitted model to the calculated maxima was between 1.0001 and 1.02 at all points. In fact, the ratio was 1.01–1.02 between 2 and 3 MeV, and 1.0001–1.005 above 12 MeV for all the elements. The solved coefficients $p_1(Z)$, $p_2(Z)$, $p_3(Z)$, $q_1(Z)$, and $q_2(Z)$ for $Z = 1$–$100$ are given in Tables A.1 and A.2 in Appendix A.

Note that below about 10 MeV, the maximum of Eq. (3.137) is obtained at $\epsilon = 1/2$, however, it is slightly faster to use the rational function fit instead of the direct calculation due to the logarithm in Eq. (3.133). The rational function fit (3.140) begins to fail below 2 MeV. Instead of calculating the maximum at $\epsilon = 1/2$, $\epsilon$ is then sampled uniformly between $\epsilon_{\min}$ and $\epsilon_{\max}$ which should not introduce any significant error. Above 100 MeV, it should be possible to employ the sampling method used in PENELOPE [7]. However, this was not implemented or tested because it is above the energy range of our current interest.

Once the energy of the electron and positron have been determined, their direction is sampled as discussed in the next section. The TTB approximation is then applied for both particles as specified in Sec. 5.5. Electron-positron annihilation is simulated as discussed in Sec. 3.5.3. The energy deposited in the pair production event is calculated as

$$E_{\mathrm{dep,pp}} = E_{\mathrm{dep,TTB,e}} + E_{\mathrm{dep,TTB,p}}, \tag{3.141}$$

where $E_{\mathrm{dep,TTB,e}}$ and $E_{\mathrm{dep,TTB,p}}$ are the energies deposited by the electron and positron, respectively, which are given by Eq. (5.23).

### 3.5.2 Angular distribution of electron-positron pair

Besides the kinetic energy of the electron-positron pair, we need to sample the direction of the particles. A compilation of different theoretical cross sections

differential in positron energy and direction is given in Ref. [78]. However, these cross sections are rather complicated to sample. Fortunately, a detailed model of the angular distribution is usually not needed in full electron transport simulations or with the TTB approximation. Considering full electron transport, electrons and positrons scatter multiple times right after their production, and therefore the effect of the initial angular distribution will be somewhat lost in the process. Also, the mean free path of electrons and positrons is small compared with the one of photons, and hence the particles lose their energy in the vicinity of the pair production site. A more accurate distribution might be needed in applications where the electron-positron pair is measured before multiple scattering occurs [8]. However, in our case, the TTB approximation is used for electrons and positrons. In our TTB model, the direction of the bremsstrahlung radiation is not sampled but is instead assumed to be equal to the direction of the charged particle. This approximation is likely to be the main source of error for the direction of bremsstrahlung photons. Also, as already noted, the bremsstrahlung yield increases with the energy of the charged particle. Therefore, it should be sufficient to use a simple high-energy approximation of the angular distribution, as the low-energy electrons and positrons contribute only a small amount to the total bremsstrahlung yield.

In the currently used Monte Carlo codes, at least a couple of different models are used for sampling the polar emission angles $\theta_e$ and $\theta_p$ illustrated in Fig. 3.1d. For example, ETRAN-based codes [80] and PENELOPE [7] use the leading order term of the Sauter–Gluckstern–Hull distribution (Eq. 3D-2000 in Ref. [78]), which is given by

$$\left(\frac{d\sigma_{pp}}{d\Omega_e}\right)_{SGH} \approx C \frac{1}{(1 - \beta_e \cos\theta_e)^2}, \tag{3.142}$$

where $C$ is a constant term and $\beta_e$ is given by Eq. (3.12). Eq. (3.142) also holds for positrons when replacing $\beta_e$ by $\beta_p$ and $\theta_e$ by $\theta_p$. This distribution is also used in EGS5 below 4.14 MeV [8], otherwise EGS5 uses the more complicated Schiff distribution (Eq. 3D-2003 in Ref. [78]). Geant4 (G4BetheHeitlerModel) employs an approximation of the distribution given by Tsai [74]. Eq. (3.142) and the Geant4 model depend only on the electron/positron energy whereas the Schiff distribution depends on both of them and also on the photon energy and the atomic number. The Geant4 model and Eq. (3.142) are compared in Fig. 3.24 for electron kinetic energies of 0.1, 1, 3, 10, 30, and 50 MeV. Eq. (3.142) is more forward-peaked but the two models are still quite close to each other. Also, according to the comparison made in Ref. [81], the Geant4 model agrees reasonably well with the Schiff distribution when the total energy of the electron is between 3.5 and 100 MeV. Therefore, Eq. (3.142) should be sufficiently accurate when compared with these models.

Due to its simplicity and reasonably good accuracy, we have chosen to use Eq. (3.142) for sampling the polar emission angles. The normalized PDF of Eq. (3.142) is the same as Eq. (3.17), and therefore, the polar emission angle is straightforward to sample using Eq. (3.19). The angles $\theta_e$ and $\theta_p$ are sampled independently from each other. Because only unpolarized photons are considered, the azimuthal angle of
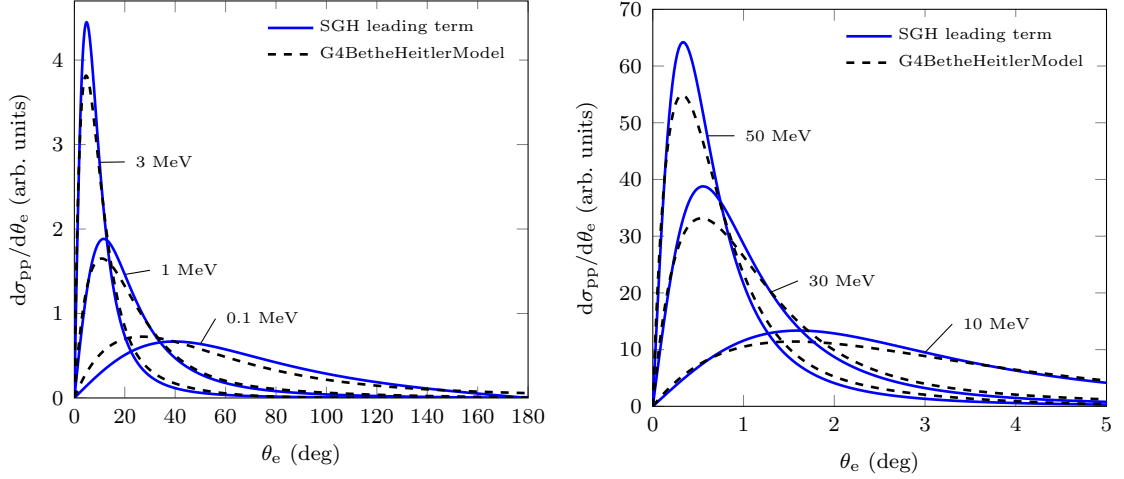
Figure 3.24: Normalized differential cross section for pair production as a function of the polar emission angle of the electron according to Eq. (3.142) (SGH leading term) and Geant4 (G4BetheHeitlerModel) for different electron kinetic energies.

one of the particles can be sampled from a uniform distribution. We assume that the direction vectors of the pair and the incident photon are coplanar. As pointed out in Ref. [82], this approximation is correct only for photon energies above about 200 MeV. However, as already pointed out, the benefit of a more accurate angular distribution model would most likely be insignificant.

### 3.5.3 Electron-positron annihilation

After a positron is generated in pair production, it slows down due to collision and radiative energy losses with atoms. Eventually, the positron interacts with an electron, which results in the annihilation of both particles and the production of one or more photons. The energy of the emitted photons is equal to the rest mass and kinetic energies of the positron and electron, when the possible binding energy of the electron and the recoil of a nucleus are ignored. Usually, positron annihilation results in the emission of two photons, both having energy equal to $m_e c^2 \approx 0.511$ MeV.

Annihilation can be modelled by three mechanisms which determine the number of produced photons. The most probable annihilation process occurs when the electron is essentially free, i.e. when the electron binding can be ignored. Due to the conservation of momentum, at least two photons must be emitted, which is also the most probable process. The annihilation can occur in-flight or after the thermalization of the positron. The two-photon annihilation cross section for a positron with a kinetic energy $T_p$ and electron at rest is given by Heitler [83] as

$$\sigma_{2\gamma} = \frac{\pi r_e^2}{\gamma + 1} \left[ \frac{\gamma^2 + 4\gamma + 1}{\gamma^2 - 1} \ln\left(\gamma + \sqrt{\gamma^2 - 1}\right) - \frac{\gamma + 3}{\sqrt{\gamma^2 - 1}} \right], \tag{3.143}$$
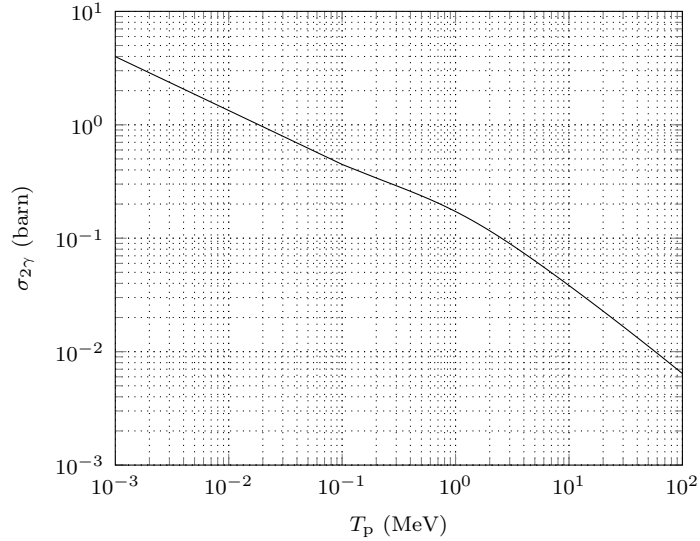
Figure 3.25: Two-photon electron-positron annihilation cross section according to Eq. (3.143) as a function of the kinetic energy of positron.

where $\gamma = 1 + T_\mathrm{p}/(m_\mathrm{e}c^2)$ is the Lorentz factor. This cross section is plotted in Fig. 3.25, which shows that the annihilation probability increases significantly as the positron slows down. Therefore, the majority of positrons annihilate at low energies. The energy distribution of the emitted photons is strongly asymmetric when the kinetic energy of the positron is of the order of $m_\mathrm{e}c^2$ [83]. Also, the direction of the higher-energy photon is strongly forward-directed with respect to the positron direction. When the kinetic energy of the positron is small compared with $m_\mathrm{e}c^2$, the energies of the photons are almost equal and they are emitted approximately isotropically in the opposite directions.

When the annihilation occurs with a bound atomic electron in a way that the nucleus obtains some momentum, a single photon can be emitted. For most elements and positron energies, the cross section of the one-photon annihilation per atom is substantially lower than the cross section of the free electron annihilation producing two photons. However, the one-photon cross section is proportional to $Z^5$ [84]. Therefore, it can be important for high-$Z$ elements when the cross section of the two-photon annihilation is small. The ratio of the one-photon to two-photon annihilation cross section per atom is largest in the MeV range, e.g., it amounts to about 17% for lead at about $T_\mathrm{p} = 3$ MeV [84].

A positron can also form an unstable bound state with an electron, called a positronium [84]. This system has two ground state configurations. In a singlet state, the spins of the electron and positron are antiparallel, whereas in a triplet state the spins are parallel. The most probable decay mode of the singlet state is into two photons, although the decay into any even number of photons is possible. The triplet state can decay into an odd number of photons with a minimum of three photons, which is also the most probable mode. The cross section for the three-photon decay is about

370 times smaller than the free electron annihilation cross section [83].

Based on the discussion above, we can ignore the rare one-photon and three-photon annihilation mechanisms, and simulate only the two-photon annihilation. Because the majority of the positrons annihilate at low energies, we can also ignore the in-flight annihilation, and assume that the annihilation occurs after the thermalization of the positron. The photons are then emitted isotropically in the opposite directions, both with an energy of $E_\mathrm{k} = m_\mathrm{e}c^2$. The small kinetic energy and momentum of the positron and the binding energy of the electron are ignored. Also, the vacancy generated in the annihilation is neglected because positrons annihilate predominantly with outer-shell electrons [85]. More detailed Monte Carlo annihilation models have also been presented (see, e.g., Ref. [86]) which could be used for applications such as positron emission tomography [87]. However, such applications are out of the scope of this work, and the simplified annihilation model should be sufficient for current purposes.

# 4   Atomic relaxation

When an electron is emitted from an atom as a result of the photoelectric effect or Compton scattering, a vacancy is left in the electron shell of the atom. The vacancy is filled by an electron dropping down from an upper shell, resulting in an emission of a photon or an electron. This often leads to a shower of photons and electrons as the new vacancies are also filled by electrons from higher shells. This process is called atomic relaxation, which needs to be modelled accurately because the generated photons transport energy away from the location of the relaxation cite.

A relaxation process resulting in the emission of a photon is called a radiative transition, or fluorescence when the time scale of the process is of the order of or less than $10^{-8}$ s [19]. A schematic of a radiative transition between the K- and $L_2$-shell is shown in Fig. 4.1. The energy of the fluorescence photon is given by

$$E_\mathrm{k} = E_{\mathrm{b},v} - E_{\mathrm{b},i}, \tag{4.1}$$

where $E_{\mathrm{b},v}$ is the binding energy of the vacancy shell and $E_{\mathrm{b},i}$ is the binding energy of the initial shell of the transition electron. Because each atom has a unique electronic structure, the emitted radiation is also called characteristic radiation. Due to quantum mechanical selection rules, not all transitions between shells are allowed. For example, the radiative transition between the K- and $L_1$-shell is forbidden.

Naturally, the highest energy fluorescence radiation is emitted in the K-shell transitions. The ratio of the transition energy $E_\mathrm{tr}$ and K-shell binding energy $E_{\mathrm{b,K}}$ is illustrated in Fig. 4.2a for $Z \geq 6$, showing the minimum, maximum and mean values. The mean ratio is always above 0.86, the minimum is above 0.81, and the maximum is close to unity. Therefore, when a radiative K-shell transition occurs, a substantial amount of the K-shell binding energy is given to a single fluorescence photon.

A vacancy in an electron shell can also be filled through a non-radiative transition which results in the emission of an electron from the atom. Three such transitions exist which are illustrated in Fig. 4.1. In the Auger transition, a vacancy is filled by an electron from a major upper shell, resulting in the emission of an electron from the same or higher shell. In the Coster–Kronig transition, a vacancy is filled by an electron from a higher subshell of the vacant primary shell, and an electron is emitted from a higher shell. The third possible transition type is the super Coster–Kronig transition, in which both the filling of the vacancy and the emission of the electron occur in the vacant primary shell. For simplicity, we call the electrons emitted in all three transitions Auger electrons. The kinetic energy of the Auger electron is given by

$$T_\mathrm{e} = E_{\mathrm{b},v} - E_{\mathrm{b},i} - E_{\mathrm{b},a}, \tag{4.2}$$

where $E_{\mathrm{b},a}$ is the binding energy of the shell from which the Auger electron is emitted. Non-radiative transitions do not have strict selection rules unlike radiative transitions, e.g., the non-radiative transition between the K- and $L_1$-shell is allowed. A non-radiative transition always generates two new vacancies in the electronic structure.
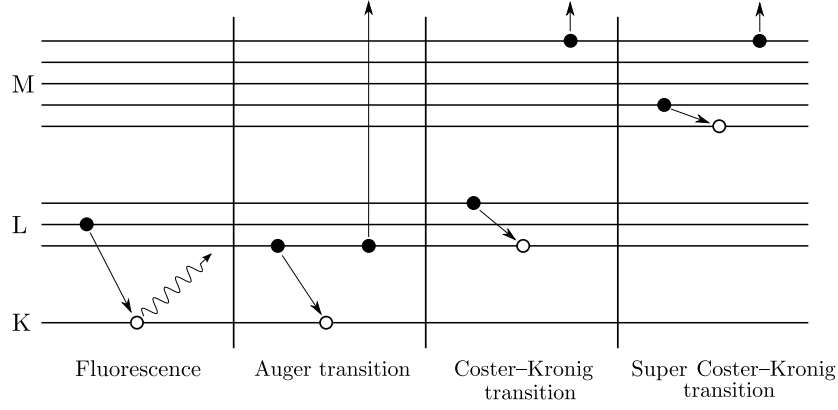
Figure 4.1: Schematics of radiative and non-radiative transitions occurring in atomic relaxation.
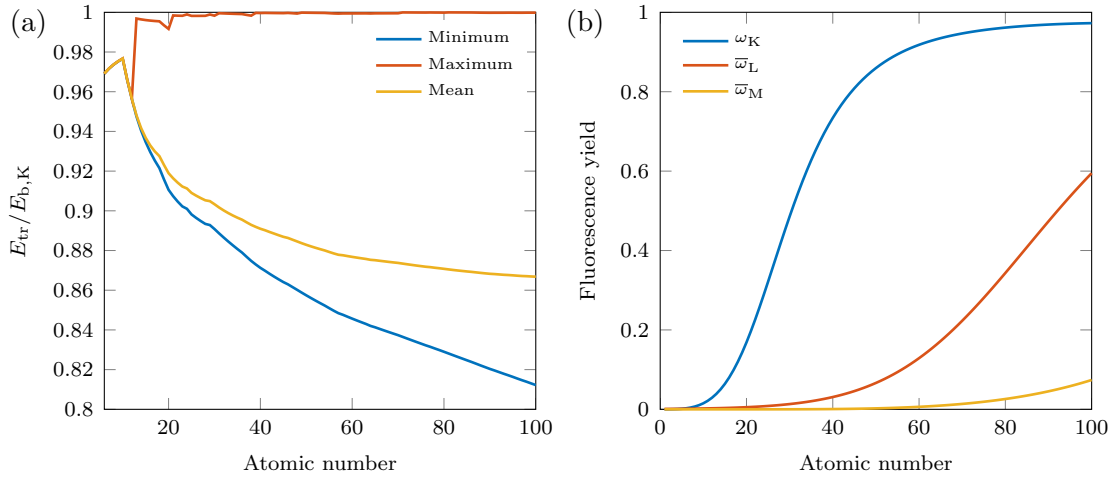


Figure 4.2: (a) Minimum, maximum, and mean radiative K-shell transition energy divided by the K-shell binding energy for $Z \geq 6$. The mean energy is the probability-weighted average of the possible radiative transition energies. Calculated from the data given in Ref. [88]. (b) Fluorescence yield for the K-shell and average fluorescence yields for the L- and M-shells according to Eqs. (4.3)–(4.6).

The transition probabilities depend strongly on the atomic number and the vacancy shell. The probability of a radiative transition is called a fluorescence yield $\omega$, which can be approximately calculated for the K-shell using the semi-empirical fit from Ref. [89]:

$$\omega_{\mathrm{K}} = \frac{\left(\sum_{i=0}^{3} C_i Z^i\right)^4}{1 + \left(\sum_{i=0}^{3} C_i Z^i\right)^4}, \tag{4.3}$$

where

$$
\begin{aligned}
C_0 &= 0.0370, & C_1 &= 0.03112, \\
C_2 &= 5.44 \times 10^{-5}, & C_3 &= -1.25 \times 10^{-6}. 
\end{aligned}
\tag{4.4}
$$

Eq. (4.3) can also be used for calculating the average L-shell fluorescence yield $\overline{\omega}_\mathrm{L}$ with the coefficients [89]

$$
\begin{aligned}
C_0 &= 0.177650, & C_1 &= 0.00298937, \\
C_2 &= 8.91297 \times 10^{-5}, & C_3 &= -2.67184 \times 10^{-7}.
\end{aligned}
\tag{4.5}
$$

The average M-shell fluorescence yield is approximately given by [89]

$$
\overline{\omega}_\mathrm{M} = 1.29 \times 10^{-9} \left(Z - 13\right)^4 .
\tag{4.6}
$$

The fluorescence yield for the K-shell and the average fluorescence yields for the L- and M-shells are presented in Fig. 4.2b. The probability of a radiative transition increases with $Z$, and decreases for increasing shell number. For example, the yield is above 0.5 for $Z \geq 31$ in the K-shell and $Z \geq 93$ in the L-shell. The K-shell yield becomes above 0.9 for $Z \geq 56$. The maximum average fluorescence is much smaller, about 0.6. Non-radiative transitions dominate for M- and higher shells in all elements.

The low-energy Auger electrons are relatively unimportant for the transport process, because their mean free paths are very small compared with fluorescence photons, and their bremsstrahlung yield is also very low. Therefore, most of the energy of Auger electrons is deposited close to the relaxed atom. On the other hand, fluorescence photons can deposit their energy far away from the location of the relaxed atom. In heavy elements, the photoelectric effect dominates below about 300–900 keV. At energies above the K-shell binding energy, 80% of photoelectric absorptions occur with the K-shell electrons [19]. Because radiative K-hell transitions dominate in heavy elements, and their mean energy is above 86% of the K-shell binding energy, a considerable portion of the binding energy is obtained by a single fluorescence photon on average.

Another important aspect of atomic relaxation is that in the energy region where the photoelectric effect dominates, fluorescence photons can have longer mean free paths than the original absorbed photons. This is due to the sharp decrease in the total cross section just below the binding energies. For example, in uranium the mean energy of the K-shell fluorescence photons is about 100 keV, at which the total cross section is about 760 b, whereas at the K-shell binding energy ($E_\mathrm{b,K} \approx 116$ keV) the total cross section is about 1900 b. In the energy range between 116 and 170 keV the total cross section is larger than at 100 keV.

The vacancies caused by Compton scattering are less important than the ones caused by the photoelectric effect because in Compton scattering, the interaction probability of a shell is approximately given by the number of electrons on the shell. Therefore, most of the Compton interactions occur with outer-shell electrons, resulting mostly in unimportant non-radiative transitions. Nevertheless, these vacancies are also treated with our relaxation model. Vacancies caused by triplet production and electron-positron annihilation should be unimportant and are therefore ignored. Also, vacancies generated when electrons and positrons collide with atomic electrons cannot be included, because the transport of charged particles is not modelled.

## 4.1   Simulation method

A comprehensive atomic relaxation database for $Z = 1$–$100$ is provided by the Evaluated Atomic Data Library (EADL) [88] which is compatible with the EPDL97 [20] and is also included in the ENDF/B-VII.1 [21]. EADL provides energies and probabilities for vast number of transitions. For example, the EADL lists almost 3,000 transitions for uranium. Although it has been pointed out that the EADL is out-of-date to some extent [24, 26, 28, 90], it is applied in many Monte Carlo codes [7, 10, 13]. Due to the comprehensive relaxation data and its accessibility through the ENDF/B-VII.1, it is also used in Serpent.

In order to sample the transition, a normalized CDF is created from the transition probabilities. The transition data is stored only for those shells which binding energies are larger than the cutoff energy $E_{\text{cut}}$. Due to non-radiative transitions, multiple vacancies can exist in the electronic structure. Therefore, the created vacancies are added to a queue and simulated in the inserted order. Also, the number of vacancies per each shell is tracked so that transitions from empty shells are not possible. At first, the initial vacancy is added to the queue. The following procedure is then repeated until the queue is empty:

(i) A new vacancy $j$ is selected from the queue and simulated only if $E_{\text{b},j} \geq E_{\text{cut}}$. Else, this step is repeated.

(ii) A transition is sampled according to the generated CDF. If the transition shell or the shell of the Auger electron is already empty, this step is repeated.

(iii) If the transition energy $E_{\text{tr},j}$ is above $E_{\text{cut}}$, a fluorescence photon or an Auger electron is created. The direction of the particle is sampled isotropically. TTB approximation is used for the Auger electron.

(iv) In the case of a radiative transition, a single vacancy is added to the queue. In the case of a non-radiative transition, two vacancies are added.

Note that any effects of multiple vacancies on the transitions are not taken into account. The Walker's alias method [16] is used for sampling the transition in step (ii) which requires only a single comparison.

After all vacancies have been treated, the locally deposited energy in the atomic relaxation process is calculated as

$$E_{\text{dep,AR}} = E_{\text{b},v} - \sum_{j,E_{\text{tr},j} \geq E_{\text{cut}}} E_{\text{tr},j} + \sum_{k,E_{\text{tr},k} \geq E_{\text{cut}}} E_{\text{dep,TTB},k}, \qquad (4.7)$$

where $E_{\text{b},v}$ is the binding energy of the initial vacancy shell and $E_{\text{dep,TTB},k}$ is the locally deposited energy in the TTB process used for the Auger electron (Eq. (5.23)). The summation index $k$ is over the non-radiative transitions.

# 5   Electron interactions

As discussed in the previous sections, electrons are emitted in three photoatomic interactions: photoelectric effect, Compton scattering, and pair production which also creates positrons. Also, low-energy electrons are emitted through non-radiative transitions of atomic relaxation. These electrons travel in the medium and lose their energy through interactions with atomic electrons and nuclei, which often lead into emission of new electrons and photons. The challenge in the modelling of electron transport is that the number of interactions the projectile electron undergoes is usually very large. Special simulation methods are therefore required in order to perform a transport calculation in a reasonable amount of time while retaining the accuracy. In photon transport applications, such as gamma heating in nuclear reactors, electron transport can usually be neglected because electrons lose their energy in much shorter distances than the high-energy photons. However, high-energy electrons emit photons in the form of bremsstrahlung radiation, which means that the electron energy is actually deposited over a greater distance than the electron range would imply. To take into account the bremsstrahlung radiation, a so-called thick-target bremsstrahlung approximation is applied in this work.

In this section, a short introduction to electron interactions is first given. The important concepts of electron stopping power and the continuous slowing down approximation are then discussed before presenting a method for the thick-target bremsstrahlung.

## 5.1   Elastic and inelastic scattering

The interactions between energetic free electrons and matter can be divided into three categories: elastic scattering, inelastic scattering, and bremsstrahlung. The angular deflection of the projectile electron is mainly determined by elastic scattering, while the energy loss is caused by inelastic scattering at low energies and by bremsstrahlung at high energies. Also, an electron can lose its energy due to Cherenkov radiation which occurs when the electron velocity is greater than the phase velocity of light in the medium. However, the energy loss due to Cherenkov radiation is negligible [19]. The main features of elastic and inelastic scattering interactions are briefly discussed here.

When an electron or positron scatters elastically form an atom, its direction is changed without the loss of energy. The atomic cross section of elastic scattering is highest at low energies, and decreases with increasing energy before saturating to a constant value. Elastic scattering is highly peaked in the forward direction, especially at high energies. When simulating elastic scattering, it is inefficient to calculate all the small-angle scattering interactions individually. Therefore, different multiple scattering theories have been developed in order to take into account a large number of small-angle scattering events. The multiple-scattering approach is often

used in Monte Carlo electron transport codes for estimating the angular deflection of the electron over a suitable path length. [19]

In inelastic scattering, the projectile electron loses part of its energy either through excitation or ionization. In excitation, the incident electron interacts with an atomic electron which is raised to a higher energy level, whereas in ionization an atomic electron is emitted from the atom. Also, fluorescence photons and Auger electrons are generated through atomic relaxation as the created vacancy is filled by other electrons. Below 1 MeV, the atomic cross section of excitation is typically twice of that of ionization, whereas above 1 MeV they are comparable. However, the mean energy loss per interaction is much higher for ionization than for excitation, and the mean energy loss per travelled distance is dominated by ionization over excitation above 1 keV or so. The energy losses through ionization and excitation events are together referred to as collision energy losses. [19]

## 5.2   Bremsstrahlung

Bremsstrahlung is the breaking radiation emitted when a charged particle is accelerated by the electric field of a nucleus or an electron. In a bremsstrahlung interaction, a photon with an energy of $E_k$ is emitted while the kinetic energy $T$ and the direction of the charged particle are changed. Bremsstrahlung is important for light charged particles, i.e. electrons and positrons, but not for heavy charged particles, such as protons and alpha particles. The energy loss of a charged particle by bremsstrahlung is referred to as a radiative energy loss, which dominates over collision losses at high energies, especially in high-$Z$ elements.

A bremsstrahlung interaction is characterized by a cross section differential in photon energy and in photon and electron emission angles. However, in Monte Carlo transport codes, a single differential cross section with respect to the photon energy is usually applied for sampling the photon energy. The angular distribution of the photon is considered separately whereas the change in the electron direction is assumed to be accounted for by the elastic scattering distribution [7]. The cross section differential in energy cannot be expressed accurately in analytical form for all energies. Different approaches and results have been combined by Seltzer and Berger [91, 92], whose extensive tabulations are often used for describing the bremsstrahlung energy distribution of electrons.

The differential cross section for bremsstrahlung is often expressed in the form of [93]

$$\frac{d\sigma_{\mathrm{br}}}{dE_{\mathrm{k}}} = \frac{Z^2}{\beta^2}\frac{1}{E_{\mathrm{k}}}\chi(Z, T, \kappa), \tag{5.1}$$

where $\beta$ is given by Eq. (3.12), $\kappa = E_{\mathrm{k}}/T$ is the reduced photon energy, and $\chi(Z, T, \kappa)$ is the scaled bremsstrahlung cross section defined as

$$\chi(Z, T, \kappa) = \frac{\beta^2}{Z^2}E_{\mathrm{k}}\frac{d\sigma_{\mathrm{br}}}{dE_{\mathrm{k}}}. \tag{5.2}$$
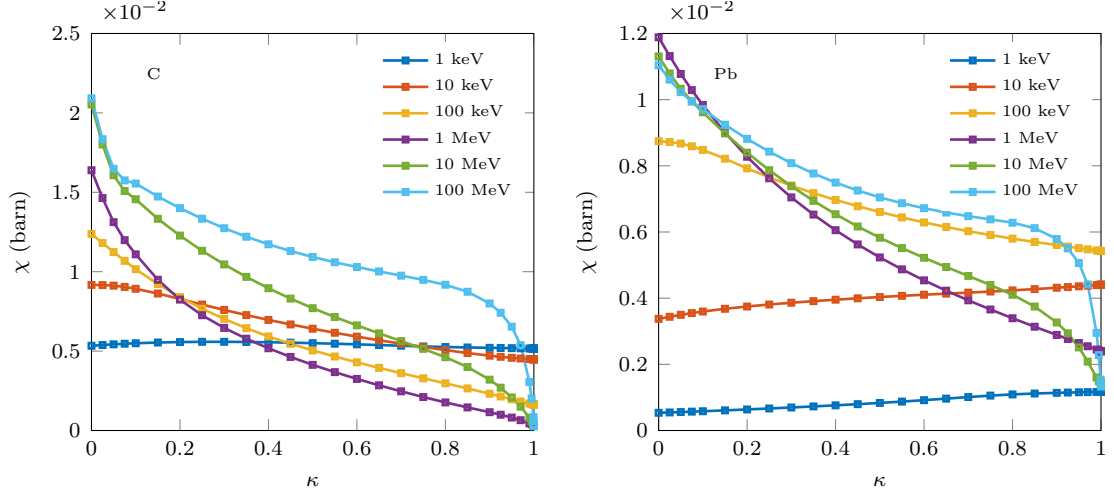
Figure 5.1: Scaled bremsstrahlung DCS as a function of the variable $\kappa = E_k/T$ in carbon and lead for different electron kinetic energies according to Ref. [92].

The scaled bremsstrahlung cross section given by Seltzer and Berger [92] is shown in Fig. 5.1 for carbon and lead at electron kinetic energies between 1 keV and 100 MeV.

The bremsstrahlung cross section is different for positrons than electrons, which is due to the fact that electrons are attracted whereas positrons are repulsed by the nucleus. The positron bremsstrahlung cross section is smaller, especially at low and intermediate energies. At high energies, the positron bremsstrahlung DCS approaches the electron DCS. No comprehensive and detailed calculations on positron bremsstrahlung have been performed, as far as the author knows. Nevertheless, some results have been published [94, 95]. In PENELOPE [7], positron DCS is calculated by multiplying Eq. (5.1) by a factor

$$
\begin{aligned}
R_p\left(Z, T\right) = {}& 1 - \exp\left(-1.2359 \times 10^{-1} t + 6.1274 \times 10^{-2} t^2 - 3.1516 \times 10^{-2} t^3\right. \\
& \left. + 7.7446 \times 10^{-3} t^4 - 1.0595 \times 10^{-3} t^5 + 7.0568 \times 10^{-5} t^6 \right. \\
& \left. - 1.8080 \times 10^{-6} t^7\right),
\end{aligned}
\tag{5.3}
$$

where the variable $t$ is defined as

$$
t = \ln\left(1 + \frac{10^6}{Z^2} \frac{T}{m_e c^2}\right).
\tag{5.4}
$$

Note that the factor $R_p$ is independent of the photon energy $E_k$, and therefore it only scales the scaled bremsstrahlung DCS. The reported accuracy of this factor is about 0.5% when compared to calculations of Ref. [95].

## 5.3 Stopping powers

An important quantity in electron transport calculations is the stopping power which gives the average energy loss per unit path length. It is defined as

$$-\frac{dT}{ds} = n \int W \frac{d\sigma}{dW} dW \equiv S(T), \qquad (5.5)$$

where $n$ is the number density of target atoms in the medium and $d\sigma/dW$ is the differential cross section for the energy loss $W$. When referring to collision energy losses through ionization and excitation, the collision stopping power $S_{\text{col}}$ is used. Likewise, the radiative stopping power $S_{\text{rad}}$ is used when referring to energy loss through bremsstrahlung. The total stopping power is the sum of these two, i.e.

$$S_{\text{tot}}(T) = S_{\text{col}}(T) + S_{\text{rad}}(T). \qquad (5.6)$$

The stopping power is often divided by the material density $\rho$, in which case it is called the mass stopping power and is denoted as $S/\rho$.

A collision stopping power formula for projectile electrons with energies much higher than those of atomic electrons was derived by Bethe [96, 97]. Using the notation of Ref. [98], the mass collision stopping power is expressed as

$$\frac{1}{\rho} S_{\text{col}}(T) = \frac{2\pi r_{\text{e}}^2 m_{\text{e}} c^2}{\beta^2} N_A \frac{Z}{A_{\text{M}}} \left[ \ln (T/I)^2 + \ln (1 + \tau/2) + F(\tau) - \delta_F(T) \right], \quad (5.7)$$

where $\tau = T/m_{\text{e}}$, $I$ is the mean excitation energy, and $\delta_F(T)$ is the density effect correction. In the case of electrons, the function $F(\tau)$ is given by

$$F_{\text{e}}(\tau) = \left( 1 - \beta^2 \right) \left[ 1 + \tau^2/8 - (2\tau + 1) \ln 2 \right], \qquad (5.8)$$

whereas for positrons $F(\tau)$ takes the form

$$F_{\text{p}}(\tau) = 2 \ln 2 - \left( \beta^2/12 \right) \left[ 23 + 14/(\tau + 2) + 10/(\tau + 2)^2 + 4/(\tau + 2)^3 \right]. \qquad (5.9)$$

There are two reasons why the collision stopping power differs for positrons. The first one is that large energy losses of electrons are treated with the Møller cross section, whereas the Bhabha cross section is used for positrons [98]. The second one is that in the final state of an electron-electron interaction, the projectile and target electrons are indistinguishable, and the fastest one is set as a primary electron by convention. On the other hand, the projectile positron is distinguishable from the target electron. Therefore, an electron can lose at most half of its energy in a single interaction, whereas a positron can lose all of it.

The two non-trivial variables in the collision stopping power formula are $I$ and $\delta_F$. The mean excitation energy $I$ is a material constant that describes the energy transfer from a charged particle to the target atom. In general, $I$ cannot be accurately calculated theoretically, but must be determined experimentally [98]. Not only does

the mean excitation energy enter Eq. (5.7) through the logarithmic term $2\ln I$, but also through the density effect correction $\delta_F$. The logarithmic term dominates at low energies, whereas at very high energies, Eq. (5.7) becomes independent of $I$ and depends only on the electron density of the medium [98].

The density effect correction $\delta_F(T)$ is needed for taking into account the polarization of the medium by the electric field of the projectile electron. The polarization of the atoms results in an electric field which suppresses the electric field of the electron, and therefore reduces the collision stopping power. The number of polarized atoms in the electron path depends on the material density, and hence the phenomenon is called the density effect. The effect is important especially at high energies when the polarization caused by the electron is stronger. The evaluation of $\delta_F$ is not trivial and requires experimental input data [98]. However, $\delta_F$ can be approximated with Sternheimer's theory [99] in which $\delta_F$ depends on the mean excitation energy $I$, material density, the number of conduction electrons, and the binding energies of the target atom. A method for solving $\delta_F$ is described in Ref. [100].

The radiative stopping power for electrons is obtained by inserting Eq. (5.1) into Eq. (5.5), which gives

$$S_{\text{rad}}(T) = n\frac{Z^2}{\beta^2} \int_0^T \chi(Z, T, \kappa)dE_{\text{k}} = n\frac{Z^2}{\beta^2}T \int_0^1 \chi(Z, T, \kappa)d\kappa, \qquad (5.10)$$

where a change of variables has been made. In the case of positrons, Eq. (5.10) is multiplied by the factor $R_{\text{p}}$ given by Eq. (5.3). At very high energies, the radiative stopping power is approximately given by

$$S_{\text{rad}}(T) = \frac{T}{X_0}, \qquad (5.11)$$

where $X_0$ is called the radiation length, which gives the mean distance at which the electron energy decreases to $1/e$ of its initial value. The radiation length is the same for positrons and electrons because at high energies the positron bremsstrahlung DCS approaches the electron DCS.

The radiative and collision mass stopping powers of electrons are shown in Fig. 5.2 for carbon, iron, silver, and uranium. At low and intermediate energies, collision energy losses dominate over radiative losses. The radiative stopping power exceeds the collision stopping power between about 10 and 100 MeV in the shown elements, and radiative losses dominate from there on. Note that the uncertainties of the plotted collision stopping powers may be large below 10 keV [101].

### 5.3.1 Treatment of compounds and mixtures

In the case of photon transport, the treatment of compounds and mixtures is straightforward, as the target atom is sampled based on the macroscopic cross sections as was discussed in Sec. 2.3.2. However, this so-called free-atom model is not
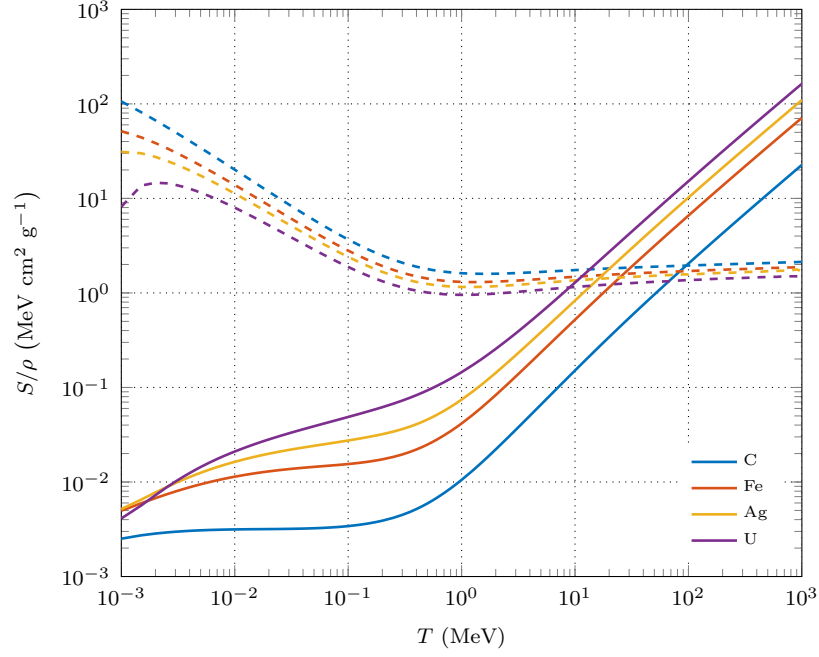
Figure 5.2: Mass stopping powers $S/\rho$ of electrons in carbon, iron, silver, and uranium. The solid lines represent the radiative stopping powers $S_{\mathrm{rad}}/\rho$ while the dashed lines represent the collision stopping powers $S_{\mathrm{col}}/\rho$. The stopping power data is from the ESTAR database provided by National Institute of Standards and Technology (NIST) [101].

always valid in the case of electron transport, as molecular binding and the phase of the matter can have large effects on the cross sections. Here, we shortly discuss how compound materials can be treated.

To calculate a cross section for a molecule, Bragg's additivity rule is commonly used, which states that the molecular cross section is equal to the sum of the cross sections of the atoms in the molecule. This is equivalent to the free-atom model. It is often used for approximating the bremsstrahlung cross section and the radiative stopping power. According to the additivity rule, the bremsstrahlung DCS is given by

$$\frac{d\sigma_{\mathrm{br}}}{dE_{\mathrm{k}}} = \frac{1}{\beta^2 E_{\mathrm{k}}} \sum_j \gamma_j Z_j^2 \chi(Z_j, T, \kappa), \tag{5.12}$$

where $Z_j$ is the atomic number and $\gamma_j$ is the atomic fraction of the $j$th constituent element. Note that in the actual molecular DCS the atomic fractions are replaced by the numbers of each type of atom in the molecule. Inserting Eq. (5.12) into the radiative stopping power equation (5.10) yields

$$S_{\mathrm{rad}}(T) = n_{\mathrm{tot}} \frac{T}{\beta^2} \sum_j \gamma_j Z_j^2 \int_0^1 \chi(Z_j, T, \kappa) d\kappa, \tag{5.13}$$

where $n_{\mathrm{tot}}$ is the total number density of atoms in the material. Because the number

density of the $j$th constituent atoms is $n_j = \gamma_j n_{\text{tot}}$, and $n_j$ is given by

$$n_j = \frac{N_{\text{A}}\rho}{A_j} w_j, \tag{5.14}$$

where $A_j$ is the atomic weight and $w_j$ is the mass fraction related to the $j$th constituent element, Eq. (5.13) can be written as

$$\frac{1}{\rho} S_{\text{rad}}(T) = \sum_j w_j \left[ \frac{1}{\rho} S_{\text{rad}}(T) \right]_j, \tag{5.15}$$

where $\left[ \frac{1}{\rho} S_{\text{rad}}(T) \right]_j$ is the mass radiative stopping power of the $j$th constituent element.

The Bragg's additivity rule cannot be accurately used for calculating the collision stopping power. The reason is that the mean excitation energies $I$ and especially the density effect corrections $\delta_F$ of the constituents cannot be simply summed together. Experimental results are often used for the mean excitation energy, and the density effect correction must be solved for the material [100]. Another complicating factor is that $I$ and $\delta_F$ depend on the phase of the matter and types of chemical bonds present in the molecules [98].

## 5.4   Continuous slowing down approximation

In the continuous slowing down approximation (CSDA), the projectile particle loses its energy in a continuous manner at a rate given by the total stopping power, i.e. the stopping power is treated as a derivative [98]. The CSDA results in average values, which can be used for simple estimations of how electrons slow down in a medium. The statistical fluctuations around the average values are disregarded. The CSDA is used as the basis for the thick-target bremsstrahlung approximation.

One useful CSDA quantity is the CSDA range $R_{\text{CSDA}}(T)$, which is the average path length the charged particle travels when it slows down to rest. It is simply given by

$$R_{\text{CSDA}}(T) = \int \left( \frac{dT'}{ds} \right)_{\text{tot}}^{-1} dT' = \int_0^T \frac{1}{S_{\text{tot}}(T')} dT'. \tag{5.16}$$

The CSDA range can be used for crude estimation of the penetration depth of charged particles. In Fig. 5.3, the CSDA ranges are shown for electrons in aluminium, iron, and uranium between 10 keV and 1 GeV. Also, the photon mean free paths are plotted for comparison. The CSDA ranges are much smaller than the mean free paths, except at high energies. The differences are larger in lighter elements.

Another important quantity is the radiative yield $Y_{\text{rad}}(T)$, which is the fraction of the charged particle's kinetic energy emitted as bremsstrahlung radiation as it slows
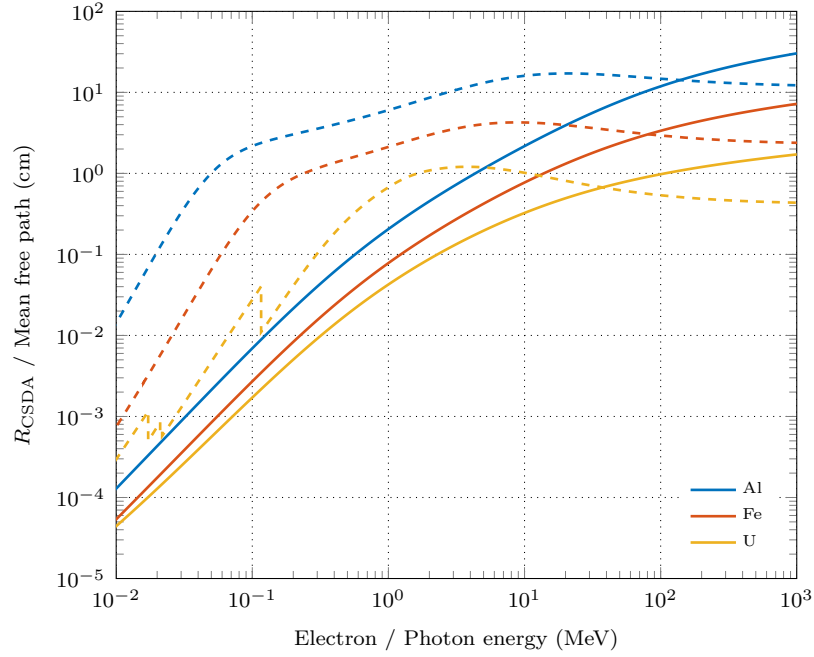
Figure 5.3: Electron CSDA range as a function of the electron kinetic energy and photon mean free path as a function of the photon energy in aluminium, iron, and uranium. The CSDA ranges were calculated using the stopping powers given by the ESTAR database [101]. The mean free paths were calculated using the cross section data of the EPDL97 [20].

down to rest. The energy emitted as a bremsstrahlung is given by

$$E_{\rm rad}(T) = \int_0^{R_{\rm CSDA}(T)} \left(\frac{dT'}{ds}\right)_{\rm rad} ds = \int_0^T \left(\frac{dT'}{ds}\right)_{\rm rad} \left(\frac{dT'}{ds}\right)_{\rm tot}^{-1} dT'$$
$$= \int_0^T \frac{S_{\rm rad}(T')}{S_{\rm tot}(T')} dT'. \tag{5.17}$$

Thus, the radiative yield is given by

$$Y_{\rm rad}(T) = \frac{E_{\rm rad}(T)}{T} = \frac{1}{T} \int_0^T \frac{S_{\rm rad}(T')}{S_{\rm tot}(T')} dT'. \tag{5.18}$$

Radiative yields of electrons and positrons are shown in Fig. 5.4 for carbon, iron, silver, and uranium. The yield is small at low energies where collision energy losses dominate, but approaches unity at high energies. The radiative yield is much higher for high-$Z$ elements except at very high energies. For example, the electron radiative yield at 1 MeV is about 8% in uranium, whereas it is 0.3% in carbon. The radiative yield of positrons is lower than that of electrons, especially in heavy elements. At 1 MeV in uranium, the positron radiative yield is about 3%. At high energies, the positron radiative yield approaches the electron radiative yield because the positron bremsstrahlung DCS approaches the electron DCS.

The average number of bremsstrahlung photons emitted per unit path length is given
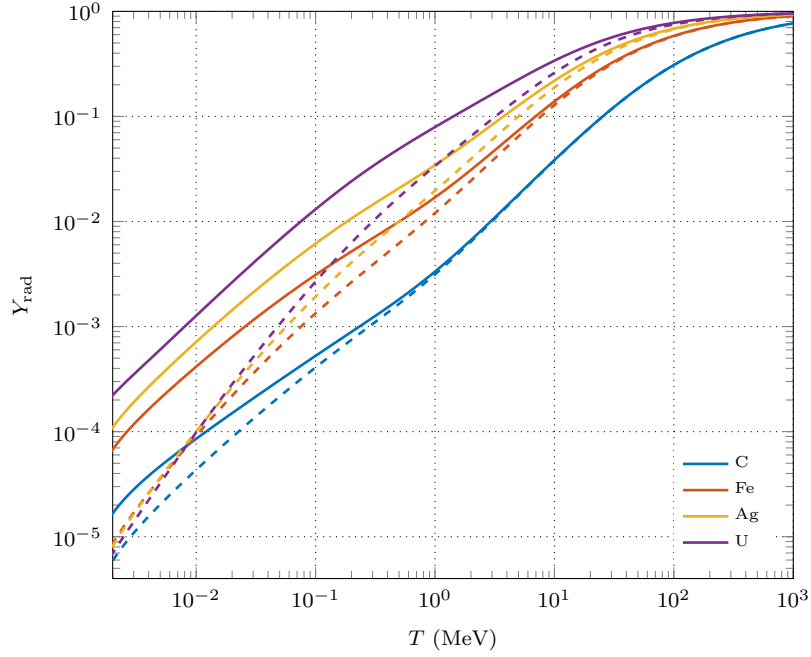
Figure 5.4: Radiative yield $Y_{\mathrm{rad}}$ of electrons (solid lines) and positrons (dashed lines) in carbon, iron, silver, and uranium. The yields were calculated using the stopping powers given by the ESTAR database [101]. In the case of positrons, the radiative stopping powers were multiplied by the factor $R_{\mathrm{p}}$ given by Eq. (5.3), but the collision stopping powers were the same as for electrons.

by the inverse of the bremsstrahlung mean free path, which is calculated as

$$\lambda_{\mathrm{br}}^{-1}(T, E_{\mathrm{cut}}) = n\sigma_{\mathrm{br}} = n\int_{E_{\mathrm{cut}}}^{T} \frac{d\sigma_{\mathrm{br}}}{dE_{\mathrm{k}}}dE_{\mathrm{k}} = n\frac{Z^2}{\beta^2}\int_{\kappa_{\mathrm{cut}}}^{1} \frac{1}{\kappa}\chi(Z, T, \kappa)d\kappa, \qquad (5.19)$$

where $\kappa_{\mathrm{cut}} = E_{\mathrm{cut}}/T$. Note that the lower limit of the integral is set to non-zero value $E_{\mathrm{cut}}$ because the DCS given by Eq. (5.1) diverges when $E_{\mathrm{k}} \to 0$. The inverse mean free path can be used for calculating the photon number yield $Y_{\mathrm{n}}(T, E_{\mathrm{cut}})$, which is here defined as the average number of bremsstrahlung photons with energies higher than $E_{\mathrm{cut}}$ emitted by a charged particle as it slows down to the energy $E_{\mathrm{cut}}$. It is given by

$$Y_{\mathrm{n}}(T, E_{\mathrm{cut}}) = \int_{R_{\mathrm{CSDA}}(E_{\mathrm{cut}})}^{R_{\mathrm{CSDA}}(T)} \lambda_{\mathrm{br}}^{-1}(T', E_{\mathrm{cut}})ds = \int_{E_{\mathrm{cut}}}^{T} \frac{\lambda_{\mathrm{br}}^{-1}(T', E_{\mathrm{cut}})}{S_{\mathrm{tot}}(T')}dT'. \qquad (5.20)$$

The photon number yield of electrons and positrons is shown in Fig. 5.5 in carbon and lead for different values of $E_{\mathrm{cut}}$. The number yield is clearly greater in heavier elements. For example, the number yield at 10 MeV is about 1.3 in carbon while it is about 10 in lead. Also, the number yield of electrons is greater than that of positrons, particularly in high-$Z$ elements.

The photon number yield can be used for forming the energy spectrum of bremsstrahlung photons emitted by a charged particle. The number of photons with energies
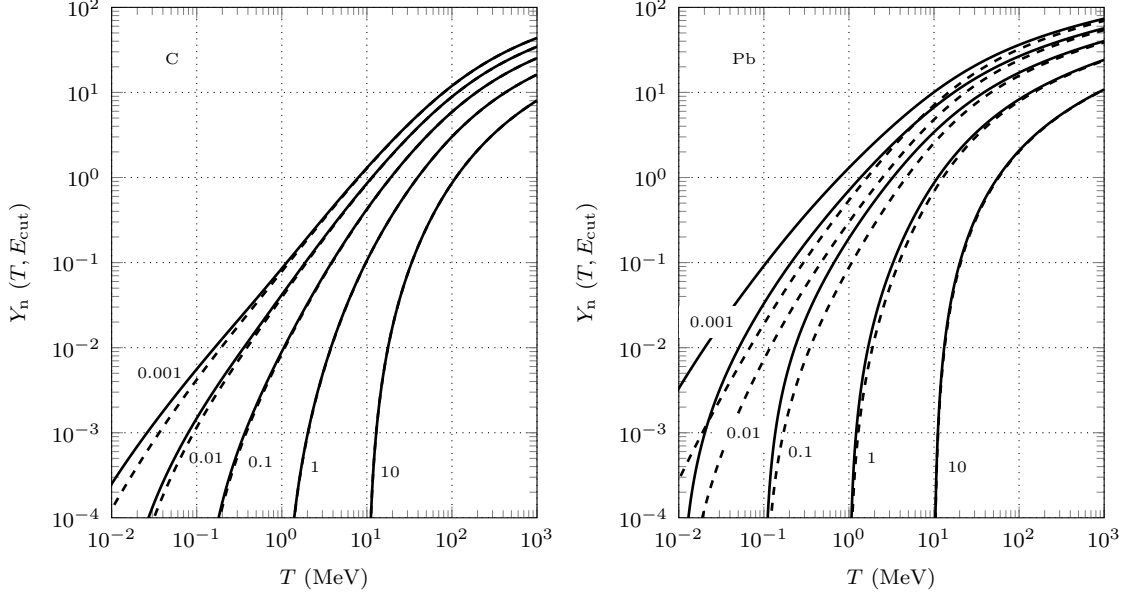
Figure 5.5: Photon number yields $Y_{\mathrm{n}}(T, E_{\mathrm{cut}})$ of electrons (solid lines) and positrons (dashed lines) in carbon and lead for the cutoff energies $E_{\mathrm{cut}}$ of 0.001, 0.01, 0.1, 1, and 10 MeV as indicated in the figure. The number yields were integrated from the scaled bremsstrahlung DCS data of Ref. [92] and stopping powers given by the ESTAR database [101]. Positron stopping powers were calculated as described in the caption of Fig. 5.4.

between $E_1$ and $E_2$ is given by $Y_{\mathrm{n}}(T, E_1) - Y_{\mathrm{n}}(T, E_2)$, assuming that $E_1 > E_2 > E_{\mathrm{cut}}$. Also, the photon number yield can be used for calculating the number of photons with energies higher than $E_{\mathrm{cut}}$ emitted by an electron as it slows down from an energy $T_1$ to $T_2$. This is given by $Y_{\mathrm{n}}(T_1, E_{\mathrm{cut}}) - Y_{\mathrm{n}}(T_2, E_{\mathrm{cut}})$.

## 5.5   Thick-target bremsstrahlung approximation

As already discussed in this section, high-energy electrons and positrons lose their energy mainly through radiative losses as they slow down. Combining this with the fact that bremsstrahlung photons can travel much greater distances than the charged particle itself, bremsstrahlung must be taken into account for high-energy electrons and positrons. A rather straightforward way to include the emission of bremsstrahlung photons is to use a thick-target bremsstrahlung approximation. Thick-target bremsstrahlung essentially means that the charged particle is assumed to lose all of its energy in a single homogeneous material region. The quantities of interest are the number of photons emitted by the charged particle, and the energy spectrum of the photons as the particle slows down below the cutoff energy $E_{\mathrm{cut}}$. These quantities can be calculated using the CSDA as discussed in the previous section.

The TTB approximation presented here involves some approximations which introduce errors to the angular distribution of bremsstrahlung radiation. First of all,

bremsstrahlung photons are assumed to be emitted at the same location where the charged particle was created. Hence, the range of the particle is omitted entirely. The introduced error should be small when the energy of the charged particle is not too high and the range is short. Secondly, because the transport of charged particles is omitted entirely, the direction of the particle when the bremsstrahlung emission occurs is ignored. Thirdly, the emission direction of the bremsstrahlung photon itself is ignored. Therefore, the direction of the bremsstrahlung photon is approximated to be equal to the direction of the incident charged particle. This should be a reasonable approximation at high electron energies, because then most bremsstrahlung photons are emitted at small angles [19].

### 5.5.1   Simulation method

The data needed for simulating thick-target bremsstrahlung consists of the scaled bremsstrahlung DCSs and the radiative and collision stopping powers. The scaled bremsstrahlung DCS data given by Seltzer and Berger [92] were read from the PENE-LOPE data files included in Geant4 [13]. In this data set, the scaled bremsstrahlung DCS $\chi(Z, T, \kappa)$ is tabulated for $Z = 1$–$99$ for a set of electron energies $T$ ranging between 1 keV and 10 GeV. The $T$ grid is dense enough to use cubic spline log-log interpolation [7]. For each $T$ value, $\chi(Z, T, \kappa)$ is given for a set of 32 reduced photon energies $\kappa$.

The radiative and collision stopping powers were read from the ESTAR database provided by NIST [101]. For compounds and mixtures, we calculate the radiative stopping powers with the Bragg's additivity rule, Eq. (5.15). The collision stopping powers for compounds are also calculated with the Bragg's additivity rule, and the density effect correction is ignored. Note that this is not a good approximation as was discussed in Sec. 5.3.1, and this should be fixed in the future. The Bragg's additivity rule fails especially when a higher-density compound consists of elements that are in low-density gaseous form in normal temperature and pressure, at which the collision stopping powers of NIST are given.

As noted in the previous sections, the bremsstrahlung DCS and both the radiative and collision stopping powers for positrons differ from those of electrons. The positron factor $R_{\mathrm{p}}(Z, T)$ given by Eq. (5.3) is taken into account for the scaled bremsstrahlung DCS and radiative stopping powers. However, the difference between collision stopping powers of electrons and positrons is omitted, and the collision stopping powers of electrons are used for positrons as well. Therefore, the current method for treating positrons is incomplete. Also, the positron bremsstrahlung method has not been tested thoroughly, and therefore an option for treating positrons as electrons is included.

In order to sample the number and the energies of bremsstrahlung photons, the photon number yield $Y_{\mathrm{n}}(T, E_{\mathrm{cut}})$ must be calculated for a set of electron kinetic energies $T_i$ and cutoff energies $E_{\mathrm{cut},j}$. The same logarithmic energy grid consisting of

200 values between 1 keV and 100 MeV is used for both $T_i$ and $E_{\text{cut},j}$, which from now on is denoted as $T_i$. The first step is to calculate the total stopping powers and the scaled bremsstrahlung DCSs for the given material as specified above. Both of them are then interpolated at the $T_i$ grid using cubic spline log-log interpolation. The inverse mean free path given by Eq. (5.19) is integrated using trapezoidal rule on log-log scale for a set of $\kappa_{\text{cut},i}$ values corresponding to the $T_i$ grid. Photon number yields given by Eq. (5.20) are calculated using cubic spline integration on a linear scale. Thick-target bremsstrahlung energy PDF and CDF are then calculated.

The first step in the TTB sampling method is to calculate the number of emitted bremsstrahlung photons. For an electron or a positron with an energy $T$, the photon number yield $Y_{\text{n}}(T, E_{\text{cut}})$ is computed using linear interpolation on a log-log scale. The number of photons is then given by

$$N_{\text{ph}} = \lfloor Y_{\text{n}}(T, E_{\text{cut}}) + \xi \rfloor, \tag{5.21}$$

where $E_{\text{cut}}$ now has the value of 1 keV, $\xi \sim unif(0, 1)$, and $\lfloor \cdot \rfloor$ denotes the floor function. To sample the photon energies, one would have to interpolate the energy distribution between the tabulated values at indexes $k$ and $k + 1$ for which $T_k < T < T_{k+1}$ holds. This is computationally expensive, especially if logarithmic interpolation is used. An alternative method is to use the composition technique described in Sec. 2.2.4. Using linear interpolation on logarithmic scale, the energy grid is sampled using the probabilities of the indexes $k$ and $k + 1$, which are given by

$$\text{P}_k = \frac{\ln T_{k+1} - \ln T}{\ln T_{k+1} - \ln T_k}, \quad \text{P}_{k+1} = \frac{\ln T - \ln T_k}{\ln T_{k+1} - \ln T_k}. \tag{5.22}$$

If the index $k + 1$ is selected, the maximum of the bremsstrahlung energy CDF is interpolated at the energy $T$. Note that when the index $k$ is selected, the maximum photon energy will be lower than $T$. Photon energies are sampled from the tabulated distribution corresponding to the sampled index as described in Sec. 2.2.3, assuming linear interpolation on a linear scale and using the unnormalized PDF and CDF.

The locally deposited energy in the TTB process is calculated as

$$E_{\text{dep,TTB}} = T - \sum_j E_{\text{k},j}, \tag{5.23}$$

where the summation is over the emitted bremsstrahlung photons. If no bremsstrahlung photons are created, $E_{\text{dep,TTB}}$ is equal to $T$.

### 5.5.2   Known limitations and future development

The TTB model presented here cannot be considered fully complete and has some limitations. Due to the large amount of work required for the other parts of this thesis, the TTB model was left with less attention. Also, an adequate description of the implementation of the TTB approximation was not found in the literature, which complicated the development of the model.

One issue in the described TTB sampling method is that the sum of the sampled photon energies can be larger than the electron energy. This occurs mainly at high electron energies when the radiation yield is high. For example, the sum exceeds the electron energy in about 2.7% of the cases for 10 MeV electrons in uranium, and in about 18% of the cases for 50 MeV electrons. When modelling bremsstrahlung, it is important that the radiative yield and the energy distribution of photons are correct. In order to preserve the conservation of energy with the correct radiative yield and energy distribution, the number of photons should be sampled differently than described.

Another detected problem is that radiative yields obtained with the TTB sampling method differ slightly from the ones calculated with Eq. (5.18). For example, the radiative yield given by the TTB sampling method is about 0.7% lower for 1 and 10 MeV electrons in uranium, while about 0.2% higher for 100 MeV electrons. This may indicate a problem in the chosen interpolation methods. The radiative yields calculated with Eq. (5.18) were tested to be correct by comparing them to the values given by the ESTAR database [101].

In the future, the collision stopping powers should be solved for the given density and material composition instead of using the Bragg's additivity rule. The implemented positron bremsstrahlung model should be tested in comparison with Monte Carlo transport codes that also model positron bremsstrahlung. The used interpolation and integration methods are to be reviewed. The possibility of implementing an angular distribution model for bremsstrahlung photons should also be studied.

# 6 Comparison between Serpent and MCNP6

In this section, the photon physics model implemented in Serpent is tested and also compared with MCNP6 [10]. MCNP6 is a general-purpose Monte Carlo transport code for neutron, photon, electron and other charged particle calculations, and is used in a wide range of applications. Of all the available general-purpose Monte Carlo codes, MCNP6 was selected primarily because it also includes the thick-target bremsstrahlung approximation. Comparison with other Monte Carlo codes using coupled photon–electron transport would have been too extensive task for this thesis. Also, the validation with respect to experimental results and benchmark problems is left for future research.

Two test cases are used here for comparing Serpent and MCNP6: a monoenergetic point source in an infinite geometry for studying the energy spectrum of photons, and a monoenergetic photon beam inside a cylinder for investigating the energy-angular distribution. All the calculations were carried out with the development version of Serpent 2.1.24 and the pre-compiled executable of MCNP6.1. The default photon physics options and the eprdata12 library were used in MCNP6. In Serpent calculations, total interaction cross sections were also read from the eprdata12 library. Most of the interaction data applied in Serpent were extracted from the ENDF/B-VII.1 [21] as specified in Secs. 3 and 4. Compton profiles were read from the ESRF's DABAX library [102], electron stopping powers from the ESTAR database provided by NIST [101], and the scaled bremsstrahlung DCS data from the PENELOPE data files included in Geant4 [13]. The processing of the interaction data is done in Serpent before the beginning of the transport simulation.

## 6.1 Differences in photon physics

MCNP6 introduces several enhancements related to the photon transport physics compared to previous releases [103], including improved presentation of form factors and incoherent scattering functions, subshell-specific photoelectric data, and detailed modelling of atomic relaxation. These and many other modelled phenomena are based on similar approaches in Serpent and MCNP6. However, the physics routines implemented in Serpent are not based on the ones used in MCNP6, and the source code of MCNP6 or any previous version of MCNP was not used as a reference. As discussed in Sec. 3, many of the used interaction models are common in other Monte Carlo photon transport codes as well.

There are several different photon interaction data libraries available in MCNP6 which differ by the applied sources of data and approximations used. The eprdata12 library used here is mostly based on the ENDF/B-VI.8 [103], whereas the photon interaction data used in Serpent is taken from the ENDF/B-VII.1 when applicable. The photoatomic and atomic relaxation data included in both the ENDF/B-VI.8 and ENDF/B-VII.1 are based on the EPDL97 and EADL libraries, so there should

not be major differences between the releases. However, not all the interaction data needed are available through the ENDF, and also, the ENDF photon interaction data used in MCNP is processed with the NJOY code [104]. Thus, some differences exist between the photon data used in MCNP6 and Serpent.

In both codes, all the electron shells are included in the photoelectric effect and atomic relaxation [103]. For calculating the direction of the photoelectron, MCNP6 applies precomputed tables [80, 103] based on the work by Fischer and by Sauter, whereas the non-relativistic approximation of the Sauter distribution discussed in Sec. 3.2.2 is used in Serpent. The atomic relaxation procedure is modelled similarly in MCNP6 [103] and Serpent. In both codes, modelling of Rayleigh scattering is based on the form factor approximation, and the direction of the Compton-scattered photon is sampled using the incoherent scattering function approximation. Logarithmic interpolation method is used for both scattering interactions in both Serpent and MCNP6 [103]. The pair production model used in MCNP6 has not been extensively documented, as far as the author knows. Electron-positron annihilation is modelled at rest in both codes. Differences may exist in the details of the various procedures, e.g., in the applied interpolation and sampling methods.

Notable differences exist in the Doppler broadening methods used for calculating the energy of the Compton-scattered photon. According to the original documentation of the Doppler broadening in MCNP5 [105, 106], the variable $p_z$ is sampled in MCNP in a way that $|p_z/(\alpha m_e c)| \leq 100$ is always true, whereas in Serpent the full range of $p_z$ is used as discussed in Sec. 3.4.8. Not only does the sampling range of $p_z$ have a direct effect on the shell-wise energy distributions, but it also affects the shell probabilities. In Sec. 3.4.8, it was shown that the sampling range of $p_z$ can have a major effect on the energy-angular distribution at large scattering angles. However, it should be noted that the "$|p_z/(\alpha m_e c)| \leq 100$" method tested for Serpent in Sec. 3.4.8 is likely to differ from the one used in MCNP6. Some issues related to the representation of the Compton profile data in MCNP have been found, but these problems have been reportedly fixed [107]. Whether the actual implementation described in Refs. [105, 106] has been updated for MCNP6 is unknown.

The comparison of the TTB models used in MCNP and Serpent is difficult because the implementation of the MCNP model has not been documented, as far as the author knows. However, some differences can be figured out from the documentation of the MCNP electron transport. Apparently, the radiative and collision stopping powers are calculated in MCNP whereas tabulated data from NIST [101] is used in Serpent. The most important difference in the MCNP approach is that it takes into account the density effect correction on the electron stopping powers [108]. The density effect correction was not included in the Serpent TTB method, but it should be implemented in the future. In both MCNP and Serpent, the bremsstrahlung energy distributions given by Seltzer and Berger [91, 92] are used. However, in MCNP, the same bremsstrahlung distributions are used for positrons and electrons, whereas in Serpent a separate treatment for positrons is possible, as discussed in Sec. 5.5. Angular distribution of bremsstrahlung photons is omitted in both codes.

## 6.2 Energy spectrum in an infinite geometry

In this test case, the photon spectrum was tallied in a sphere of radius $10^9$ cm containing a single isotropic, monoenergetic point source at the centre. Due to the large size, the geometry can be regarded as infinite and therefore no photons are leaked from the system. The tested elements were H, O, Fe, Ag, Nd, and U, each with a mass density of 1 g/cm$^3$. Also, the spectrum in H$_2$O (mass fractions $w_H = 0.111894$ and $w_O = 0.888106$, mass density 0.998207 g/cm$^3$) and UO$_2$ (mass fractions $w_O = 0.118473$ and $w_U = 0.881527$, mass density 10.437501 g/cm$^3$) were studied. The simulations were carried out with source energies of 0.1, 1, 10 and 100 MeV. The number of photons was $10^9$ with the source energy of 0.1 MeV and $10^8$ with the other energies. Both positron bremsstrahlung models were tested in Serpent, one in which positrons are treated as electrons, and the other in which positrons have separate distributions. The results are compared using the relative difference which is here given by

$$RD = \frac{\text{Serpent result} - \text{MCNP6 result}}{\text{MCNP6 result}}. \tag{6.1}$$

The same dense energy grid was used for tallying the spectrum in Serpent and MCNP6 simulations.

The calculated spectra and the relative differences are plotted in Figs. 6.1-6.4 for the tested materials and energies. The spectra of hydrogen and oxygen are shown in Fig. 6.1. For source energies of 0.1 and 1 MeV, very good agreement is obtained at the highest part of the spectrum which is mainly formed by Compton-scattered photons. However, just above the bremsstrahlung continuum, which is the linear region at the low end of the spectrum plot, the spectrum given by Serpent is much higher. In the case of hydrogen, the spectrum given by Serpent is over 400% higher for the source energy of 0.1 MeV and over 100% for the 1 MeV source. In the case oxygen, the differences are smaller, about 65 and 12% at their highest for 0.1 and 1 MeV, respectively. Further testing indicated that these differences are caused by the Doppler broadening of Compton-scattered photons. In Fig. 6.5, close-ups of the hydrogen spectrum for 0.1 MeV photons are shown with and without the Doppler broadening. Without the Doppler broadening, i.e. when only the ISF approximation is used, good agreement is obtained between Serpent and MCNP6. Interestingly, at the highest point of the spectrum between 6 and 8 keV, the Doppler-broadened spectrum given by MCNP6 does not differ from the one obtained without the broadening. However, between 71 and 73 keV, the effect of the broadening is notable. Another observed inconsistency is that the spectrum given by MCNP6 is non-zero just below the source energy. In the energy interval between $E - E_b$ and $E$, where $E$ is the source energy and $E_b$ is the lowest electron binding energy, the spectrum should be zero because the maximum energy of a Compton-scattered photon is $E - E_b$ and the bremsstrahlung photons produced by photoelectrons at this energy interval are negligible. This behaviour is correctly predicted by Serpent but not by MCNP6. These results could mean that the Doppler broadening is not always used in MCNP6.

The "$|p_z/(\alpha m_e c)| \leq 100$" method was also tested in Serpent but it did not remove the observed differences.

At the low end of the spectrum where the bremsstrahlung continuum dominates, the Serpent results are a few percent lower for the source energies of 0.1 and 1 MeV in both hydrogen and oxygen. When the source energy is increased to 10 MeV, the differences increase throughout the spectrum, and at 100 MeV, the spectrum given by Serpent is 15–30% lower for hydrogen below about 40 MeV, and 10–18% lower for oxygen below about 90 MeV. The large differences are caused by the bremsstrahlung radiation produced by the high-energy electrons which are generated mainly through Compton scattering but also through pair production at 100 MeV. More precisely, the differences are due to the density effect correction taken into account in MCNP6 but not in Serpent. The density effect is especially seen in this case because the mass density used was 1 g/cm$^3$, which is much higher than the densities of hydrogen ($8.37480 \times 10^{-5}$ g/cm$^3$) and oxygen ($1.33151 \times 10^{-3}$ g/cm$^3$) for which the stopping powers provided by NIST have been calculated [101]. There is no major difference between the results of the two positron bremsstrahlung models in hydrogen or oxygen, which is because the bremsstrahlung energy distribution of positrons is very close to that of electrons in low-$Z$ elements.

The spectra for iron and silver are shown in Fig. 6.2. Good agreement is achieved for the source energies of 0.1 and 1 MeV in general. However, the Serpent spectrum is much higher just above the energy region where the bremsstrahlung continuum dominates, similar to hydrogen and oxygen. The maximum difference is over 40% in iron and 60% in silver. Also, at the high end of the spectrum for the source energy of 0.1 MeV, the spectrum given by Serpent is about 10% lower. Again, these differences are caused by the Doppler broadening. In Fig. 6.6, the spectrum in silver for the 0.1 MeV source energy is shown in more detail at the regions of the largest differences. It seems that in Serpent, the inner shells with broader Compton profiles have higher interaction probabilities than the outer shells. This could be due to differences in the way the Compton profiles are normalized. According to Ref. [109], the integrated Compton profiles in MCNP are within 10% from the correct values for inner shells of higher-$Z$ elements, whereas in Serpent they are within 5%, though it is not possible to draw any certain conclusions based on these numbers. Another noticeable difference in Fig. 6.6 is that there are several high peaks in the MCNP6 spectrum below 60 keV, which are all non-physical because there exists no fluorescence lines at these energies. Similar peaks can also be observed in some of the spectra of the other tested elements.

In the case of the 1 MeV source in iron and silver, a small decrease can be seen in the spectra close to 0.1 MeV. Also, above 0.2 MeV or so, the spectra given by Serpent are slightly higher. These differences disappeared when the Doppler broadening was switched off. Therefore, they could be caused by the fact that in Serpent the value of $p_z/(\alpha m_e c)$ is not confined below 100, which leads into a wider energy distribution because $p_z$ is an increasing function of the scattered photon energy. Also, the shell probabilities can play a role in the observed differences.

Unlike in hydrogen and oxygen, the difference between the spectra given by the two positron bremsstrahlung models is evident in iron and silver for the source energies of 10 and 100 MeV. When positrons are treated differently than electrons, the Serpent spectrum is about 1–5% lower in iron and 3–10% lower in silver, excluding the high end of the spectrum. This is anticipated because the radiation yield is lower for positrons than electrons as was discussed in Sec. 5.5. The result also shows that the bremsstrahlung background forms an important portion of the spectrum for high-energy source photons. A reasonably good agreement is found when positrons are treated as electrons, except between about 2 and 8 MeV for the 10 MeV source and above a few tens of MeV for the 100 MeV source, in which cases the Serpent spectra are lower. In the case of the 100 MeV source in silver, the difference is over 30%. The differences may be caused by some problem in the interpolation methods used for calculating the TTB energy distribution in Serpent, but there could also be some differences in the treatment of pair production between Serpent and MCNP6. The large difference in the case of the 100 MeV source might not be important, because the spectrum is very low at the high end, and also, the TTB approximation is most likely to be a bad choice at such high energies in any case.

The qualitative features of the spectra of neodymium and uranium shown in Fig. 6.3 are similar to the ones seen with iron and silver. The maximum differences due to the Doppler broadening are about 70 and 40% for the 0.1 MeV source in neodymium and uranium, respectively. A decrease in the spectrum given by Serpent is seen between 0.1 and 0.2 MeV for the 1 MeV source, again caused by the Doppler broadening. The spectra are slightly higher above a few hundred keV and lower in the bremsstrahlung continuum for the 1 MeV source. The sharp peaks seen in the relative difference curve of uranium are caused by discontinuities in the MCNP6 spectrum, similar to the ones seen in Fig. 6.6. Greater differences are seen between the two bremsstrahlung models than in the case of the lighter elements, which is due to the *Z*-dependence of the bremsstrahlung radiation. When the separate treatment of positrons is used, the Serpent spectrum is about 4–12% lower in neodymium and 5–16% lower in uranium for the 10 and 100 MeV sources, except at the high end of the spectrum of the 100 MeV source where the differences are again greater. A good agreement is found for the 10 MeV source when positrons are treated as electrons, with the exception of the 4–6% difference close to 5 MeV. The agreement is slightly worse for the 100 MeV source which is most likely due to some difference between the TTB models.

The energy spectra in water and $UO_2$ are shown in Fig. 6.4. In water, the spectra and the relative differences are very close to the ones obtained in oxygen. When the source energy is 10 and 100 MeV, the differences between Serpent and MCNP6 results are slightly greater than in oxygen. The relative differences are larger in $UO_2$ than in uranium. The spectrum given by Serpent is about 5–7% lower for the 10 MeV source and 5–10% lower in the case of the 100 MeV source. As already mentioned, the density effect correction for the collision stopping power is not included in Serpent, which is most likely to be the main cause of the differences. Also in Serpent, the collision stopping powers in compounds are calculated using the Bragg's additivity rule, which is not a good approximation as was discussed in Sec. 5.3.1.
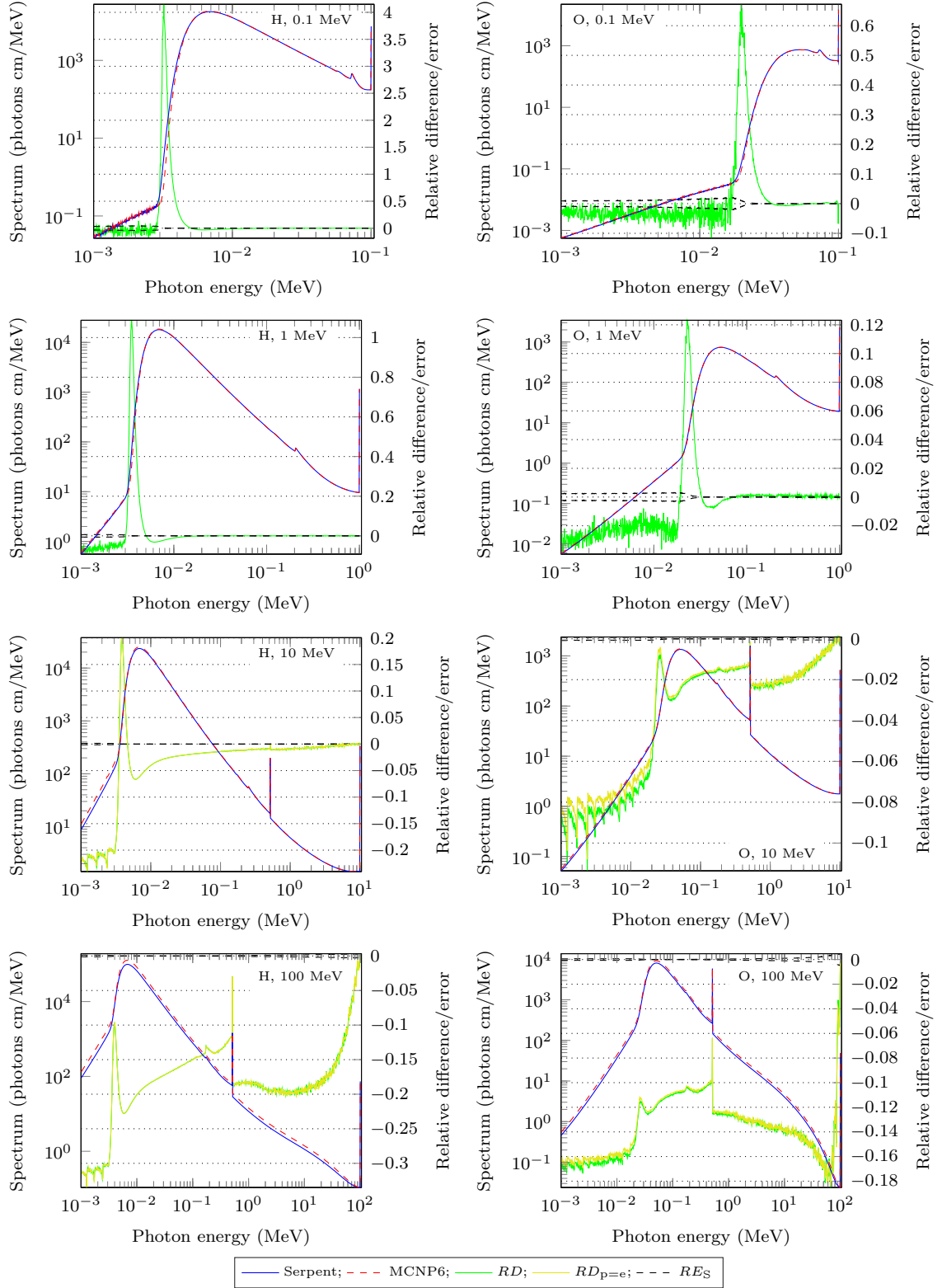
Figure 6.1: Volume integrated photon energy spectrum in an infinite geometry for hydrogen and oxygen calculated with Serpent and MCNP6. The right vertical axis indicates the values of the relative differences ($RD$ and $RD_{p=e}$) and the relative statistical error given by Serpent ($RE_S$). In the case of $RD$, a separate treatment of positron bremsstrahlung was used in Serpent, whereas in the case of $RD_{p=e}$, positrons were treated as electrons. Serpent spectra are the ones with the separate positron treatment, corresponding to $RD$.

Figure 6.2: Volume integrated photon energy spectrum in an infinite geometry for iron and silver calculated with Serpent and MCNP6. The description of the plots is the same as in Fig. 6.1.
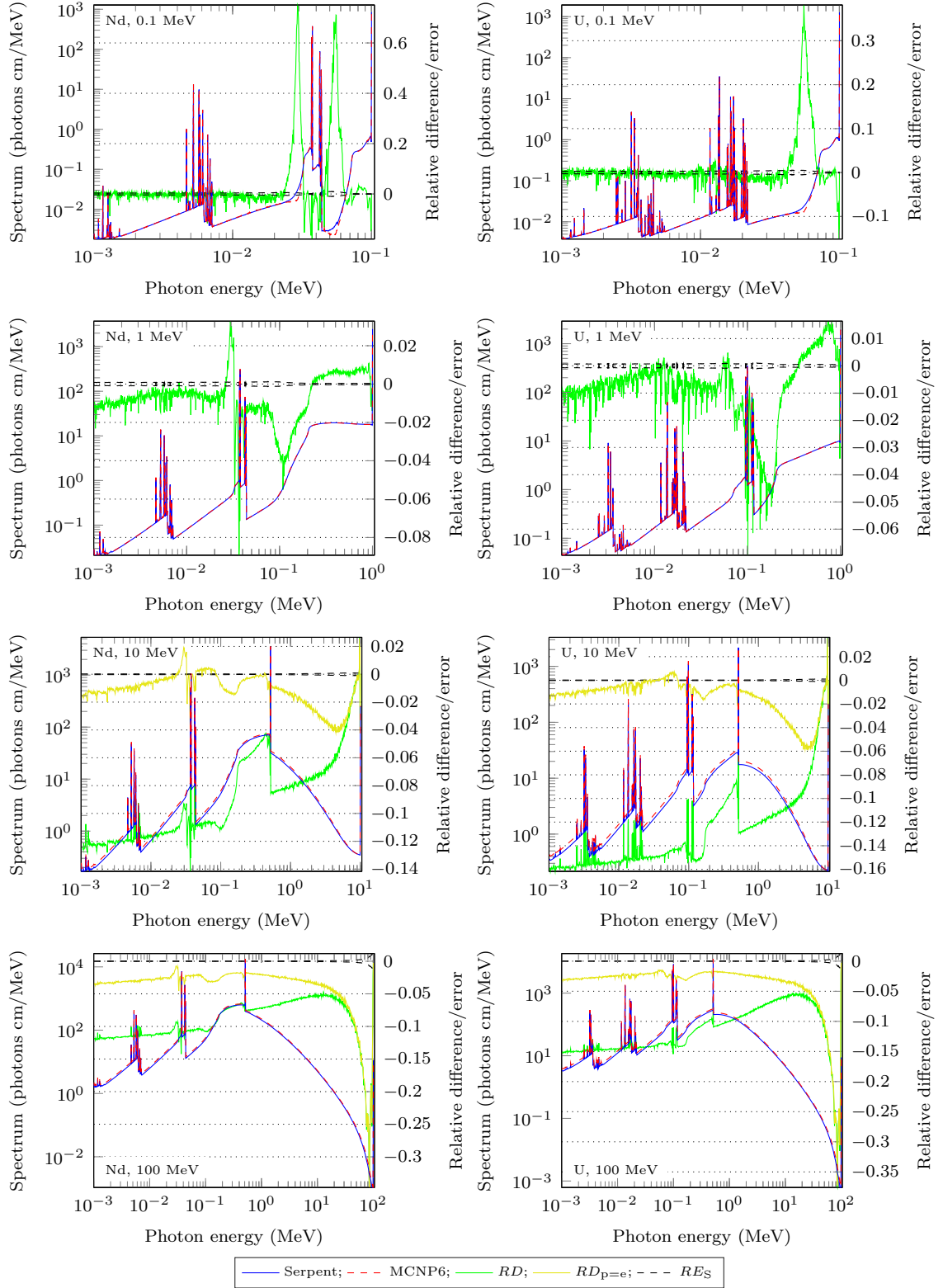
Figure 6.3: Volume integrated photon energy spectrum in an infinite geometry for neodymium and uranium calculated with Serpent and MCNP6. The description of the plots is the same as in Fig. 6.1.

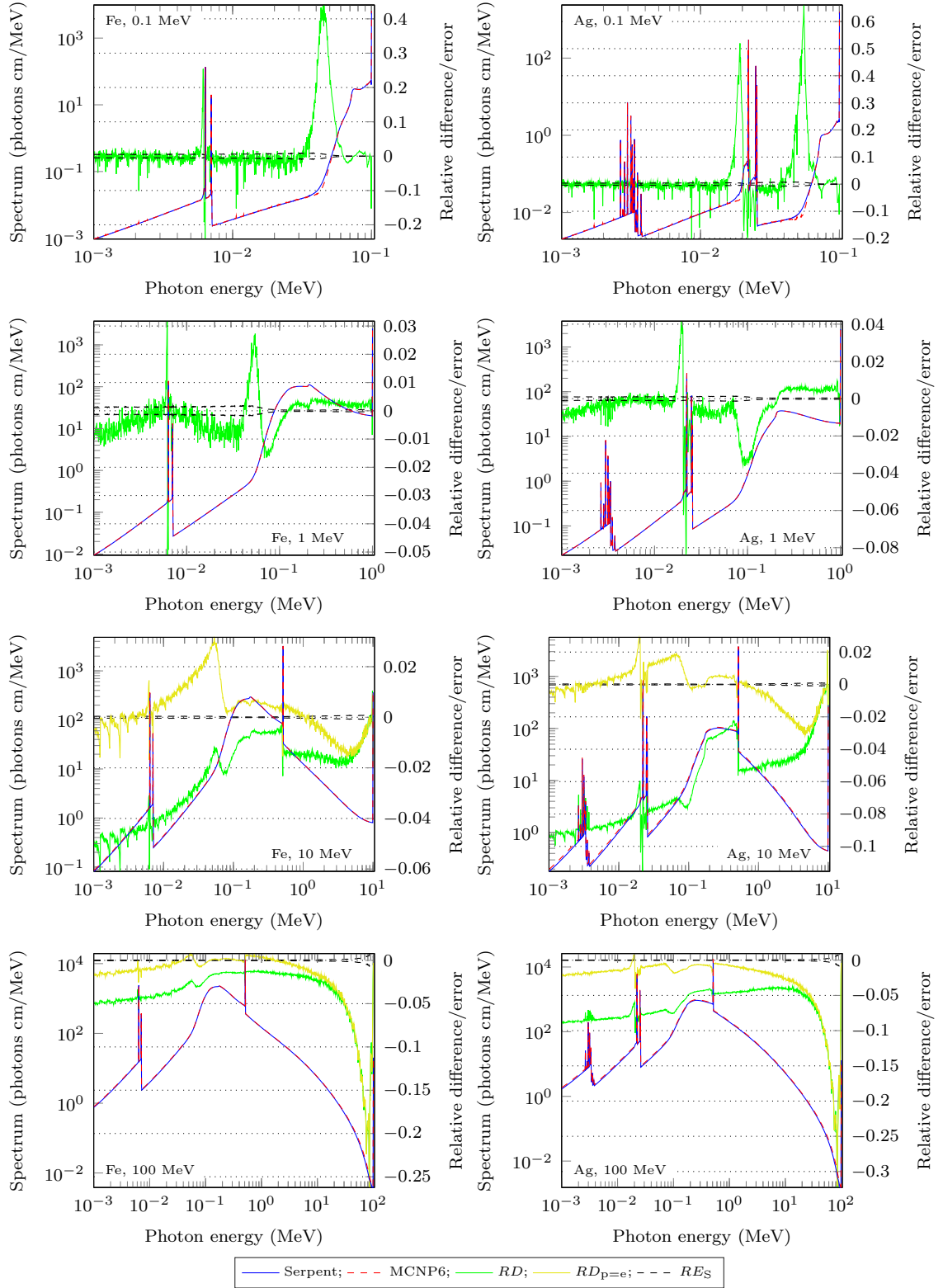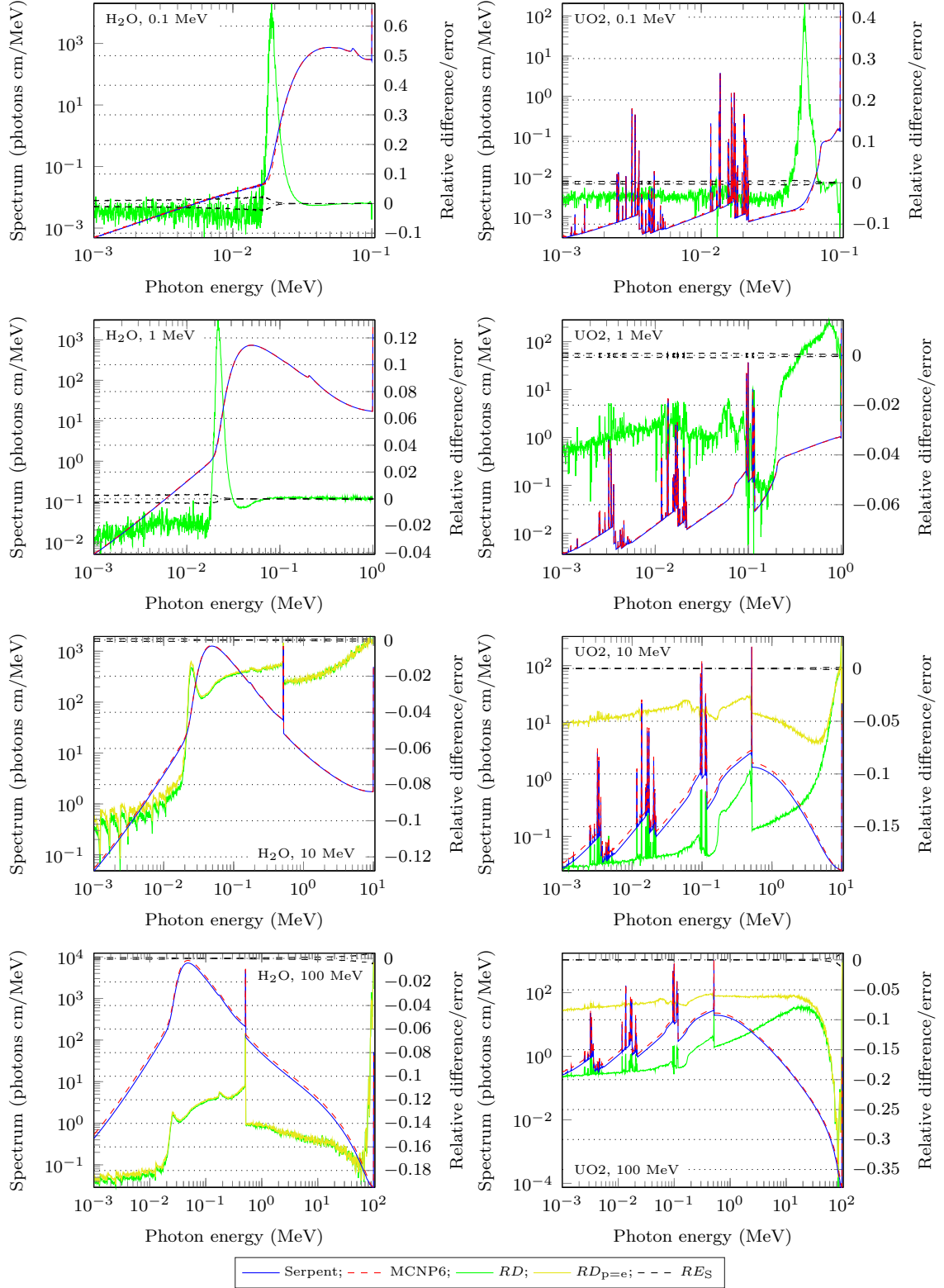Figure 6.4: Volume integrated photon energy spectrum in an infinite geometry for water and uranium dioxide calculated with Serpent and MCNP6. The description of the plots is the same as in Fig. 6.1.

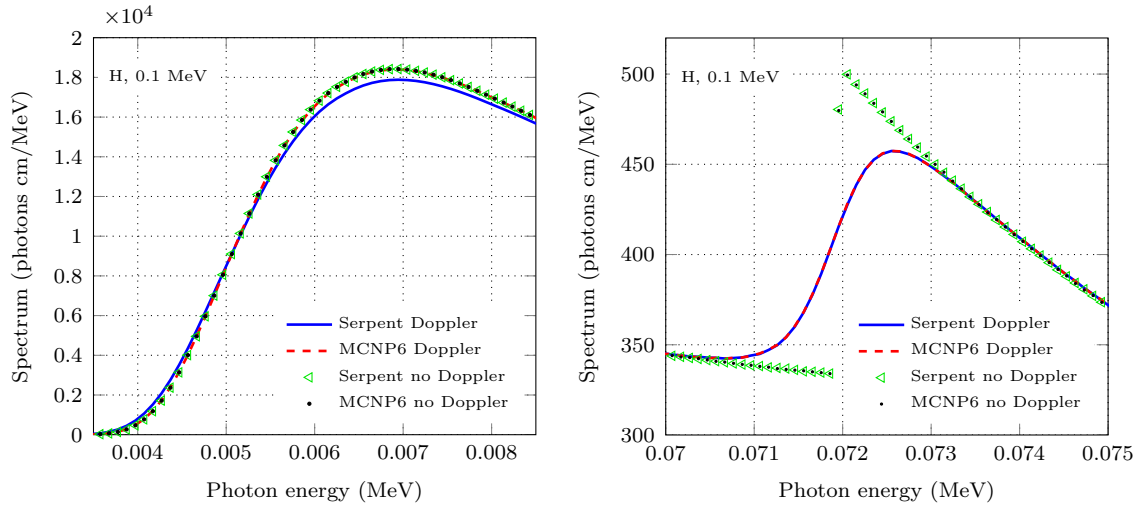Figure 6.5: Volume integrated photon energy spectrum for 0.1 MeV source photons in hydrogen calculated with Serpent and MCNP6 with and without the Doppler broadening.
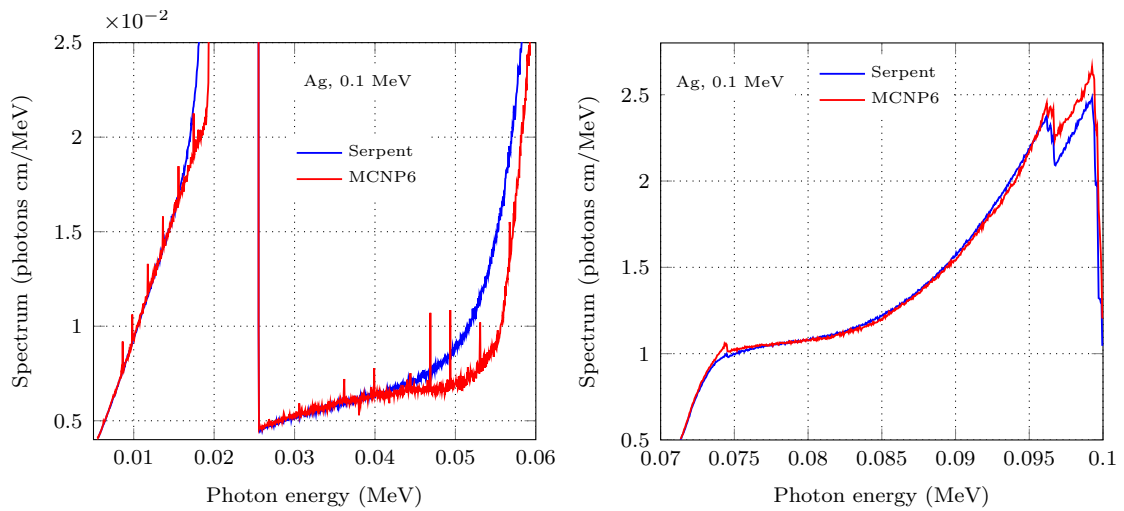


Figure 6.6: Volume integrated photon energy spectrum for 0.1 MeV source photons in silver calculated with Serpent and MCNP6.
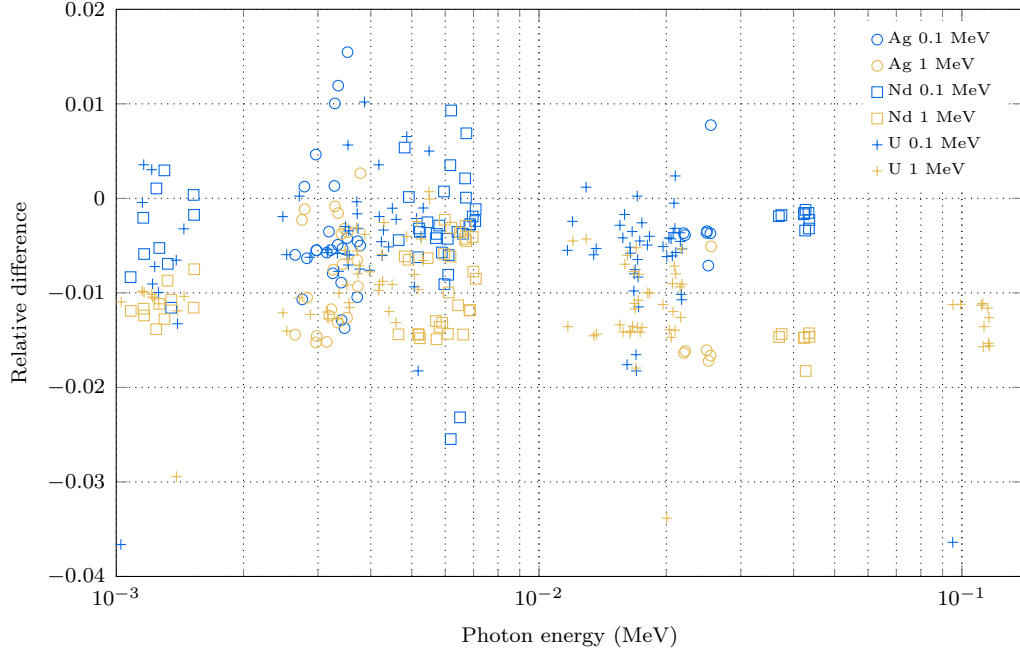
Figure 6.7: Relative difference between Serpent and MCNP6 at the fluorescence energies taken from Figs. 6.2 and 6.3 in silver, neodymium, and uranium for the source energies of 0.1 and 1 MeV. Not all fluorescence energies are separately included because they were not explicitly tallied.

The relative differences at the energy bins corresponding to the fluorescence energies of silver, neodymium, and uranium are plotted in Fig. 6.7 for the 0.1 and 1 MeV sources. In the case of the 0.1 MeV source, most of the spectrum values are within 1% and the Serpent results are slightly lower than MCNP6 values on average. When the source energy is 1 MeV, the Serpent spectrum values are 1% lower on average. The differences are probably related to the shell probabilities of Compton scattering. In any case, no major differences are observed which indicates that the atomic relaxation procedure behaves similarly in Serpent and MCNP6. However, when the Doppler broadening was switched off, the Serpent spectrum was much lower at the fluorescence energies, the difference was as much as 20%. Most likely, the shell is always sampled in the Compton scattering method of MCNP6, unlike in Serpent in which the shell is sampled only when the Doppler broadening is used. This behaviour could be changed in the future.

The running times of Serpent and MCNP6 were compared for H, C, O, Al, Fe, Ge, Ag, Nd, W, Pb, and U using the same spherical geometry but without any tallies. The density of 1 g/cm$^3$ was used for all the elements, and positrons were treated as electrons in Serpent. The number of photons was 10$^8$ for the 0.1 MeV source and 10$^7$ for the rest of the energies. All cases were run on a single-core of a 3.47GHz Intel Xeon X5690 processor. The speed-up factor of Serpent compared to MCNP6 is shown in Fig. 6.8. Serpent is considerably faster than MCNP6 in most of the cases. For the lightest elements, the speed-up factor is between 1.4 and 2. The
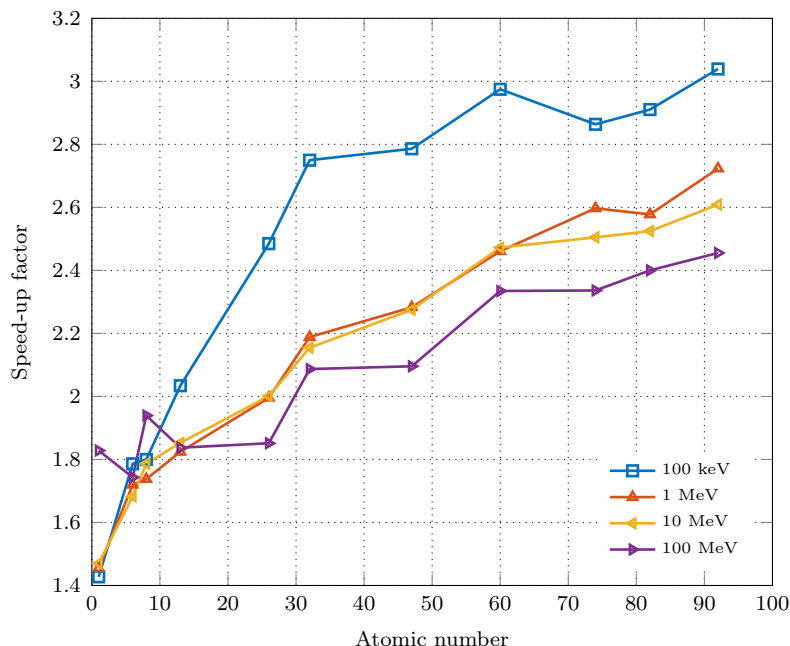
Figure 6.8: Speed-up factor of Serpent 2 compared to MCNP6 in the infinite geometry case without any tallies.

speed-up factor increases with the atomic number and is between about 2 and 3 for germanium and heavier elements. The speed-up factor is largest for 0.1 MeV photons, with the exception of the lightest elements, and decreases as a function of energy. Although Serpent seems to perform very well, a couple of things should be beared in mind. First of all, it is possible that the pre-compiled version of MCNP6 hasn't been compiled with full optimization. Also, the cause of the differences in the calculation times may not lie in the photon physics routines, but in other parts of the codes. For example, Serpent uses the unionized energy grid for all point-wise reaction cross sections [110]. However, the Woodcock delta-tracking method applied in Serpent [18] should not be the cause in this simple homogeneous geometry. One factor which possibly explains the difference in the speed-up factor at high energies is that the bremsstrahlung yield in Serpent is lower than in MCNP6, especially at 100 MeV, which results in reduced computation times. It is also important to note that some of the Serpent photon physics routines have not been fully optimized yet.

## 6.3 Energy-angular spectrum in a cylinder

The purpose of this test case is to study the spatial distribution of photons as they propagate through the medium. The angular distribution of photons is mainly characterized by the Compton effect, but Rayleigh scattering and the secondary photons generated through atomic relaxation, electron-positron annihilation, and bremsstrahlung process also play a role. A cylindrical geometry was used for tallying the spectrum and total integral flux as a function of the cylindrical coordinates $z$

and $r$. A single mono-directional point source was used at the centre of the cylinder pointing towards the positive axial direction. The studied materials were lead and water for the source beam energies of 0.1, 1, and 10 MeV. The density and mass fractions of water were the same as in the infinite geometry case, the density of lead was 11.35 g/cm$^3$. The number of photons was $5 \times 10^{10}$ for the source energies of 0.1 and 1 MeV and $10^{10}$ in the 10 MeV cases. For the 100 keV source in lead, the radius and height of the cylinder were 0.2 and 0.4 cm, respectively. For 1 MeV and 100 MeV photons in lead, the radius was 5 cm and the height 10 cm. In water, the radius was 50 cm and the height 100 cm for all energies. Positrons were treated as electrons in the TTB approximation of Serpent. Cylindrical mesh detector was used in Serpent and the FMESH tally in MCNP6 for the whole cylindrical geometry. In all the cases, the number of radial and axial bins were 50 and 100, respectively.

The spectra in lead for the 0.1 MeV source is shown in the top row of Fig. 6.9 at six locations of the cylinder. The spectrum given by Serpent is much higher close to 0.05 and 0.1 MeV at $r = 0.004$ cm and $z = -0.004$ cm which is just below the source point. The differences become smaller with increasing $r$, especially close to 0.1 MeV. Above the source point the differences are much smaller, although the Serpent spectrum is higher close to 0.05 MeV. Most likely, the differences are caused by the Doppler broadening of Compton-scattered photons, however, the exact reason is difficult to understand. The limited sampling of $p_z$ in MCNP6 cannot directly cause the difference because the maximum value of $p_z/(\alpha m_e c)$ given by Eq. (3.73) is about 26.8 for $E_k = 0.1$ MeV, $E_{b,i} = 0$ MeV, and $\theta = 180°$. At the location below the source point, the Serpent spectrum decreases rapidly between the interval of 96.5 and 97.6 keV, which corresponds to the maximum energies of photons scattering from the three outermost shells for which $E_{b,i} > 1$ keV. On the other hand, the MCNP6 spectrum decreases rapidly between the interval of 91.5 and 94 keV which does not correspond to any maximum energies of Compton-scattered photons. It is unclear what causes this major difference at this energy region.

The total flux and the relative difference between Serpent and MCNP6 are shown in the bottom row of Fig. 6.9 in lead for the 0.1 MeV source. The total flux decreases rapidly as a function of both $r$ and $z$ because the photoelectric effect is the dominant interaction in lead for this energy. Good agreement is observed between Serpent and MCNP6 in the region where the flux is highest. However, some differences can be seen in the region where $r > 0.1$ cm which could be due to the differences in the Doppler broadening method. It is important to note that the majority of the 0.1 MeV photons are absorbed in a very small volume around the source point. Therefore, the differences seen in the spectra and the total flux should not be important if one is interested in the energy deposition of low-energy photons, for example.

The spectra for the 1 MeV photon beam in lead are shown in Fig. 6.10, where major differences are seen in the backscattered photon spectra. Below the source point at $r = 0.1$ cm and $z = -0.1$ cm, the agreement is good below about 0.32 MeV. However, above this energy the spectrum given by Serpent is much higher than the one of MCNP6, the maximum difference between 0.32 and 0.9 MeV is over

Figure 6.9: At the top row, the volume integrated photon energy spectrum for 0.1 MeV photon beam in a lead cylinder at six locations of the geometry. At the bottom row, the total integral flux given by Serpent in the cylinder and the relative difference (Eq. (6.1)) compared with MCNP6. The source beam was located at the origin, pointing in the $z$-direction. The bottom of the cylinder was excluded from the figure due to insufficient statistics.

an order of magnitude. The difference decreases for increasing $r$ but remains still very large. Most of the difference can be explained by the limited sampling of $p_z$ in the Doppler broadening method of MCNP6. However, the maximum energy of a photon with an incident energy of 1 MeV scattering at 180° is about 0.41 MeV when $p_z/(\alpha m_e c)$ is limited below 100, whereas the maximum energy in the MCNP6 spectrum is somewhere between 0.32 and 0.34 MeV. Therefore, there seems to exist some mechanism limiting the maximum energy of scattered photons in MCNP6, which was also observed in the case 0.1 MeV beam. Above the source point, the spectra are in much better agreement, although some difference is observed at the high end of the spectrum for increasing $r$.
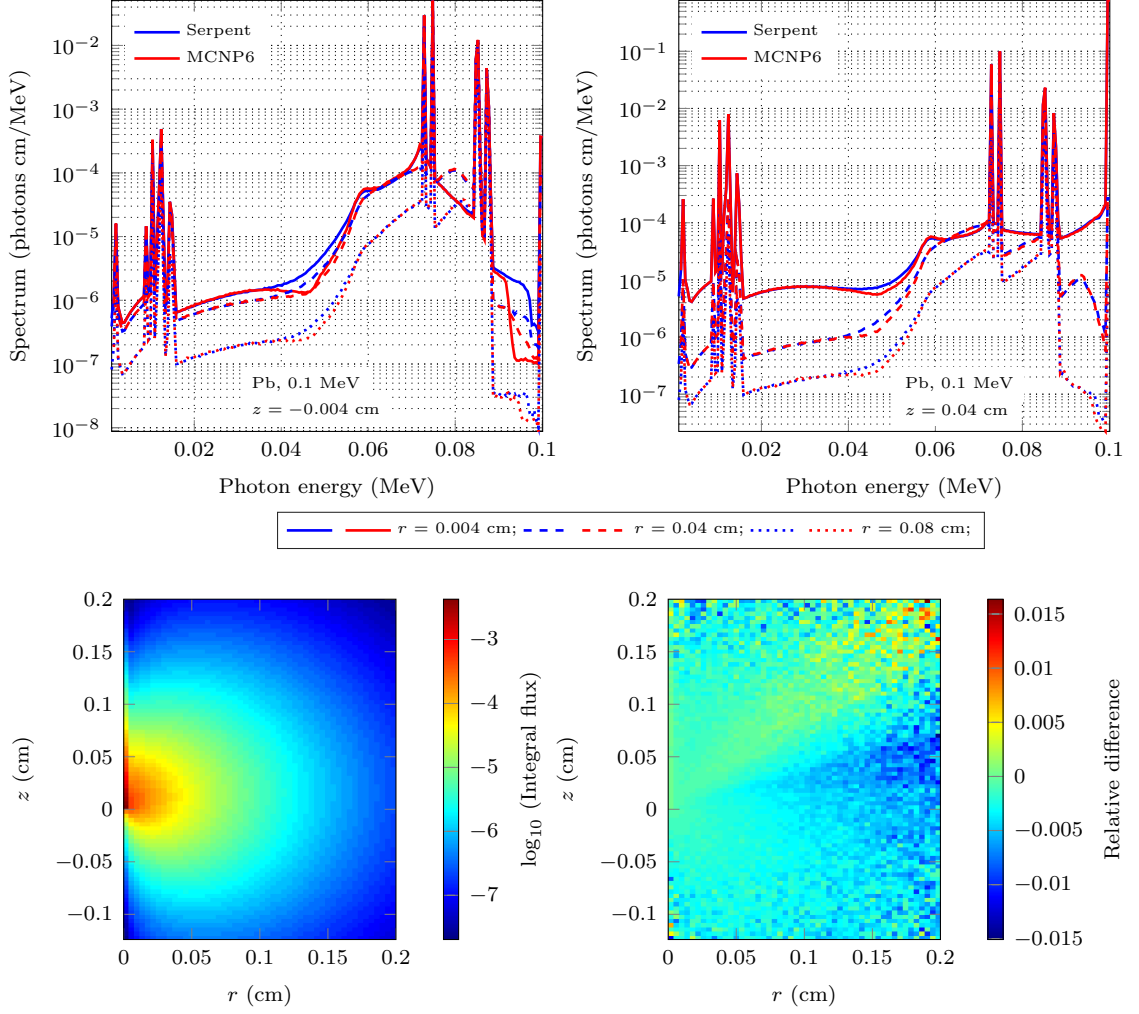
Figure 6.10: At the top row, the volume integrated photon energy spectrum for 1 MeV photon beam in a lead cylinder at six locations of the geometry. At the bottom row, the total integral flux given by Serpent in the cylinder and the relative difference (Eq. (6.1)) compared with MCNP6.

The total integral flux for the 1 MeV beam in lead is shown in the bottom row of Fig. 6.10. The total flux given by Serpent is over 200% higher in the region below the source point. This is caused by the differences observed in the energy-angular distribution at the top row of Fig. 6.10. However, the differences are very small in the forward direction where the flux is highest, which can be seen from the logarithm of the absolute relative difference. Because the total flux is so small below the source point, the observed differences should not be important, e.g., in energy deposition calculations.

In Fig. 6.11, spectra and total flux are shown for the 10 MeV source beam in lead. Below the source point, the spectrum is dominated by the isotropically emitted annihilation photons. Above the annihilation energy of 0.511 MeV, the Serpent
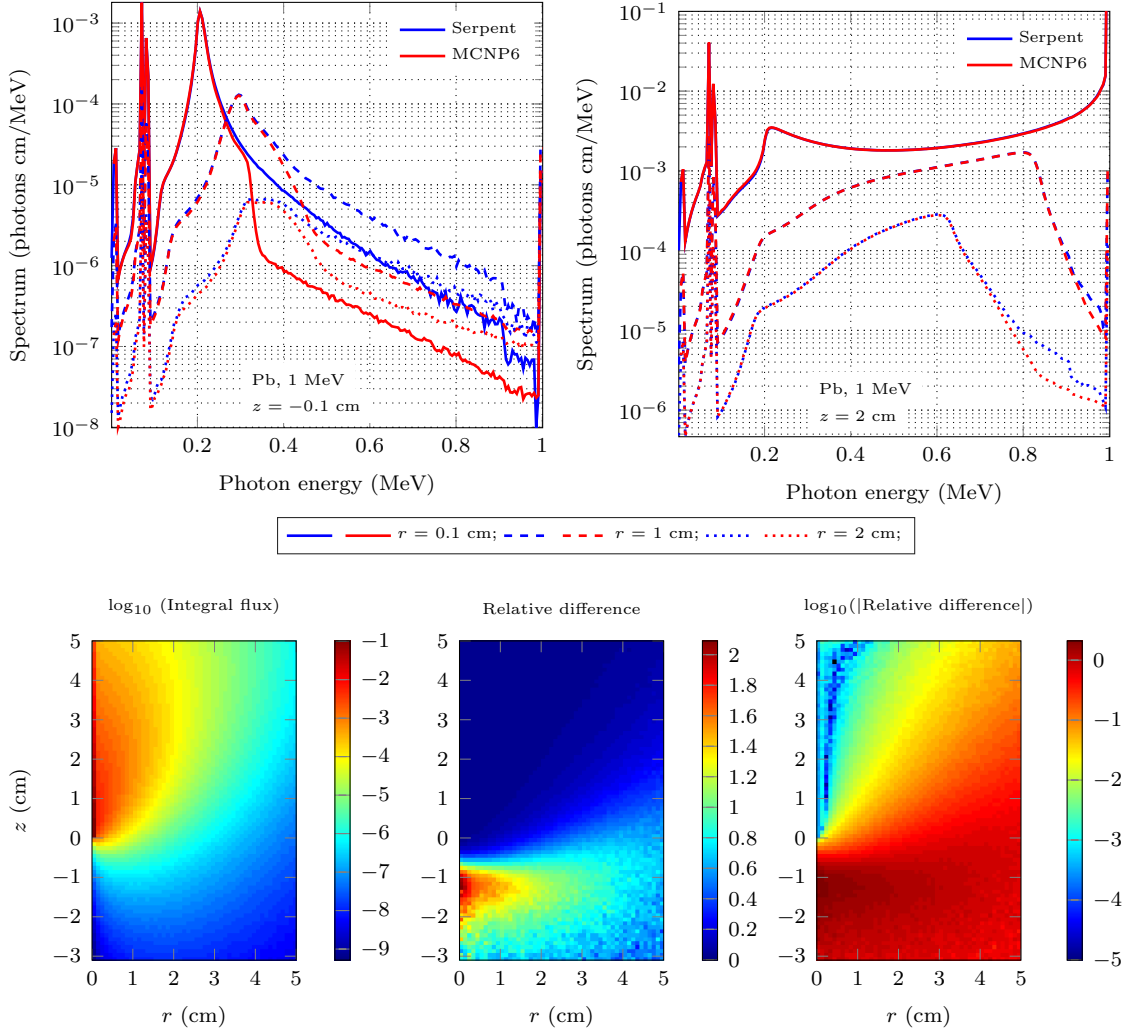
Figure 6.11: At the top, the volume integrated photon energy spectrum for 10 MeV photon beam in a lead cylinder at seven locations of the geometry. At the bottom row, the total integral flux given by Serpent in the cylinder and the relative difference (Eq. (6.1)) compared with MCNP6.

spectra are higher than the ones of MCNP6 due to the differences in Doppler broadening, which was also observed in the 1 MeV case. However, the spectra are very low at energies above 0.511 MeV for $z < 0$ cm, so the discrepancies should not be significant. Interesting differences are seen in the spectra which were tallied between $r = 0.0$ and $r = 0.4$ cm at $z = 2$ cm. Between 1 and 2 MeV, the Serpent spectrum is about 15% lower on the $z$-axis ($r \leq 0.1$ cm), while 15–25% higher when the radial coordinate $r$ is between 0.1 and 0.4 cm. Also, the total flux given by Serpent is about 10% lower close to the $z$-axis, but higher for increasing $r$. The differences in the total spectrum summed over $r$- and $z$-coordinates were similar to the ones seen in neodymium and uranium in Fig. 6.3. This case was also tested without the TTB approximation, which resulted in a good agreement for both energy spectra and the total flux. Therefore, the differences seen in Fig. 6.11 must be caused by the bremsstrahlung photons. As already discussed in Sec. 6.2, the discrepancies in the overall energy distribution are most likely caused by the differences in the TTB approximations. However, the TTB cannot cause the discrepancies observed in
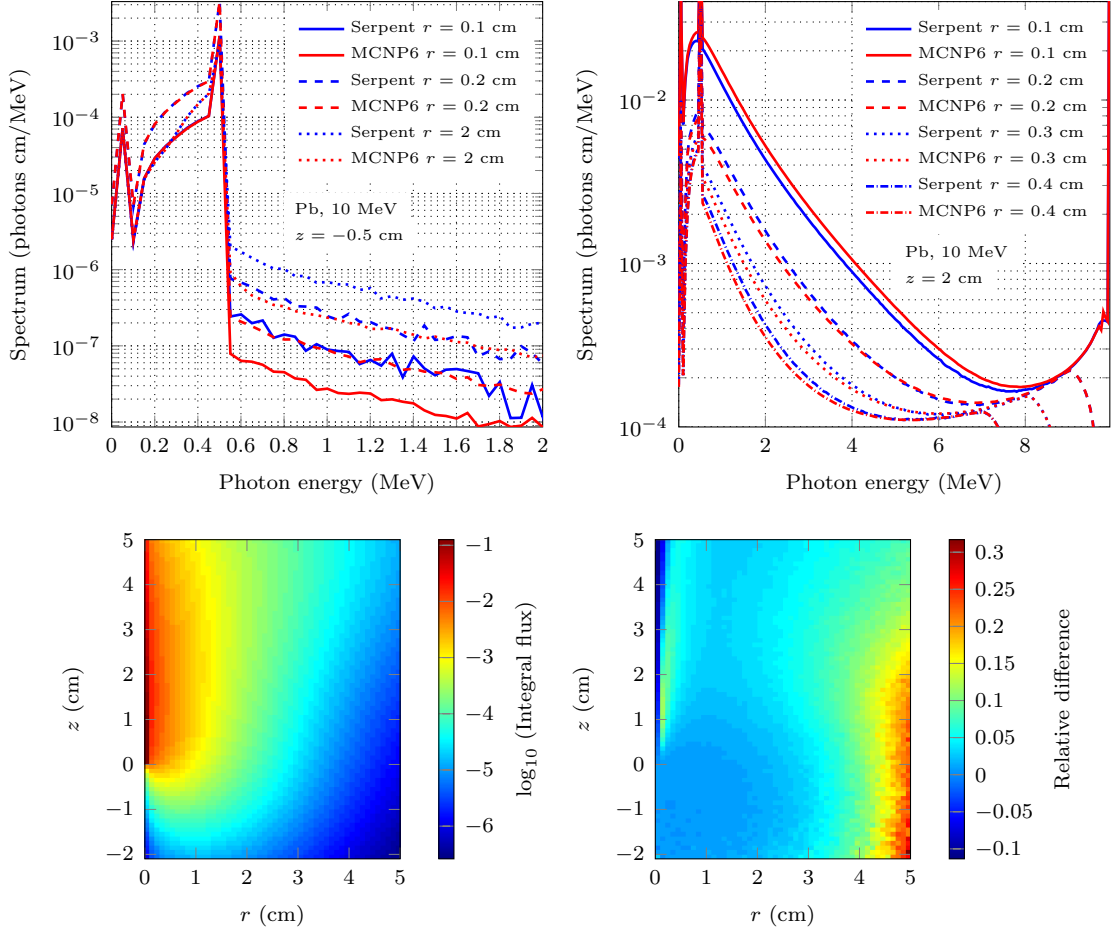
Figure 6.12: At the top row, the volume integrated photon energy spectrum for 0.1 MeV photon beam in a water cylinder at six locations of the geometry. On the left figure of the top row, the spectrum obtained without the Doppler broadening are shown for $r = 1$ cm. At the bottom row, the total integral flux given by Serpent in the cylinder and the relative difference (Eq. (6.1)) compared with MCNP6.

Fig. 6.11 because the direction of the bremsstrahlung radiation is not sampled in either MCNP6 or Serpent. The dominant interaction for 10 MeV photons in lead is pair production, so the observed differences are most likely due to different angular distributions used for electron-positron pairs. Unfortunately, there seems to be no documentation of the pair production model implemented in MCNP6, so the exact cause cannot be identified. Another discrepancy seen in Fig. 6.11 is that there is a small non-physical discontinuity in the MCNP6 spectrum close to the source energy.

Good agreement is observed in Fig. 6.12 between Serpent and MCNP6 for 0.1 MeV beam in water both below and above the source point in most parts of the spectra. However, a significant difference is seen at the high end of the spectrum below the

Figure 6.13: At the top row, the volume integrated photon energy spectrum for 1 MeV photon beam in a water cylinder at six locations of the geometry. At the bottom row, the total integral flux given by Serpent in the cylinder and the relative difference (Eq. (6.1)) compared with MCNP6.

source point at $r = 1$ cm and $z = -0.1$ cm. The rapid decrease in the MCNP6 spectrum is very similar to the one seen in lead with the same source energy, and occurs in the same energy interval, too. To study this peculiarity in more detail, the calculations were also carried out without the Doppler broadening. The results at $r = 1$ cm and $z = -0.1$ cm are also given in Fig. 6.12, which show a good agreement between Serpent and MCNP6. Close to the source energy, the MCNP6 spectrum obtained with the Doppler broadening is similar to the spectrum obtained without the broadening. This could mean that the Doppler broadening is not always used in MCNP6 for some reason. Good agreement is obtained for the total flux, although the flux given by Serpent decreases slightly faster away from the source point.

In the case of the 1 MeV beam in water shown in Fig. 6.13, the spectra are in good agreement both above and below the source point, and the differences in the total
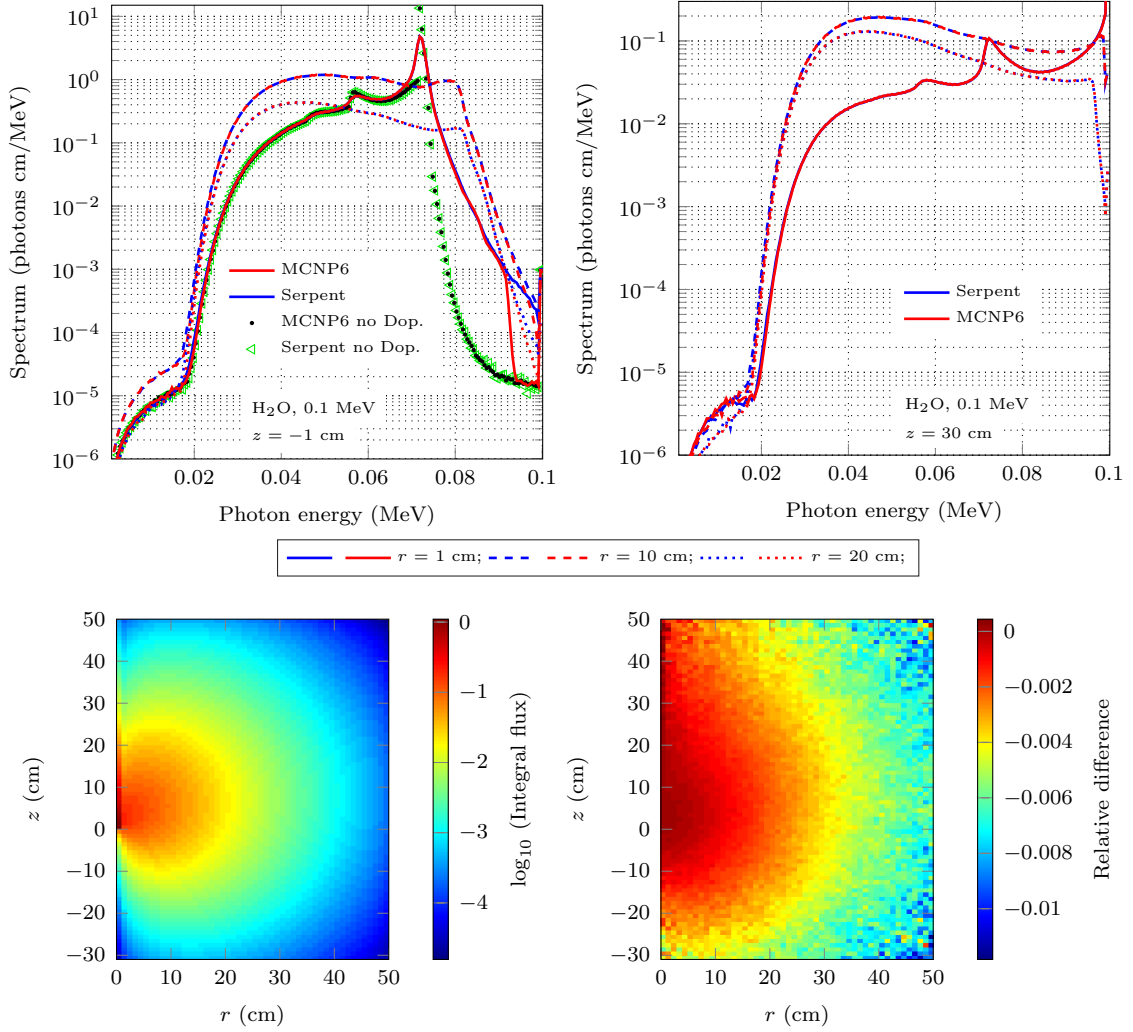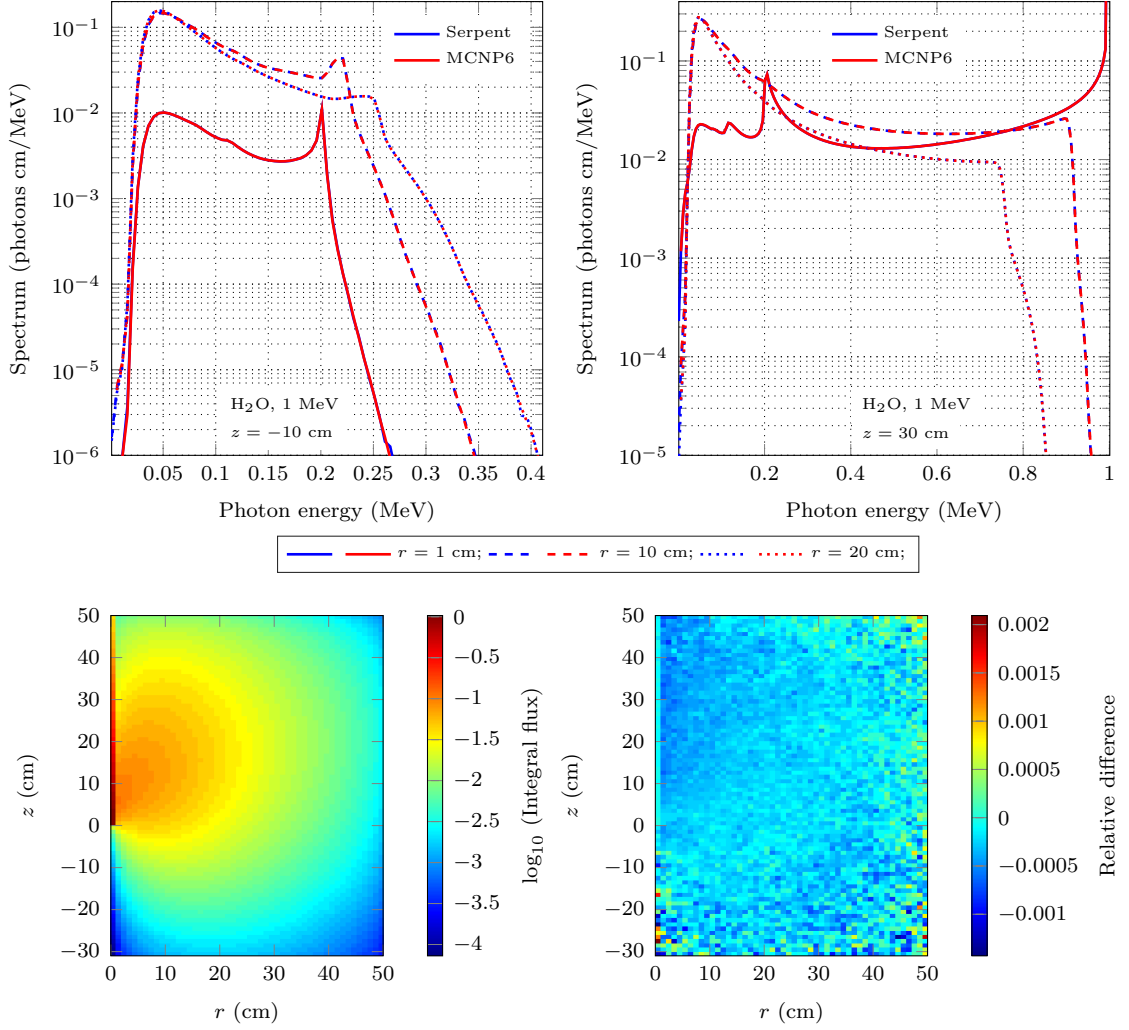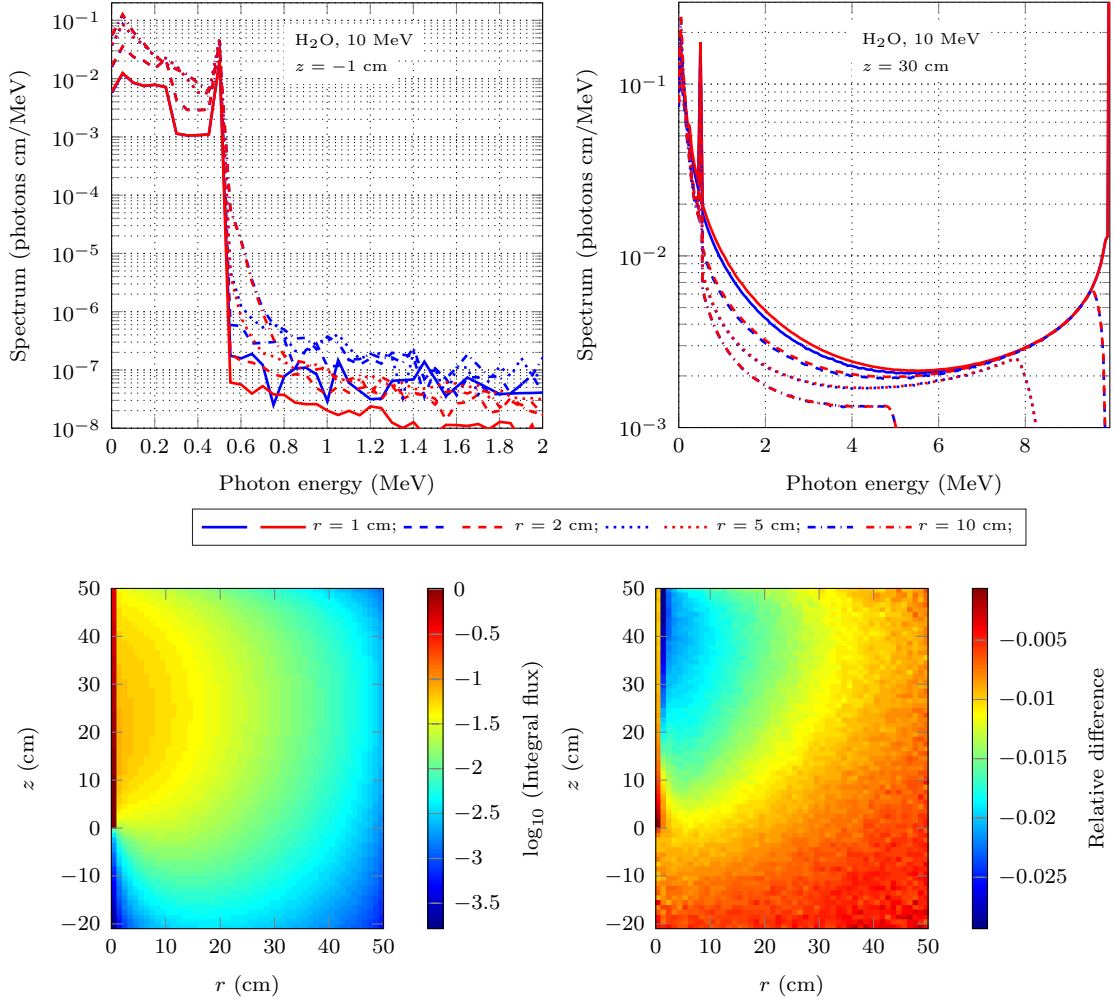
Figure 6.14: At the top row, the volume integrated photon energy spectrum for 10 MeV photon beam in a water cylinder at eight locations of the geometry. At the bottom row, the total integral flux given by Serpent in the cylinder and the relative difference (Eq. (6.1)) compared with MCNP6.

flux are small. Larger differences are observed when the source energy is increased to 10 MeV, shown in Fig. 6.14. Below the source point at energies above 0.511 MeV, the differences in the spectra are similar as in the case of the 10 MeV beam in lead, and they can be mostly ignored. Above the source point, the spectra given by Serpent are slightly lower than the MCNP6 spectra. Also, the total flux given by Serpent is smaller in the whole geometry. The maximum difference is about 3% close to the beam axis. This is a somewhat expected result because in the infinite geometry case, the energy spectrum given by Serpent was about 2–3% lower for the 10 MeV photon source in the highest part of the spectrum, as can be seen in Fig. 6.4. Note that Compton scattering is the dominant process for 10 MeV photons in water. Thus, the TTB approximation used for Compton electrons is most likely to be the main source of the observed differences instead of the angular distribution of pair production, which caused the discrepancies in lead with the same energy.

# 7    Conclusions

The topic of this thesis was to implement a photon transport model in Serpent 2 Monte Carlo code. The four main photon interactions — the photoelectric effect, Rayleigh scattering, Compton scattering, and pair production — were implemented in Serpent. Also, the important atomic relaxation, thick-target bremsstrahlung, and electron-positron annihilation processes were included. A large number of different approximations, sampling methods, and evaluations found in the literature were reviewed. Not only some commonly used approaches were chosen, but also a few new methods were developed. A new algorithm for sampling the direction of the photoelectron using the non-relativistic approximation of the Sauter distribution was presented. The Doppler broadening of Compton-scattered photons was improved by extrapolating the commonly used Compton profiles. A new, fast algorithm for sampling the energy of the electron-positron pair was presented. Also, a detailed method for sampling the direction of the Compton electrons was given.

The implemented photon transport mode was compared with MCNP6 using two test cases: an infinite geometry for studying the energy spectrum of photons, and a cylindrical geometry with a uniformly directed photon beam for studying the energy-angular distribution. The results showed a good agreement in general. Most of the observed differences were caused by the TTB approximation and the Doppler broadening of Compton-scattered photons. In low-$Z$ materials, the agreement was good at low energies below 1 MeV or so, but at 10 MeV and above, the lack of the density effect correction for the collision stopping powers resulted in lower Serpent spectrum. In the tested compounds, the Bragg's additivity rule used for calculating collision stopping powers in Serpent also resulted in lower spectrum. The agreement was reasonably good in medium- and high-$Z$ elements, except at the high end of the spectrum in the case of 100 MeV source where the differences in the TTB approximations resulted in much lower Serpent spectrum.

The Doppler broadening caused some notable differences in all the tested materials, mostly at low source energies. The largest discrepancies were seen in the backscattered photon spectrum in lead with a 1 MeV source, in which case the Serpent spectrum was an order of magnitude larger. Some of the discrepancies can be explained by the differences in the Doppler broadening models. Most importantly, the Compton profiles are extrapolated in Serpent but not in MCNP6, which results in broader energy distributions. Some results indicated that Doppler broadening is not always used in MCNP6. However, the differences related to Doppler broadening are most likely to be insignificant because they were observed mainly at low spectrum values, or at low energies at which photons are absorbed in short distances.

Other interesting results were also obtained. The separate treatment of positron bremsstrahlung in Serpent produced lower spectrum, which was the expected result. The spectral lines caused by atomic relaxation were in a good agreement between Serpent and MCNP6. The angular distribution of pair production seemed to cause discrepancies in the energy-angular distribution in the case 10 MeV source photons in

lead. Interestingly, non-physical discontinuities were detected in some of the spectra produced by MCNP6. A running time comparison was also carried out in a simple geometry without any tallies. The speed-up factor of Serpent compared to MCNP6 was between about 1.4 and 2 in low-$Z$ elements, and between 2 and 3 in medium- and high-$Z$ elements. The cause of the differences in the computation times may lie in the photon physics routines, but some other factors could also play a role.

In the future, comparisons between Serpent and full electron transport codes should be done in order to study the Compton scattering model and the accuracy of the TTB approximation. The validity of the implemented positron TTB model should be investigated in comparison with other Monte Carlo codes which treat positrons separately from electrons. More realistic calculations like a gamma-heating problem are to be done. Also, the validation of the implemented photon transport model must be carried out using experimental results and benchmark problems.

The presented photon transport model can be improved in several ways. In the photoelectric effect, the accurate Sauter distribution should be used for high-energy electrons, and the directions of L-shell electrons could be sampled from a separate distribution. In Compton scattering, the possibility of a more accurate sampling method for the RIA should be investigated, although the presented method should be reasonably accurate. Also, the validity of the different approximations made in the Compton scattering model should be studied in more detail. It should be straightforward to extend the energy range of the pair production model above 100 MeV. Also, it should be possible to extend the energy range of the interactions below 1 keV, although the accuracy of the cross section data is poor at low energies. The benefit of a more accurate electron-positron annihilation method for special applications should be investigated. Photonuclear interactions could be implemented at some point. Probably the most important areas of development are implementing the density effect correction for collision stopping powers and creating an angular distribution model for TTB photons. Other important development topics are the coupled neutron–photon transport mode and variance reduction techniques needed for shielding applications. Maybe one day a full electron transport mode will be implemented in Serpent.

# References

[1] J. Leppänen, M. Pusa, T. Viitanen, V. Valtavirta, and T. Kaltiaisenaho, "The Serpent Monte Carlo code: Status, development and applications in 2013," *Annals of Nuclear Energy*, **82**, 142–150 (2015).

[2] J. Leppänen, *Development of a New Monte Carlo Reactor Physics Code*, PhD thesis, Helsinki University of Technology, VTT Publications 640, 2007.

[3] E. Fridman and J. Leppänen, "On the use of the Serpent Monte Carlo code for few-group cross section generation," *Annals of Nuclear Energy*, **38**, *6*, 1399–1405 (2011).

[4] M. Pusa, *Numerical methods for nuclear fuel burnup calculations*, PhD thesis, Aalto University, VTT Science 32, 2013.

[5] T. Viitanen, *Development of a stochastic temperature treatment technique for Monte Carlo neutron tracking*, PhD thesis, Aalto University, VTT Science 84, 2015.

[6] J. Leppänen et al., "The Numerical Multi-Physics project (NUMPS) at VTT Technical Research Centre of Finland," *Annals of Nuclear Energy*, **84**, 55–62 (2015).

[7] F. Salvat, J. M. Fernández-Varea, and J. Sempau, "PENELOPE-2011: A Code System for Monte Carlo Simulation of Electron and Photon Transport," OECD-NEA, Issy-les-Moulineaux, France (2011).

[8] H. Hirayama, Y. Namito, A. F. Bielajew, S. J. Wilderman, and W. R. Nelson, "The EGS5 Code System," SLAC-R-730 and KEK Report 2005-8, Stanford Linear Accelerator Center, Stanford, CA (2013).

[9] I. Kawrakow, E. Mainegra-Hing, D. W. O. Rogers, F. Tessier, and B. R. B. Walters, "The EGSnrc Code System: Monte Carlo Simulation of Electron and Photon Transport," NRCC Report PIRS-701, Ottawa, Canada (2013).

[10] T. Goorley et al., "Initial MCNP6 release overview," *Nuclear Technology*, **180**, *3*, 298–315 (2012).

[11] T. T. Böhlen et al., "The FLUKA Code: Developments and Challenges for High Energy and Medical Applications," *Nuclear Data Sheets*, **120**, 211–214 (2014).

[12] A. Ferrari, P. R. Sala, A. Fasso, and J. Ranft, "FLUKA: a multi-particle transport code," CERN-2005-010, INFN/TC_05/11, SLAC-R-773 (2005).

[13] "Geant4 Physics Reference Manual, Version: Geant4 10.0," CERN (2013).

[14] J. Soto, "Statistical Testing of Random Number Generators," Proceedings of the 22nd National Information Systems Security Conference (1999).

[15] L. Devroye, *Non-uniform random variate generation*, Springer-Verlag (1986).

[16] A. J. Walker, "An Efficient Method for Generating Discrete Random Variables with General Distributions," *ACM Trans. Math. Softw.*, **3**, *3*, 253–256 (1977).

[17] E. Woodcock, "Techniques Used in the GEM Code for Monte Carlo Neutronics Calculations in Reactors and Other Systems of Complex Geometry," Proceedings of the Conference on the Applications of Computing Methods to Reactor Problems, ANL-7050, Argonne National Laboratory (1965).

[18] J. Leppänen, "Performance of Woodcock Delta-Tracking in Lattice Physics Applications Using the Serpent Monte Carlo Reactor Physics Burnup Calculation Code," *Annals of Nuclear Energy*, **37**, *5*, 715–722 (2010).

[19] N. Carron, *An Introduction to the Passage of Energetic Particles through Matter*, Taylor & Francis (2006).

[20] D. E. Cullen, J. H. Hubbell, and L. Kissel, "EPDL97: the Evaluated Photo Data Library '97 Version," UCRL–50400-Vol. 6-Rev. 5, Lawrence Livermore National Lab., CA (United States) (1997).

[21] M. Chadwick et al., "ENDF/B-VII.1 Nuclear Data for Science and Technology: Cross Sections, Covariances, Fission Product Yields and Decay Data," *Nuclear Data Sheets*, **112**, *12*, 2887–2996 (2011).

[22] E. Podgorsak, *Radiation Physics for Medical Physicists*, Biological and Medical Physics, Biomedical Engineering, Springer-Verlag Berlin Heidelberg (2010).

[23] T. Basaglia et al., "Physics methods for the simulation of photoionisation," *Proc. Nuclear Science Symposium and Medical Imaging Conference (NSS/MIC), 2013 IEEE*, p. 1–8, Oct, 2013.

[24] M. Pia et al., "Evaluation of Atomic Electron Binding Energies for Monte Carlo Particle Transport," *Nuclear Science, IEEE Transactions on Nuclear Science*, **58**, *6*, 3246–3268 (2011).

[25] D. R. Lide, *CRC Handbook of Chemistry and Physics, 73rd Edition*, Taylor & Francis (1992).

[26] G. Roach, J. Tickner, and Y. V. Haarlem, "Discrepancies in atomic shell and fluorescent X-ray energies in the Evaluated Photon Data Library EPDL97," *X-Ray Spectrometry*, **41**, *5*, 279–283 (2012).

[27] F. Sauter, "Über den atomaren Photoeffekt in der K-Schale nach der relativistischen Wellenmechanik Diracs," *Annalen der Physik*, **403**, *4*, 454–488 (1931).

[28] F. Salvat and J. M. Fernández-Varea, "Overview of physical interaction models for photon and electron transport used in Monte Carlo codes," *Metrologia*, **46**, *2*, S112–S138 (2009).

[29] M. Gavrila, "Relativistic L-Shell Photoeffect," *Phys. Rev.*, **124**, 1132–1141 (1961).

[30] R. H. Pratt, R. D. Levee, R. L. Pexton, and W. Aron, "K-Shell Photoelectric Cross Sections from 200 keV to 2 MeV," *Phys. Rev.*, **134**, A898–A915 (1964).

[31] H. K. Tseng, R. H. Pratt, S. Yu, and A. Ron, "Photoelectron angular distributions," *Phys. Rev. A*, **17**, 1061–1079 (1978).

[32] N. Nariyama, "Photon-produced electron fluence calculated with photoelectron angular distribution of Sauter expression," *Radiation Physics and Chemistry*, **75**, *11*, 1719–1722 (2006).

[33] J. Taylor, *Scattering Theory: The Quantum Theory of Nonrelativistic Collisions*, Dover Books on Engineering, Dover Publications (2012).

[34] J. H. Hubbell et al., "Atomic form factors, incoherent scattering functions, and photon scattering cross sections," *Journal of Physical and Chemical Reference Data*, **4**, *3*, 471–538 (1975).

[35] L. Kissel, B. Zhou, S. C. Roy, S. K. Sen Gupta, and R. H. Pratt, "The validity of form-factor, modified-form-factor and anomalous-scattering-factor approximations in elastic scattering calculations," *Acta Crystallographica Section A*, **51**, *3*, 271–288 (1995).

[36] W. Franz, "Rayleighsche Streuung harter Strahlung an schweren Atomen," *Zeitschrift für Physik*, **98**, *5-6*, 314-320 (1935).

[37] S. C. Roy, L. Kissel, and R. H. Pratt, "Elastic scattering of photons," *Radiation Physics and Chemistry*, **56**, *1–2*, 3–26 (1999).

[38] B. K. Chatterjee and S. C. Roy, "Tables of Elastic Scattering Cross Sections of Photons in the Energy Range 50–1500 keV for All Elements in the Range $13 \leq Z \leq 104$," *Journal of Physical and Chemical Reference Data*, **27**, *6*, 1011–1215 (1998).

[39] M. Batic, G. Hoff, M. G. Pia, and P. Saracco, "Photon Elastic Scattering Simulation: Validation and Improvements to Geant4," *Nuclear Science, IEEE Transactions on*, **59**, *4*, 1636–1664 (2012).

[40] L. Kissel, "RTAB: the Rayleigh scattering database," *Radiation Physics and Chemistry*, **59**, *2*, 185–200 (2000).

[41] W. Muhammad and S. H. Lee, "Impact of anomalous effects on the angular distribution of coherently scattered photons using Monte Carlo simulation," *Acta Crystallographica Section A*, **69**, *3*, 297–308 (2013).

[42] E. Cashwell et al., "Monte Carlo photon codes: MCG and MCP," Los Alamos National Laboratory Report, LA–5157–MS (1973).

[43] O. Klein and Y. Nishina, "Über die Streuung von Strahlung durch freie Elektronen nach der neuen relativistischen Quantendynamik von Dirac," *Zeitschrift für Physik*, **52**, *11–12*, 853–868 (1929).

[44] P. M. Bergstrom Jr. and R. H. Pratt, "An overview of the theories used in Compton scattering calculations," *Radiation Physics and Chemistry*, **50**, *1*, 3 – 29 (1997).

[45] P. M. Bergstrom, T. Surić, K. Pisk, and R. H. Pratt, "Compton scattering of photons from bound electrons: Full relativistic independent-particle-approximation calculations," *Phys. Rev. A*, **48**, 1134–1162 (1993).

[46] Z. Kaliman, T. Surić, K. Pisk, and R. H. Pratt, "Triply differential cross section for Compton scattering," *Phys. Rev. A*, **57**, 2683–2691 (1998).

[47] R. H. Pratt et al., "Compton scattering revisited," *Radiation Physics and Chemistry*, **79**, *2*, 124–131 (2010).

[48] J. H. Hubbell, "Summary of existing information on the incoherent scattering of photons, particularly on the validity of the use of the incoherent scattering function," *Radiation Physics and Chemistry*, **50**, *1*, 113–124 (1997).

[49] I. Waller and D. R. Hartree, "On the Intensity of Total Scattering of X-Rays," *Proceedings of the Royal Society of London A: Mathematical, Physical and Engineering Sciences*, **124**, *793*, 119–142 (1929).

[50] A. J. Freeman, "A study of the Compton scattering of X-rays, Ne, Cu$^+$, Cu and Zn," *Acta Crystallographica*, **12**, *4*, 274–279 (1959).

[51] M. J. Cooper, "Compton scattering and electron momentum determination," *Reports on Progress in Physics*, **48**, *4*, 415 (1985).

[52] R. Ribberfors, "Relationship of the relativistic Compton cross section to the momentum distribution of bound electron states," *Phys. Rev. B*, **12**, 2067–2074 (1975).

[53] R. Ribberfors and K. F. Berggren, "Incoherent-x-ray-scattering functions and cross sections $(d\sigma/d\Omega')_{\text{incoh}}$ by means of a pocket calculator," *Phys. Rev. A*, **26**, 3325–3333 (1982).

[54] F. Biggs, L. B. Mendelsohn, and J. B. Mann, "Hartree–Fock Compton profiles for the elements," *Atomic Data and Nuclear Data Tables*, **16**, *3*, 201–309 (1975).

[55] Y. Namito, S. Ban, and H. Hirayama, "Implementation of the Doppler broadening of a Compton-scattered photon into the EGS4 code," *Nuclear Instruments and Methods in Physics Research Section A: Accelerators, Spectrometers, Detectors and Associated Equipment*, **349**, *2–3*, 489–494 (1994).

[56] D. Brusa, G. Stutz, J. Riveros, J. Fernández-Varea, and F. Salvat, "Fast sampling algorithm for the simulation of photon Compton scattering," *Nuclear Instruments and Methods in Physics Research Section A: Accelerators, Spectrometers, Detectors and Associated Equipment*, **379**, *1*, 167–175 (1996).

[57] R. Ribberfors, "X-ray incoherent scattering total cross sections and energy-absorption cross sections by means of simple calculation routines," *Phys. Rev. A*, **27**, 3061–3070 (1983).

[58] J. Brown, M. Dimmock, J. Gillam, and D. Paganin, "A low energy bound atomic electron Compton scattering model for Geant4," *Nuclear Instruments and Methods in Physics Research Section B: Beam Interactions with Materials and Atoms*, **338**, *0*, 77–88 (2014).

[59] R. Pratt, L. LaJohn, T. Suric, B. Chatterjee, and S. Roy, "Limitations on the validity of impulse approximation in Compton scattering," *Nuclear Instruments and Methods in Physics Research Section B: Beam Interactions with Materials and Atoms*, **261**, *1–2*, 175 - 179 (2007).

[60] B. Chatterjee, S. Roy, T. Suric, L. LaJohn, and R. Pratt, "Asymmetry and the shift of the Compton profile," *Nuclear Instruments and Methods in Physics Research Section A: Accelerators, Spectrometers, Detectors and Associated Equipment*, **580**, *1*, 22–24 (2007).

[61] P. Kane, "Experimental studies of inelastic X-ray and $\gamma$-ray scattering," *Radiation Physics and Chemistry*, **50**, *1*, 31 - 62 (1997).

[62] R. Blomquist and E. Gelbard, "An Assessment of Existing Klein–Nishina Monte Carlo Sampling Methods," *Nuclear Science and Engineering*, **83**, *3*, 380–384 (1983).

[63] K. Mathews, "Random sampling from the Klein–Nishina distribution: Efficiency, Parsimony, and Speed," *Nuclear Science and Engineering*, **173**, *3*, 207–221 (2013).

[64] L. Koblinger, "Direct sampling from the Klein–Nishina distribution for photon energies above 1.4 MeV," *Nucl. Sci. Eng.*, **56**, *2*, 218–219 (1975).

[65] H. Kahn, "Applications of Monte Carlo," RM-1237-AEC, The Rand Corporation (1956).

[66] I. Lux and L. Koblinger, *Monte Carlo Particle Transport Methods: Neutron and Photon Calculations*, CRC Press (1991).

[67] G. Stutz, "Compton scattering cross section for inner-shell electrons in the relativistic impulse approximation," *Nuclear Instruments and Methods in Physics Research Section B: Beam Interactions with Materials and Atoms*, **319**, 8–16 (2014).

[68] J. H. Hubbell, H. a. Gimm, and I. Øverbø, "Pair, Triplet, and Total Atomic Cross Sections (and Mass Attenuation Coefficients) for 1 MeV-100 GeV Photons in Elements Z=1 to 100," *Journal of Physical and Chemical Reference Data*, **9**, *4*, 1023–147 (1980).

[69] D. C. Gates, R. W. Kenney, and W. P. Swanson, "Electron Triplet Production by High-Energy Photons in Hydrogen," *Phys. Rev.*, **125**, 1310–1318 (1962).

[70] S. Jarp and K. J. Mork, "Differential Cross Sections for Pair Production by Photons on Electrons," *Phys. Rev. D*, **8**, 159–168 (1973).

[71] J. H. Hubbell, "Electron–positron pair production by photons: A historical overview," *Radiation Physics and Chemistry*, **75**, *6*, 614–623 (2006).

[72] H. Davies, H. A. Bethe, and L. C. Maximon, "Theory of Bremsstrahlung and Pair Production. II. Integral Cross Section for Pair Production," *Phys. Rev.*, **93**, 788–795 (1954).

[73] J. C. Butcher and H. Messel, "Electron number distribution in electron-photon showers in air and aluminium absorbers," *Nuclear Physics*, **20**, *0*, 15–128 (1960).

[74] Y.-S. Tsai, "Pair production and bremsstrahlung of charged leptons," *Rev. Mod. Phys.*, **46**, 815–851 (1974).

[75] H. Bethe and W. Heitler, "On the Stopping of Fast Particles and on the Creation of Positive Electrons," *Proceedings of the Royal Society of London. Series A*, **146**, *856*, 83–112 (1934).

[76] I. Øverbø, K. J. Mork, and H. A. Olsen, "Pair Production by Photons: Exact Calculation for Unscreened Atomic Field," *Phys. Rev. A*, **8**, 668–685 (1973).

[77] K. K. Sud and D. K. Sharma, "Distorted wave Born approximation calculation of pair production cross section for 12.5 MeV photon," *Radiation Physics and Chemistry*, **75**, *6*, 631–643 (2006).

[78] J. W. Motz, H. A. Olsen, and H. W. Koch, "Pair Production by Photons," *Rev. Mod. Phys.*, **41**, 581–639 (1969).

[79] C. Selvaraju, A. S. Bhullar, and K. K. Sud, "DWBA differential and total pair production cross sections for intermediate energy photons," *Radiation Physics and Chemistry*, **61**, *1*, 1–17 (2001).

[80] S. M. Seltzer, "An Overview of ETRAN Monte Carlo Methods," in *Monte Carlo Transport of Electrons and Photons*, edited by T. Jenkins, W. Nelson, and A. Rindi, volume 38 of *Ettore Majorana International Science Series*, p. 153–181, Springer US, 1988.

[81] "LAT-PB-00637 Validation of Physical Processes in the Geant4 Simulator for the Gamma-ray Satellite GLAST (GLASTGeant4)," Department of Physics, Hiroshima University (2002).

[82] G. O. Depaola, "Azimuthal distribution for pair production by high-energy $\gamma$-rays," *Nuclear Instruments and Methods in Physics Research Section A: Accelerators, Spectrometers, Detectors and Associated Equipment*, **452**, *1–2*, 298–305 (2000).

[83] W. Heitler, *The Quantum Theory of Radiation*, Dover Publications (1984).

[84] B. McParland, *Nuclear Medicine Radiation Dosimetry: Advanced Theoretical Principles*, Springer (2010).

[85] K. Iwata, R. G. Greaves, and C. M. Surko, "$\gamma$-ray spectra from positron annihilation on atoms and molecules," *Phys. Rev. A*, **55**, 3586–3604 (1997).

[86] T. T. Böhlen, A. Ferrari, V. Patera, and P. R. Sala, "Describing Compton scattering and two-quanta positron annihilation based on Compton profiles: two models suited for the Monte Carlo method," *Journal of Instrumentation*, **7**, *07*, P07018 (2012).

[87] I. Buvat and D. Lazaro, "Monte Carlo simulations in emission tomography and GATE: An overview," *Nuclear Instruments and Methods in Physics Research Section A: Accelerators, Spectrometers, Detectors and Associated Equipment*, **569**, *2*, 323 - 329 (2006).

[88] S. T. Perkins, M. H. Chen, D. E. Cullen, and J. H. Hubbell, "Tables and graphs of atomic subshell and relaxation data derived from the LLNL Evaluated Atomic Data Library (EADL), Z=1-100," Lawrence Livermore National Laboratory, UCRL-50400, Vol. 30 (1991).

[89] J. H. Hubbell et al., "A Review, Bibliography, and Tabulation of K, L, and Higher Atomic Shell X-Ray Fluorescence Yields," *Journal of Physical and Chemical Reference Data*, **23**, *2*, 339–364 (1994).

[90] M. Augelli et al., "New physics data libraries for Monte Carlo transport," *Proc. Nuclear Science Symposium Conference Record (NSS/MIC), 2010 IEEE*, p. 307–310, Oct, 2010.

[91] S. M. Seltzer and M. J. Berger, "Bremsstrahlung spectra from electron interactions with screened atomic nuclei and orbital electrons," *Nuclear Instruments and Methods in Physics Research Section B: Beam Interactions with Materials and Atoms*, **12**, *1*, 95–134 (1985).

[92] S. M. Seltzer and M. J. Berger, "Bremsstrahlung energy spectra from electrons with kinetic energy 1 keV–10 GeV incident on screened nuclei and orbital electrons of neutral atoms with Z = 1–100," *Atomic Data and Nuclear Data Tables*, **35**, *3*, 345–418 (1986).

[93] S. M. Seltzer, "Cross Sections for Bremsstrahlung Production and Electron-Impact Ionization," in *Monte Carlo Transport of Electrons and Photons*, edited by T. M. Jenkins, W. R. Nelson, and A. Rindi, volume 38 of *Ettore Majorana International Science Series*, p. 81–114, Springer US, 1988.

[94] *Stopping Powers for Electrons and Positrons*, ICRU report 37, International Commission on Radiation Units and Measurements, Bethesda, MD (1984).

[95] L. Kim, R. H. Pratt, S. M. Seltzer, and M. J. Berger, "Ratio of positron to electron bremsstrahlung energy loss: An approximate scaling law," *Phys. Rev. A*, **33**, 3002–3009 (1986).

[96] H. Bethe, "Zur Theorie des Durchgangs schneller Korpuskularstrahlen durch Materie," *Annalen der Physik*, **397**, 325-400 (1930).

[97] H. Bethe, "Bremsformel für Elektronen relativistischer Geschwindigkeit," *Zeitschrift für Physik*, **76**, *5*, 293–299 (1932).

[98] M. J. Berger, "Electron Stopping Powers for Transport Calculations," in *Monte Carlo Transport of Electrons and Photons*, edited by T. M. Jenkins, W. R. Nelson, and A. Rindi, volume 38 of *Ettore Majorana International Science Series*, p. 57–80, Springer US, 1988.

[99] R. M. Sternheimer, "The Density Effect for the Ionization Loss in Various Materials," *Phys. Rev.*, **88**, 851–859 (1952).

[100] R. M. Sternheimer, S. M. Seltzer, and M. J. Berger, "Density effect for the ionization loss of charged particles in various substances," *Phys. Rev. B*, **26**, 6067–6076 (1982).

[101] M. J. Berger, J. Coursey, M. Zucker, and J. Chang, "Stopping-power and range tables for electrons, protons, and helium ions," NIST Physical Measurement Laboratory, `http://www.nist.gov/pml/data/star/index.cfm`, [accessed: 11 August 2014].

[102] "DABAX, DAtaBAse for X-ray applications," `http://ftp.esrf.eu/pub/scisoft/xop2.3/DabaxFiles/ComptonProfiles.dat`, 2015, [accessed: 6 May 2015].

[103] H. G. Hughes, "Recent developments in low-energy electron/photon transport for MCNP6," *Progress in Nuclear Science and Technology*, **4**, 454–458 (2014).

[104] R. E. MacFarlane and A. C. Kahler, "Methods for Processing ENDF/B-VII with NJOY," *Nuclear Data Sheets*, **111**, *12*, 2739–2890 (2010).

[105] A. Sood, "Doppler Energy Broadening for Incoherent Scattering in MCNP5, Part I," Los Alamos National Laboratory Report LA-UR-04-0487 (2004).

[106] A. Sood and M. C. White, "Doppler Energy Broadening for Incoherent Scattering in MCNP5, Part II," Los Alamos National Laboratory Report LA-UR-04-0488 (2004).

[107] B. C. Kiedrowski, F. B. Brown, M. C. White, and P. K. Donald, "Testing for the photon doppler broadening data sampling bug in MCNP5/X," Los Alamos National Laboratory Report LA-UR-12-00121 (2012).

[108] K. J. Adams, "Electron Upgrade for MCNP4B," Los Alamos National Laboratory Report LA-UR-00-3581 (2000).

[109] M. C. White, "Photoatomic Data Library MCPLIB03: An Update to MCPLIB02 Containing Compton Profiles for Doppler Broadening of Incoherent Scattering," Los Alamos National Laboratory Report LA-UR-03-0787 (2002).

[110] J. Leppänen, "Two practical methods for unionized energy grid construction in continuous-energy Monte Carlo neutron transport calculation," *Annals of Nuclear Energy*, **36**, 7, 878–885 (2009).

# A Pair production sampling coefficients

Table A.1: Coefficients for Eq. (3.140) for $Z = 1$–$50$.

| Atomic number $Z$ | $p_1$ | $p_2$ | $p_3$ | $q_1$ | $q_2$ |
|---|---|---|---|---|---|
| 1 | 15.712 | 525.50 | -392.40 | 83.770 | 339.67 |
| 2 | 15.372 | 501.88 | -366.79 | 80.706 | 320.35 |
| 3 | 15.147 | 485.79 | -351.56 | 78.700 | 306.82 |
| 4 | 14.977 | 474.16 | -340.29 | 77.270 | 297.03 |
| 5 | 14.838 | 464.39 | -331.35 | 76.099 | 288.68 |
| 6 | 14.715 | 454.58 | -324.12 | 74.962 | 280.01 |
| 7 | 14.615 | 448.81 | -317.38 | 74.277 | 275.19 |
| 8 | 14.521 | 442.35 | -311.61 | 73.540 | 269.56 |
| 9 | 14.436 | 436.42 | -306.43 | 72.875 | 264.34 |
| 10 | 14.358 | 430.99 | -301.69 | 72.274 | 259.54 |
| 11 | 14.285 | 425.93 | -297.30 | 71.723 | 255.06 |
| 12 | 14.216 | 421.15 | -293.20 | 71.210 | 250.82 |
| 13 | 14.152 | 416.70 | -289.35 | 70.740 | 246.87 |
| 14 | 14.090 | 412.49 | -285.72 | 70.302 | 243.12 |
| 15 | 14.031 | 408.17 | -282.38 | 69.856 | 239.22 |
| 16 | 13.975 | 404.43 | -279.06 | 69.478 | 235.91 |
| 17 | 13.920 | 400.69 | -275.94 | 69.103 | 232.56 |
| 18 | 13.868 | 397.16 | -272.92 | 68.755 | 229.41 |
| 19 | 13.818 | 393.97 | -269.99 | 68.450 | 226.59 |
| 20 | 13.768 | 390.54 | -267.29 | 68.120 | 223.50 |
| 21 | 13.717 | 386.19 | -264.76 | 67.689 | 219.55 |
| 22 | 13.673 | 384.00 | -262.16 | 67.503 | 217.61 |
| 23 | 13.627 | 380.85 | -259.69 | 67.212 | 214.79 |
| 24 | 13.582 | 377.80 | -257.28 | 66.933 | 212.06 |
| 25 | 13.537 | 374.80 | -254.91 | 66.663 | 209.38 |
| 26 | 13.493 | 371.74 | -252.53 | 66.386 | 206.68 |
| 27 | 13.450 | 368.88 | -250.25 | 66.133 | 204.14 |
| 28 | 13.408 | 366.20 | -248.05 | 65.904 | 201.76 |
| 29 | 13.366 | 363.32 | -245.78 | 65.652 | 199.25 |
| 30 | 13.323 | 360.12 | -243.39 | 65.361 | 196.50 |
| 31 | 13.273 | 354.59 | -240.87 | 64.791 | 191.76 |
| 32 | 13.243 | 355.34 | -239.25 | 64.979 | 192.28 |
| 33 | 13.203 | 352.88 | -237.15 | 64.780 | 190.13 |
| 34 | 13.163 | 350.21 | -234.96 | 64.556 | 187.84 |
| 35 | 13.122 | 347.29 | -232.66 | 64.302 | 185.39 |
| 36 | 13.083 | 344.83 | -230.54 | 64.106 | 183.28 |
| 37 | 13.036 | 340.22 | -227.68 | 63.637 | 179.57 |
| 38 | 13.006 | 340.46 | -226.50 | 63.780 | 179.51 |
| 39 | 12.968 | 338.09 | -224.38 | 63.595 | 177.50 |
| 40 | 12.929 | 335.75 | -222.26 | 63.414 | 175.53 |
| 41 | 12.891 | 333.51 | -220.16 | 63.246 | 173.65 |
| 42 | 12.853 | 331.15 | -218.00 | 63.063 | 171.68 |
| 43 | 12.816 | 328.97 | -215.89 | 62.903 | 169.86 |
| 44 | 12.776 | 326.23 | -213.54 | 62.672 | 167.65 |
| 45 | 12.740 | 324.51 | -211.58 | 62.571 | 166.17 |
| 46 | 12.703 | 322.21 | -209.37 | 62.394 | 164.28 |
| 47 | 12.666 | 320.11 | -207.22 | 62.245 | 162.56 |
| 48 | 12.629 | 317.93 | -205.02 | 62.085 | 160.77 |
| 49 | 12.591 | 315.76 | -202.80 | 61.925 | 159.00 |
| 50 | 12.554 | 313.64 | -200.58 | 61.773 | 157.28 |

Table A.2: Coefficients for Eq. (3.140) for $Z = 51$–$100$.

| Atomic number $Z$ | $p_1$ | $p_2$ | $p_3$ | $q_1$ | $q_2$ |
|---|---|---|---|---|---|
| 51 | 12.518 | 311.49 | -198.32 | 61.616 | 155.54 |
| 52 | 12.480 | 309.31 | -196.04 | 61.454 | 153.78 |
| 53 | 12.444 | 307.30 | -193.79 | 61.314 | 152.14 |
| 54 | 12.407 | 305.20 | -191.50 | 61.163 | 150.45 |
| 55 | 12.363 | 301.01 | -188.41 | 60.728 | 147.30 |
| 56 | 12.334 | 300.97 | -186.83 | 60.854 | 147.05 |
| 57 | 12.296 | 298.55 | -184.37 | 60.659 | 145.14 |
| 58 | 12.262 | 296.94 | -182.16 | 60.571 | 143.81 |
| 59 | 12.225 | 294.79 | -179.75 | 60.409 | 142.08 |
| 60 | 12.189 | 292.85 | -177.39 | 60.276 | 140.52 |
| 61 | 12.151 | 290.39 | -174.84 | 60.071 | 138.59 |
| 62 | 12.116 | 288.70 | -172.53 | 59.971 | 137.19 |
| 63 | 12.081 | 286.76 | -170.12 | 59.835 | 135.62 |
| 64 | 12.043 | 284.33 | -167.53 | 59.631 | 133.71 |
| 65 | 12.009 | 282.73 | -165.19 | 59.541 | 132.37 |
| 66 | 11.971 | 280.31 | -162.59 | 59.336 | 130.46 |
| 67 | 11.936 | 278.25 | -160.09 | 59.182 | 128.81 |
| 68 | 11.901 | 276.70 | -157.72 | 59.096 | 127.49 |
| 69 | 11.864 | 274.30 | -155.09 | 58.891 | 125.59 |
| 70 | 11.830 | 272.59 | -152.65 | 58.781 | 124.15 |
| 71 | 11.794 | 270.56 | -150.12 | 58.625 | 122.49 |
| 72 | 11.759 | 268.68 | -147.61 | 58.490 | 120.93 |
| 73 | 11.723 | 266.70 | -145.08 | 58.339 | 119.29 |
| 74 | 11.688 | 264.69 | -142.53 | 58.183 | 117.63 |
| 75 | 11.651 | 262.35 | -139.91 | 57.978 | 115.73 |
| 76 | 11.617 | 260.72 | -137.45 | 57.874 | 114.31 |
| 77 | 11.582 | 258.72 | -134.90 | 57.715 | 112.63 |
| 78 | 11.546 | 256.38 | -132.30 | 57.507 | 110.71 |
| 79 | 11.512 | 254.75 | -129.84 | 57.398 | 109.26 |
| 80 | 11.477 | 252.75 | -127.32 | 57.236 | 107.55 |
| 81 | 11.442 | 250.77 | -124.81 | 57.074 | 105.84 |
| 82 | 11.407 | 248.74 | -122.30 | 56.903 | 104.08 |
| 83 | 11.373 | 246.73 | -119.81 | 56.735 | 102.33 |
| 84 | 11.338 | 244.75 | -117.35 | 56.569 | 100.59 |
| 85 | 11.304 | 242.85 | -114.92 | 56.412 | 98.882 |
| 86 | 11.269 | 240.87 | -112.50 | 56.244 | 97.116 |
| 87 | 11.235 | 238.91 | -110.10 | 56.075 | 95.341 |
| 88 | 11.201 | 236.92 | -107.74 | 55.901 | 93.533 |
| 89 | 11.166 | 234.94 | -105.40 | 55.727 | 91.722 |
| 90 | 11.131 | 232.68 | -103.08 | 55.508 | 89.698 |
| 91 | 11.093 | 229.55 | -100.74 | 55.150 | 87.096 |
| 92 | 11.065 | 229.07 | -98.619 | 55.203 | 86.223 |
| 93 | 11.031 | 227.04 | -96.442 | 55.014 | 84.310 |
| 94 | 10.997 | 225.15 | -94.314 | 54.844 | 82.469 |
| 95 | 10.963 | 222.92 | -92.240 | 54.620 | 80.383 |
| 96 | 10.930 | 221.20 | -90.217 | 54.473 | 78.619 |
| 97 | 10.897 | 219.34 | -88.251 | 54.301 | 76.738 |
| 98 | 10.864 | 217.41 | -86.350 | 54.118 | 74.796 |
| 99 | 10.831 | 215.49 | -84.516 | 53.933 | 72.832 |
| 100 | 10.797 | 213.29 | -82.778 | 53.703 | 70.662 |